VILNIUS
TECH
Vilniaus Gedimino
technikos universitetas

Mahmoud Samy Mahmoud Mohammed FARH

ANALYSIS AND MODELING OF DEFORMATIONS INDUCED BY THE EXTRUSION OF FIBER-REINFORCED POLYMERS

DOCTORAL DISSERTATION

TECHNOLOGICAL SCIENCES,
MATERIALS ENGINEERING (T 008)

Vilnius, 2026

2026-023-M

VILNIUS GEDIMINAS TECHNICAL UNIVERSITY

Mahmoud Samy Mahmoud Mohammed FARH

ANALYSIS AND MODELING OF DEFORMATIONS INDUCED BY THE EXTRUSION OF FIBER-REINFORCED POLYMERS

DOCTORAL DISSERTATION

TECHNOLOGICAL SCIENCES,
MATERIALS ENGINEERING (T 008)

Vilnius, 2026

The doctoral dissertation was prepared at Vilnius Gediminas Technical University in 2021–2026.

Supervisor

Prof. Dr Viktor GRIBNIAK (Vilnius Gediminas Technical University, Materials Engineering – T 008).

The Dissertation Defense Council of the Scientific Field of Materials Engineering of Vilnius Gediminas Technical University:

Chairman

Assoc. Prof. Dr Nikolaj VIŠNIAKOV (Vilnius Gediminas Technical University, Materials Engineering – T 008).

Members:

Prof. Dr Darius BAČINSKAS (Vilnius Gediminas Technical University, Civil Engineering – T 002),

Dr Genrik MORDAS (State Research Institute Center for Physical Sciences and Technology, Materials Engineering – T 008),

Prof. Dr Dimitrios PAVLOU (University of Stavanger, Norway, Mechanical Engineering – T 009),

Assoc. Prof. Dr Jelena ŠKAMAT (Vilnius Gediminas Technical University, Materials Engineering – T 008).

The dissertation will be defended at the public meeting of the Dissertation Defense Council of the Scientific Field of Materials Engineering in the *Aula Doctoralis* Meeting Hall of Vilnius Gediminas Technical University at **2 p.m. on 10 June 2026.**

Address: Saulėtekio al. 11, LT-10223 Vilnius, Lithuania.
Tel.: +370 5 274 4956; fax +370 5 270 0112; e-mail: doktor@vilniustech.lt

A notification on the intended defense of the dissertation was sent on 8 May 2026.
A copy of the doctoral dissertation is available for review at Vilnius Gediminas Technical University repository https://etalpykla.vilniustech.lt and the Library of Vilnius Gediminas Technical University (Saulėtekio al. 14, LT-10223 Vilnius, Lithuania).

Vilnius Gediminas Technical University book No. 2026-023-M

https://doi.org/10.20334/2026-023-M

Mahmoud-Mohammed.Farh@vilniustech.lt

VILNIAUS GEDIMINO TECHNIKOS UNIVERSITETAS

Mahmoud Samy Mahmoud Mohammed FARH

PLUOŠTAIS ARMUOTŲ POLIMERŲ EKSTRUZIJOS SUKELTŲ DEFORMACIJŲ ANALIZĖ IR MODELIAVIMAS

DAKTARO DISERTACIJA

TECHNOLOGIJOS MOKSLAI,
MEDŽIAGŲ INŽINERIJA (T 008)

Vilnius, 2026

Disertacija rengta 2021–2026 metais Vilniaus Gedimino technikos universitete.

Vadovas

prof. dr. Viktor GRIBNIAK (Vilniaus Gedimino technikos universitetas, Medžiagų inžinerija – T 008).

Vilniaus Gedimino technikos universiteto Medžiagų inžinerijos mokslo krypties disertacijos gynimo taryba:

Pirmininkas

doc. dr. Nikolaj VIŠNIAKOV (Vilniaus Gedimino technikos universitetas, Medžiagų inžinerija – T 008).

Nariai:

prof. dr. Darius BAČINSKAS (Vilniaus Gedimino technikos universitetas, Statybos inžinerija – T 002),

dr. Genrik MORDAS (Valstybinis mokslinių tyrimų institutas Fizinių ir technologijos mokslų centras, Medžiagų inžinerija – T 008),

prof. dr. Dimitrios PAVLOU (Stavangerio universitetas, Norvegija, Mechanikos inžinerija – T 009),

doc. dr. Jelena ŠKAMAT (Vilniaus Gedimino technikos universitetas, Medžiagų inžinerija – T 008).

Disertacija bus ginama viešame Medžiagų inžinerijos mokslo krypties disertacijos gynimo tarybos posėdyje **2026 m. birželio 10 d. 14 val.** Vilniaus Gedimino technikos universiteto *Aula Doctoralis* posėdžių salėje.

Adresas: Saulėtekio al. 11, LT-10223 Vilnius, Lietuva.
Tel.: (0 5) 274 4956; faksas (0 5) 270 0112; el. paštas doktor@vilniustech.lt

Pranešimai apie numatomą ginti disertaciją išsiųsti 2026 m. gegužės 8 d.
Disertaciją galima peržiūrėti Vilniaus Gedimino technikos universiteto talpykloje https://etalpykla.vilniustech.lt/ ir Vilniaus Gedimino technikos universiteto bibliotekoje (Saulėtekio al. 14, LT-10223 Vilnius, Lietuva).

Abstract

Additive manufacturing via fused filament fabrication (FFF) enables the creation of geometrically complex components. Yet, its use in structural and semi-structural applications remains limited by anisotropic mechanical response, defect sensitivity, and fabrication-induced residual stresses that cause warpage and geometric inaccuracy. This dissertation investigates polylactic acid (PLA)- based materials manufactured by FFF, including neat and partially recycled PLA, continuously reinforced PLA, and short-fiber-reinforced composites, to develop an integrated experimental-computational methodology for evaluating mechanical efficiency and predicting process-induced distortion. The research object comprises the mechanical, thermal, viscoelastic, microstructural, and thermo-mechanical characteristics of these materials. The dissertation develops a unified approach linking reinforcement strategy, material structure, thermal history, mechanical performance, and warpage behavior. The adopted methodology combines quasi-static tensile and flexural testing, thermomechanical characterization, scanning electron microscopy, and finite-element simulations.

Continuous aramid reinforcement developed in this study for FFF increases the load-bearing capacity of the tension specimens by 67%. Still, reinforcement efficiency was limited by toolpath continuity, interfacial defects, and the absence of in-process fiber tensioning. Short-fiber-reinforced composites exhibit distinct fiber-type-dependent behavior: carbon-filled PLA increases stiffness, while wood-filled PLA enhances crystallinity, stiffness retention near the glass-transition temperature, toughness, and dimensional fidelity. Wood-fiber reinforcement reduces edge warpage by 43% and carbon fiber by 14.3% under identical conditions. A staged thermo-mechanical simulation framework is developed to model printing, cooling, and detachment, transferring residual stress and distortion fields into subsequent mechanical simulations. The ABAQUS model for neat PLA predicts warpage with an average error of 8.2–10.6%, whereas a Digimat workflow captures the deformation in short-fiber-reinforced PLA with an error of 14.3–17.9%. The latter predictions were obtained for the first time.

The dissertation consists of an introduction, three main chapters, general conclusions, and references. The First Chapter provides a literature review of FFF of reinforced polymers, including material combination and modeling strategies. The Second Chapter specifies the chosen materials, test program, and thermo-mechanical modeling concept. The Third Chapter evaluates experimental and numerical results, integrating mechanical, thermal, microstructural, and simulation-based findings. The General Conclusions summarize the dissertation work, which is supported by four publications, including three articles in Web of Science-indexed journals with impact factors, and four conference presentations.

Reziumė

Polimerų 3D spausdinimas sudaro galimybę pritaikyti gamybą sudėtingos geometrijos objektams. Vis dėlto jų konstrukcinį pritaikymą riboja spausdintos medžiagos anizotropinės mechaninės savybės, gamybos metu susidarantys mikrostruktūros defektai ir liekamieji įtempiai, sukeliantys matmenų netikslumus bei formos iškraipymus. Šioje disertacijoje tiriamos 3D spausdintos polilaktido (PLA) medžiagos: grynasis ir dalinai perdirbtas PLA, ištisine aramido gija ir trumpais plaušais armuoti kompozitai. Tyrimo tikslas – sukurti kombinuotą eksperimentinę ir skaitmeninę metodiką, leidžiančią įvertinti armavimo efektyvumą ir numatyti gamybos metu atsirandančias liekamąsias deformacijas. Tyrimo objektas apima spausdintų PLA kompozitų termomechanines ir viskoelastines savybes bei terminio virsmo parametrai. Tyrimų metodika apima tempimo ir lenkimo bandymus, termomechaninių savybių tyrimus, skenuojančiąją elektroninę mikroskopiją ir baigtinių elementų modeliavimą.

Sukurta ištisine aramido armuoto polilaktido gija pritaikyta 3D spausdinimo technologijai padidino tempiamųjų bandinių laikomąją galią 67 %, tačiau armavimo efektyvumą ribojo gijos išdėstymo netiesiškumas, sukibimo defektai ir įtempimo trūkumas 3D spausdinimo metu. Trumpais plaušais armuoti polimero kompozitai pasižymėjo skirtingu plaušų poveikiu: anglies plaušai didino kompozito standumą, o medienos plaušai – kristalizavimo laipsnį, standumą ties stiklinimo temperatūra, tąsumą ir matmenų pastovumą. Lyginant su grynuoju PLA, medienos plaušai sumažino bandinio kraštų išlinkį 43 %, o anglies plaušai – 14 %. Sukurtas kombinuotas baigtinių elementų modelis, kuriame termomechaninio uždavinio sprendimas pažingsniui atkuria 3D spausdinimo, aušinimo ir pačio objekto atskyrimo nuo gamybos platformos etapus. Gauti liekamųjų įtempių ir deformacijų pasiskirstymo laukai eksportuojami į mechaninį modelį. ABAQUS modeliavimo aplinkoje grynojo PLA išlinkis apskaičiuotas su 8,2–10,6 % vidutine paklaida, o Digimat aplinkoje sudarytas modelis nustato trumpais plaušais armuotų kompozitų deformacijas su 14,3–17,9 % paklaida. Toks modeliavimas trumpais plaušais armuotiems kompozitams atliktas pirmą kartą.

Disertaciją sudaro įvadas, trys pagrindiniai skyriai, bendrosios išvados ir literatūros sąrašas. Pirmajame skyriuje pateikta 3D spausdinimo armuoto polimero kompozitų literatūros apžvalga, aptariant medžiagų sandarą, armavimo ir modeliavimo būdus. Antrajame skyriuje aprašytos pasirinktos medžiagos, bandymo programa ir skaitinio modeliavimo principai. Trečiajame skyriuje pateikti bandymų ir modeliavimo rezultatai. Bendrosiose išvadose pateikti svarbiausi darbo rezultatai. Disertacijos tyrimo pagrindu paskelbtos keturios mokslinės publikacijos, iš kurių trys straipsniai – *Web of Science* žurnaluose su citavimo rodikliais, ir keturi pranešimai pristatyti mokslinėse konferencijose.

Notations

Symbols

A – the cross-sectional area (liet. *skerspjūvio plotas*);
C_{ef} – the coefficient describes the fiber reinforcement efficiency (liet. *plaušų armavimo efektyvumo koeficientas*);
E – the modulus of elasticity (liet. *tampumo modulis*);
E_f – the flexural modulus of elasticity (liet. *lenkimo tampumo modulis*);
K_b – the Stefan-Boltzmann constant (liet. *Stefano ir Boltzmanno konstanta*);
L – the support span length (liet. *atstumas tarp atramų*);
N_f – the internal force acting on the fiber (liet. *pluoštą veikianti vidinė jėga*);
N_p – the internal force acting on the matrix (liet. *matricą veikianti vidinė jėga*);
Ñ – the divergence operator (liet. *divergencijos operatorius*);
P – the applied point load (liet. *taškinė apkrova*);
P_u – the ultimate load (liet. *ribinė apkrova*);
$S(T)$ – the temperature-dependent compliance (the inverse of the stiffness matrix) (liet. *nuo temperatūros priklausantis pasiduodamumas, arba atvirkštinė standumo matrica*);
$S(t)$ – the external surface of the body changing with time (liet. *išorinis kūno paviršius kintantis laike*);
T – the temperature (liet. *temperatūra*);
T_b – the print bed temperature (liet. *gamybos (spausdinimo) pagrindo temperatūra*);
T_{cc} – the cold crystallization temperature (liet. *šaltosios kristalizacijos temperatūra*);

T_f – the extrusion temperature (liet. *ekstruzijos temperatūra*);
T_g – the glass transition temperature (liet. *stiklėjimo temperatūra*);
T_m – the melting temperature (liet. *lydymosi temperatūra*);
T_s – the surrounding temperature (liet. *aplinkos temperatūra*);
V_f – the volumetric fiber fraction (liet. *plaušo tūrio dalis*);
$V_{f,ef}$ – the efficient reinforcement fraction (liet. *efektyvioji armavimo dalis*);
X_c – the degree of crystallinity (liet. *kristališkumo laipsnis*);
b – the specimen width (liet. *bandinio plotis*);
c – the specific heat capacity (liet. *specifinė šiluminė talpa*);
d – the specimen thickness (liet. *bandinio storis*);
e – the emissivity (liet. *spinduliavimo koeficientas*);
f_y – the yield strength (liet. *takumo stipris*);
h – the heat transfer coefficient (liet. *šilumos perdavimo koeficientas*);
k – the thermal conductivity (liet. *šiluminis laidumas*);
m – the slope of the load-deflection curve (liet. *apkrovos ir įlinkio diagramos posvyris*);
n – the vector normal to the surface (liet. *paviršiaus normalės vektorius*);
q – the heat source (liet. *šilumos šaltinis*);
q_c – the convective heat flux (liet. *šilumos srautas dėl konvekcijos*);
q_r – the radiative heat flux (liet. *šilumos srautas dėl spinduliavimo*);
w – the mass fraction (liet. *masės dalis*);
ΔH_{cc} – the cold crystallization enthalpy (liet. *šaltosios kristalizacijos entalpija*);
ΔH_m – the measured melting enthalpy (liet. *išmatuota lydymosi entalpija*);
Δt – the time step (liet. *laiko periodas*);
$\Delta \sigma$ – the change in stress (liet. *įtempių pokytis*);
$\Delta \varepsilon$ – the change in strain (liet. *deformacijų pokytis*);
Ω_b – the surface of the print bed (liet. *spausdinimo pagrindo paviršius*);
Ω_f – the surface of the extruded material (liet. *spausdintos medžiagos paviršius*);
α – the thermal expansion coefficient (liet. *šiluminio plėtimosi koeficientas*);
$\alpha(T)$ – the temperature-dependent second-order tensor of the thermal expansion coefficient (liet. *antrosios eilės šiluminio plėtimosi koeficiento tenzorius kintantis laike*);
ε – the strain (liet. *deformacija*);
ε_e – the elastic strain (liet. *tamprioji deformacija*);
ε_{pl} – the plastic strain (liet. *plastinė deformacija*);
ε_t – the thermal strain (liet. *deformacija nuo temperatūros*);
ε_y – the strain at the yield point (liet. *takumo ribos deformacija*);
λ – the plastic flow factor (liet. *plastinio tekėjimo koeficientas*);
ν – the Poisson’s ratio (liet. *Puasono koeficientas*);
ρ – the material density (liet. *medžiagos tankis*);
σ_{dev} – the deviatoric part of the stress tensor (liet. *įtempių tenzoriaus deviatorinė dalis*);
σ_f – the flexural stress (liet. *lenkimo įtempiai*);
σ_u – the ultimate strength (liet. *stiprumo riba*);
σ_y – the yield strength (liet. *takumo stipris*);
σ_{vm} – the effective Von Mises stress (liet. *efektyvūs Von Mizeso įtempiai*);

$\frac{\partial T}{\partial t}$ – the time rate of change of temperature (liet. *temperatūros kitimo sparta laiko atžvilgiu*);

^{T} – the transposition operator (liet. *transponavimo ženklas*).

Abbreviations

ABS – acrylonitrile butadiene styrene (liet. *akrilnitrilo butadieno stirenas*);

AF – aramid fiber (liet. *aramido plaušas*);

AM – additive manufacturing (liet. *adityvioji gamyba*);

AM-FRP – additive manufacturing of fiber-reinforced polymer (liet. *plaušų armuotų polimerų adityvioji gamyba*);

ASTM International – formerly the American Society for Testing and Materials (ASTM) (liet. *Amerikos medžiagų ir bandymų draugija*);

C3D20R – 20-node quadratic brick element (liet. *20 integravimo mazgų kubo formos baigtinis elementas*);

CAD – computer-aided design (liet. *kompiuterinis projektavimas*);

CF – carbon fiber (liet. *anglies plaušas*);

CNT – carbon nanotubes (liet. *anglies nanovamzdeliai*);

CoV – coefficient of variation (liet. *variacijos koeficientas*);

DfAM – design for additive manufacturing (liet. *projektavimas adityviai gamybai*);

DIC – digital image correlation (liet. *skaitmeninių vaizdų koreliacija*);

DMA – dynamic mechanical analysis (liet. *dinaminė mechaninė analizė*);

DSC – differential scanning calorimetry (liet. *diferencinė skenuojanti kalorimetrija*);

FDM – fused deposition modeling (liet. *lydymosi nusodinimo modeliavimas arba 3D spausdinimas*);

FE – finite element (liet. *baigtinis elementas*);

FFF – fused filament fabrication (liet. *lydyto siūlo gamyba arba 3D spausdinimas*);

FRP – fiber-reinforced polymer (liet. *pluoštų armuotas polimeras*);

GF – glass fiber (liet. *stiklo plaušas*);

HDT – heat deflection temperature (liet. *šiluminio įlinkio temperatūra*);

ISO – International Organization for Standardization (liet. *Tarptautinė standartizacijos organizacija*);

MCF – milled carbon fiber (liet. *maltas anglies plaušas*);

MEX – material extrusion (liet. *medžiagos ekstruzija*);

MWCNT – multi-walled carbon nanotubes (liet. *daugiasieniai anglies nanovamzdeliai*);

ONYX – Nylon 6 (Polyamide 6) (liet. *poliamidas 6*);

PA – polyamide (liet. *poliamidas*);

PBAT – polybutylene adipate-co-terephthalate (liet. *polibutileno adipato terephtalatas*);

PBS – polybutylene succinate (liet. *polibutileno sukcinatas*);

PC – polycarbonate (liet. *polikarbonatas*);

PCL – polycaprolactone (liet. *polikaprolaktonas*);

PEEK – polyether ether ketone (liet. *polietereterketonas*);

PEI – polyetherimide (liet. *polieterimidas*);

PEK – polyetherketone (liet. *polieterketonas*);
PETG – polyethylene terephthalate glycol (liet. *polietileno tereftalato glikolis*);
PGA – polyglycolic acid (liet. *poliglikolio rūgštis*);
PHA – polyhydroxyalkanoate (liet. *polihidroksialkanoatas*);
PLA – polylactic acid (liet. *polipieno rūgštis*);
PLA-CF – carbon fiber-reinforced PLA (liet. *anglies plaušų armuota polipieno rūgštis*);
PLA-WF – wood fiber-reinforced PLA (liet. *medžio plaušų armuota polipieno rūgštis*);
PLGA – poly (lactic-co-glycolic acid) (liet. *polilaktido glikolido rūgštis*);
PP – polypropylene (liet. *polipropilenas*);
RVE – representative volume element (liet. *reprezentatyvusis tūrinis elementas*);
SAC – Standardization Administration of China (liet. *Kinijos Liaudės Respublikos standartizacijos administracija*);
SEM – scanning electron microscope (liet. *skenuojantis elektroninis mikroskopas*);
SLA – stereolithography (liet. *stereolitografija*);
SLS – selective laser sintering (liet. *selektyvusis lazerinis sukepinimas*);
SWCNT – single-walled carbon nanotubes (liet. *vienasieniai anglies nanovamzdeliai*);
TO – topology optimization (liet. *topologijos optimizavimas*);
TPU – thermoplastic polyurethane (liet. *termoplastinis poliuretanas*);
UV – ultraviolet (liet. *ultravioletinė spinduliuotė*).

Table of Contents

Introduction

Problem formulation

The rapid growth of fused filament fabrication (FFF) has increased interest in its use for functional components. However, its broader adoption is limited by insufficient, anisotropic mechanical performance and an incomplete understanding of how thermal histories generate residual stresses, warpage, and related mechanical degradation. These challenges intensify when recycled feedstock is introduced to meet sustainability goals. Although reinforcement strategies, short-fiber filaments, and continuous-fiber routes can improve performance, they also increase the complexity in fiber–matrix interaction, interlayer integrity, and defect sensitivity. A unified framework is therefore needed to link material selection (including recycled plastics), reinforcement architecture, microstructure, thermo-physical behavior, mechanical response, and process-induced distortions to improve the structural performance and geometric fidelity of FFF components.

Relevance of the dissertation

The dissertation is relevant to scientific and industrial communities because it addresses three converging developments: advances in FFF-based fiber-reinforced polymers, the growing need for sustainable polymer-processing routes, and the shift toward process-aware analysis that reduces trial-and-error experimentation. The increasing availability of short-fiber filaments and progress in continuous-fiber integration create opportunities for mechanically efficient components, while intensifying the importance of fiber-matrix interaction, interlayer integrity, and defect sensitivity. Evaluating unreinforced recycled polylactic acid (PLA) supports sustainability-oriented adoption where mechanical verification is required, and continuous-fiber reinforcement further enhances PLA's mechanical performance. Thermo-mechanical process analysis strengthens this direction by clarifying how residual stresses and warpage influence dimensional fidelity and structural reliability in FFF components.

Research object

The research focuses on the mechanical, thermal, viscoelastic, and microstructural properties of FFF-manufactured PLA-based short- and continuous-fiber-reinforced composites, as well as fabrication-induced residual stresses and warpage.

Aim of the dissertation

The dissertation aims to develop an experimental-computational methodology to assess the mechanical efficiency of reinforced PLA composites and predict FFF-induced geometric distortion and residual-stress evolution.

Tasks of the dissertation

To achieve the research aim, the dissertation integrates literature analysis, physical experiments, material characterization, and finite-element simulations. Based on these methodological components, the following tasks are formulated:

1. To evaluate the mechanical performance of PLA-based FFF components by determining how reinforcement strategy (continuous and short fibers) and material composition (including recycled PLA) affect load-bearing capacity, stiffness, and failure behavior.
2. To establish the relationships among fabrication process, microstructure, and thermo-physical response by analyzing crystallinity, viscoelastic behavior, thermal transitions, and microstructural features of neat and fiber-reinforced PLA, and by identifying the dominant failure mechanisms governing composite performance.

3. To develop and validate a coupled thermo-mechanical modeling framework capable of predicting residual stresses, geometric distortions, and warpage mitigation by integrating temperature-dependent material behavior and mean-field homogenization for short-fiber composites across the printing, cooling, and detachment stages.

Research methodology

Theoretical analysis established the research context and supported the development of a unified framework linking reinforcement strategy, microstructure, thermal behavior, mechanical performance, dimensional stability, and process-aware simulation in FFF. Experimental design and manufacturing parameters followed established laboratory practice for FFF specimens and validated their mechanical response. Mechanical characterization included quasi-static tensile tests, supplemented by digital image correlation (DIC) for continuously reinforced samples, and quasi-static tensile and three-point bending tests for short-fiber composites. Thermal transitions and temperature-dependent stiffness were quantified using differential scanning calorimetry (DSC) and dynamic mechanical analysis (DMA). Scanning electron microscopy (SEM) was used to evaluate the microstructural characteristics, reinforcement dispersion, interface quality, and defects. A coupled thermo-mechanical finite-element workflow in ABAQUS was developed for neat PLA to simulate printing, cooling, and detachment and to predict residual stresses and warpage. A Digimat-based workflow using RVE-based homogenization and Digimat-AM process simulation was used for short-fiber-reinforced composites to analyze warpage.

Scientific novelty of the dissertation

The aspects of scientific novelty in the experimental and numerical investigation of PLA-based materials manufactured by FFF are as follows:

1. The SEM, DSC, and DMA techniques jointly clarify the key interaction mechanisms in short-fiber-reinforced PLA composites, linking fiber type, crystallinity, viscoelastic behavior, and microstructural integrity to the resulting material performance. This multifunctional analysis demonstrates that wood fibers at 30 wt% enhance crystallinity, toughness, and dimensional fidelity without compromising overall performance. In contrast, carbon fibers at 10 wt% affect stiffness and failure mechanisms through interface-controlled microstructural defects.

2. The developed thermo-mechanical simulation framework transfers the FFF-induced residual stress and geometric distortion fields from the filament depositing and cooling stages into the subsequent mechanical simulation. The DSC- and DMA-based characterization of thermal transitions and stiffness changes in the PLA-based composites provides the temperature-dependent input of the model, governing residual-stress accumulation and detachment-induced deformation.
3. A Digimat-based workflow is implemented for short-fiber-reinforced PLA composites. An RVE-based material model for the PLA composites was developed based on the microstructure investigation for the first time to predict warpage during FFF-induced detachment.

Practical value of the research findings

The practical value of the research findings is as follows:

1. The demonstrated continuous aramid reinforcement route provides a practical reference for extending PLA-based printing toward higher load-carrying concepts on conventional FFF platforms, while highlighting implementation constraints that must be addressed to improve reinforcement efficiency and reproducibility.
2. Experimental data are obtained for the tensile behavior of PLA specimens under controlled FFF conditions, including a sustainability-oriented comparison between virgin PLA and recycled-content PLA to establish a verified baseline mechanical response for printed feedstocks.
3. The combined mechanical results and fracture-level SEM observations for PLA, carbon fiber-reinforced PLA, and wood fiber-reinforced PLA support material selection under application constraints by clarifying how short-fiber addition changes the balance between stiffness, ultimate capacity, and damage tolerance, and by indicating the role of interface- and defect-controlled failure in limiting load transfer efficiency.
4. The DSC and DMA characterization provides temperature-dependent modeling guidance for FFF parts by identifying transition behavior and stiffness-retention trends relevant to components exposed to elevated temperatures near the glass-transition region. The temperature-dependent material properties obtained from DSC and DMA testing must be used to calibrate thermo-mechanical simulation models to ensure reliable predictions of residual stresses and warpage in FFF components.
5. The coupled thermo-mechanical FFF-simulation framework developed in ABAQUS provides a process-aware tool for anticipating distortion and deformation driven by residual stress. The FFF-induced detachment stage

governs the release of accumulated residual stresses and may lead to failure of the fabrication process; the proposed modeling framework identifies cases in which detachment-induced warpage is likely to occur, thereby enabling the identification of warpage-prone geometries and parameter sensitivities, reducing the number of experimental iterations required to achieve acceptable dimensional accuracy, and allowing designers to assess distortion risk before printing.

6. An automated Python-based subroutine was created to convert slicer-generated G-code into a time-resolved event series for finite-element activation, accelerating model preparation and reducing implementation errors in process-aware simulations.
7. The Digimat-based thermo-mechanical workflow extends process-level warpage prediction to short-fiber PLA composites by combining homogenized-material modeling with FFF process simulation, enabling comparative assessment of material-dependent distortion trends. Among the investigated materials, the PLA composite containing wood fibers exhibited the greatest reduction in FFF-induced warpage, indicating that this reinforcement type can be selected when improved dimensional accuracy is required. In addition, the combination of PLA with wood fibers offers a potentially biodegradable and sustainable alternative for applications where environmental impact is a design consideration.

Defended statements

The following statements, based on the results of the dissertation, serve as the official hypothesis to be defended:

1. The developed continuous aramid-reinforced PLA filament is compatible with conventional single-extruder FFF printers. Yet, the reinforcement cannot achieve its theoretical efficiency under these conditions because the process neither tensions the fiber nor ensures geometric accuracy.
2. Short-fiber reinforcement reduces warpage and improves geometric fidelity in FFF-printed PLA composites. Wood fibers further modify polymer crystallinity and enhance toughness, enabling the development of dimensionally precise and sustainable PLA-based composite materials.
3. The developed coupled thermo-mechanical modeling workflow predicts FFF-induced geometric distortion in neat and short-fiber-reinforced PLA composites. The automated transformation of the fabrication model into a software-ready finite-element mesh enables process-aware structural simulation of printed components.

Approval of the research findings

Four publications were produced on the research topic, including three articles in Web of Science-indexed journals with impact factors. The author has made four presentations at scientific conferences:

- Presentation “Numerical Simulation of Polymer Extrusion-Based Additive Manufacturing Process” at the 14th International Conference on Numerical Methods in Industrial Forming processes, NUMIFORM 2023, Krakow, Poland, June 2023.
- Presentation “Numerical Simulation of FFF Process and Tensile Tests” at the 35th DAAAM International symposium on intelligent manufacturing and automation, Vienna, Austria, October 2024.
- Presentation “Thermo-Mechanical Simulation of Material Extrusion-Based Additive Manufacturing Process” at the 2nd Olympiad in Engineering Science international conference, Stavanger, Norway, June 2025.
- Presentation “Development and Mechanical Performance Analysis of Biodegradable Polymers Sustainable for Additive Manufacturing” at a seminar at Istanbul University, Istanbul, Turkey, August 2025.

Structure of the dissertation

The main body of the dissertation comprises three chapters and general conclusions. The literature list contains 280 references. The total scope (excluding the Summary in Lithuanian) comprises 135 pages, 35 figures, 14 tables, and 17 equations. The author’s publications include three journal articles with Web of Science Impact Factors and one conference-proceedings manuscript.

Acknowledgments

The author would like to express his sincere appreciation to the academic supervisor, Prof. Dr Viktor Gribniak, for his invaluable guidance, efforts, and intellectual support throughout the study. Special thanks are extended to Assoc. Prof. Dr Arvydas Rimkus for his constructive contributions and support to the experimental framework. The author is also grateful to Assoc. Prof. Dr Jelena Škamat, Prof. Dr Darius Bačinskas, Prof. Dr Alfonsas Daniūnas, Prof. Dr Arturas Jukna, Assoc. Prof. Dr Nikolaj Višniakov and Prof. Dr Dimitrios Pavlou for their contribution to improving the quality of this dissertation. Finally, the author would like to express his deep gratitude to his family members and friends. Their unwavering emotional support kept him motivated throughout the study.

1

Additive Manufacturing of Fiber-Reinforced Polymer Composites

This chapter presents a literature review of additive manufacturing for fiber-reinforced polymer (FRP) composites, with a focus on FFF technologies. Short-fiber and continuous-fiber reinforcement approaches are reviewed in relation to constituent compatibility, fiber-matrix adhesion, interlayer integrity, porosity formation, and the resulting anisotropic mechanical response of printed components. The chapter also considers developments in recycled and bio-based polymer feedstocks for additive manufacturing, highlighting PLA as a dominant material for FFF research and applications. The influence of FFF thermal history on residual stress formation, dimensional distortion, and temperature-dependent behavior is discussed together with recent progress in numerical modeling of warpage and residual stresses. The chapter concludes by identifying key knowledge gaps and by formulating the dissertation's objective and tasks. The research findings of this chapter are presented in the publication (Farh et al., 2026).

1.1. Fiber-reinforced polymeric composites

Fiber-reinforced polymer (FRP) composites are attracting growing research interest and evolving applications in automotive, construction, and medical fields due to their high strength-to-weight ratio and durability. Continuous fibers are typical reinforcement components. The literature defines the FRP manufacturing process in terms of fabrication techniques such as resin transfer molding (Abusrea et al., 2023; Gauvin & Chibani, 2022), manual layup (Amar et al., 2025; A. Y. Chen et al., 2021), automated tape laying (Yadav & Schledjewski, 2023), spray-up (Hasyim et al., 2023), pultrusion (T. Liu et al., 2020; Pirchio et al., 2023), automated fiber placement, and filament winding (Carosella et al., 2024). However, the molds' limitations constrain product formability, making the fabrication of complex geometries time-consuming and costly. These constraints slow the progress of FRP's innovative applications.

The design flexibility, automated fabrication, and cost constraints led to the development of additive manufacturing (AM) for producing FRP (AM-FRP) parts (Palanikumar et al., 2020). Berman (2012) characterized the AM's strengths and weaknesses, as shown in Figure 1.1. AM technologies refer to the fabrication processes by which digital 3D designs build a physical part layer by layer by depositing material. These technologies extended the horizon of FRP composites engineering for complex geometries, high-performance, and economically efficient products (Gowtham et al., 2024; T. Li et al., 2024; Rimkus et al., 2022; Thakur et al., 2024). Besides, the AM is flexible in controlling fiber orientation, changing fiber volume fraction, and producing functionally graded structures.

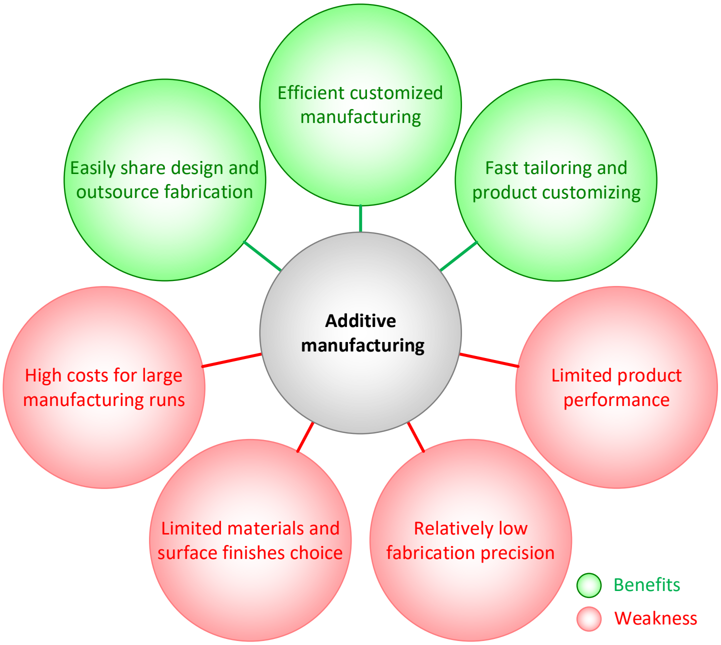

Fig. 1.1. Strengths and weaknesses of additive manufacturing (Farh et al., 2026)

Developing short-fiber-reinforced polymers that exhibit the reliability of the AM process has been an ongoing area of research (Dul et al., 2016; Gray IV et al., 1998; Nikzad et al., 2011; Van Der Klift et al., 2015). However, recent studies (Ding et al., 2023; Iftekar et al., 2023; Maqsood & Rimašauskas, 2021; Safari et al., 2022; Yan Zhang et al., 2021) highlight the need for FRP development using AM technologies' continuous fibers and process modifications, thereby improving the quality and mechanical performance of printed components. The following requirements would help to apply AM technologies to the production of polymeric components reinforced with continuous filaments:

- Minimal material porosity. Minimizing porosity reduces heterogeneity in mechanical performance and improves FRP durability.
- Compatibility of material constituents. The fiber selection criteria should align with the printed parts' purpose to achieve composite interaction between the polymeric matrix and the fiber reinforcement, while accounting for the AM technique's specific characteristics.
- The fibers and polymeric matrix adhesion. The bonding with the matrix allows the fibers to transfer loads and protects the reinforcement from mechanical and environmental effects. Interfacial adhesion also prevents delamination failure, thereby achieving acceptable mechanical performance in the FRP composite.
- Fiber alignment and homogeneity. The AM's ability to control the alignment and distribution of the fibers strengthens the printed parts' sections. In addition, fiber homogeneity and aligned distribution ensure consistent mechanical properties throughout the printed structure.

In addition to the above conditions, the AM technology modification should include equipment technical improvement adopting continuous reinforcement materials (fiber cutting or separate extrusion of polymer and filament) and software development, e.g., uninterrupted path printing, 3D pathways layup, and stitching the printing layers (Dickson et al., 2017; Goh et al., 2018; Iftekar et al., 2023; Karimi et al., 2024). However, these issues are beyond the scope of this work, which focuses on materials.

AM employs the material-layered deposition process to form a physical component from digital 3D design data. This definition comes from the ASTM Committee on additive manufacturing technologies (Martínez-García et al., 2021). Despite the common practice of using the term 3D printing as a synonym for AM, the two terms refer to different processes. In other words, the "rapid printing" or "prototyping" does not adequately describe AM technologies. The continuous material-addition process better reflects the AM ideology, distinguishing it from conventional manufacturing methods based on material removal. Figure 1.2 categorizes three mainstream AM technologies, while this study focuses on fused filament fabrication (FFF), which is the most widely adopted in technical applications (Šostakaitė et al., 2024).

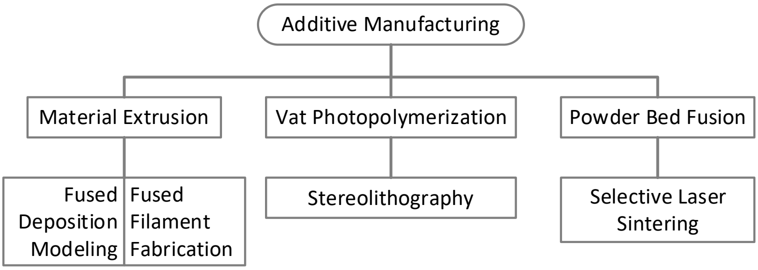

Fig. 1.2. Mainstream processes of additive manufacturing (Farh et al., 2026)

Among various AM techniques, FFF is notable for its accessibility and versatility for thermoplastic polymers (Abusrea et al., 2023). This technology is also known as fused deposition modeling (FDM) and material extrusion (MEX), both of which use filaments. Although “FDM” remains predominant in the scientific literature, it is a trademarked term that does not fully capture the technical specificity of the fabrication process. FFF explicitly denotes the extrusion-based 3D printing process using thermoplastic filaments, whereas FDM is sometimes used generically and can be ambiguous. According to ISO/ASTM 52900 (ISO, 2021), “material extrusion (MEX)” is the standardized process category, while FFF provides a precise designation for the process addressed in this study. Therefore, the terminology “FFF” is retained throughout this dissertation. The relative motion of the nozzle with respect to the platform produces curvilinear layer patterns and complex geometries in a bottom-up manner (Bettini et al., 2017; Dickson et al., 2017; Van Der Klift et al., 2015). Nowadays, it is used in most desktop 3D printers because of its low-cost feedstock and simple operating conditions. The FFF process can use various thermoplastics, similar to injection molding. Thus, it is also applicable to industrial applications. Figure 1.3 sketches the FFF process.

Thermoplastics have low melting temperatures and are typical matrix materials for FFF (Šostakaitė et al., 2024). For example, polylactic acid (PLA) operates at 180–220 °C (L. Cao et al., 2023; Ogaili et al., 2024; Rimkus et al., 2022), acrylonitrile butadiene styrene (ABS) employs 230 °C (Dul et al., 2016, 2018; Rahmati & Zolfaghari, 2024), the melting temperature of the polyamide (PA) varies from 245 °C to 265 °C (Bettini et al., 2017; Dickson et al., 2020; Spoerk et al., 2020), and polypropylene (PP) melts at 170–220 °C (Ainali et al., 2021). Still, some high-performance polymers require high operating temperatures; e.g., polyether ether ketone (PEEK) printing requires 350–420 °C (Doumeng et al., 2021; Pu et al., 2021), and polyetherimide (PEI) melts at 375–420 °C (Kumar & Sathiya, 2021).

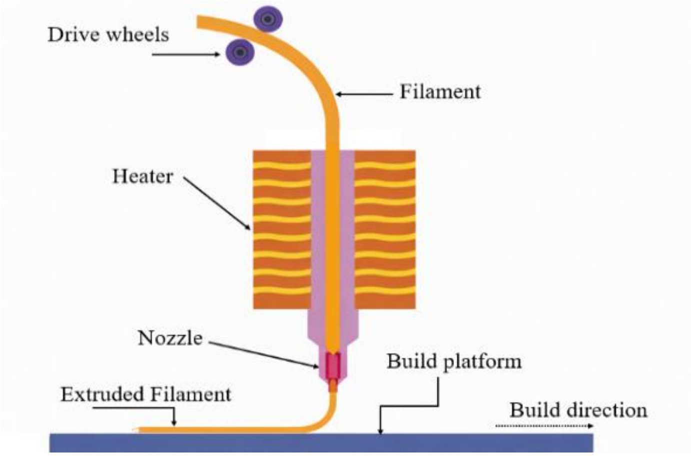

Fig. 1.3. Schematic representation of the fused filament fabrication (FFF) process (created by the author)

However, Šostakaitė et al. (2024) and Karkun and Dharmalingam (2022) suggested PLA and ABS for the construction of mechanically functional components. At the same time, another study proposed PLA as an alternative to ABS due to asthma risks and reduced carbon gas emissions during 3D printing (Mohammadian & Nasirzadeh, 2021). This air-pollution effect explains PLA's recognition as an environmentally neutral polymeric material for FFF. Extensive research (Bettini et al., 2017; L. Cao et al., 2023; Nanya Li et al., 2016; Maqsood & Rimašauskas, 2021; Matsuzaki et al., 2016; Ogaili et al., 2024; Rahmati & Zolfaghari, 2024; Rimkus et al., 2022) has identified the PLA matrix's biodegradability and sufficient mechanical resistance, making it a viable alternative to conventional polymers for developing reinforced composites. Furthermore, the PLA-printed parts are suitable for recycling. For example, Sanchez et al. (2017) and P. Zhao et al. (2018) explored the mechanical properties of recycled PLA produced from FFF-processed filaments. However, multiple recycling cycles degraded the mechanical properties of the 3D-printed material (Sanchez et al., 2017). A comparison of the mechanical properties of virgin and recycled (up to three cycles) PLAs indicated that the third recycling cycle adversely affected material strength and ultimate elongation (Lanzotti et al., 2019). The fifth recycling increased the tensile deformation modulus and strength but decreased the ultimate elongation by 10% (P. Zhao et al., 2018).

Fiber-reinforced PLA composites produced by FFF have attracted significant attention as a route for enhancing the performance of printed parts. Short fibers, ranging from nanometers to millimeters, are used in the FFF process to enhance the mechanical performance of the reinforced composite (Siripongpreda et al., 2023). The literature reports applications of vapor-grown carbon fibers (Shofner et al., 2003) and millichopped fibers of thermotropic liquid-crystalline polymers (Gray IV et al., 1998), glass fibers (L. Cao et al., 2023; Rahmati & Zolfaghari, 2024), and carbon fibers (Goh et al., 2018; Kirubakaran et al., 2025; Maqsood & Rimašauskas, 2021; Ogaili et al., 2024). There has also been growing interest in developing functionalized materials with enhanced electrical transparency (Roper et al., 2014), conductivity (Saari et al., 2015), piezoelectricity (K. Kim et al., 2014), and thermal properties (Stepashkin et al., 2018). Table 1.1(Farh et al., 2026) summarizes the results of the materials characterization reported in the literature (Berman, 2012; Carosella et al., 2024; Dul et al., 2016, 2018; Goh et al., 2018; Kumar & Sathiya, 2021; Nanya Li et al., 2016; G. Liu et al., 2021; Mohammadian & Nasirzadeh, 2021; Nikzad et al., 2011; Pu et al., 2021; Sheikh & Behdinan, 2023; Tian et al., 2017; Vaneker, 2017).

Table 1.1. Effect of fiber on the performance of FFF polymeric matrix composites

Fiber scale	Fiber (%)/ matrix composition	Improvements regarding plain polymeric matrix	References
Nano	MWCNT (0.2 wt%)/PLA	47% and 33% increase in tensile strength and Young's modulus	Berman (2012)
	Graphene (4 wt%)/ABS	8% and 33% increase in tensile strength and Young's modulus	Dul et al. (2016)
	CNT (6 wt%)/ABS	15% and 18% increase in tensile strength and Young's modulus	Dul et al. (2018)
	Graphene (5.6 wt%)/ABS/PLA	Enhanced electrical conductivity and elastic behavior	Sheikh & Behdinan (2023)
	CNT (0.5 wt%)/PLA	28% and 14% increase in yield stress and Young's modulus	Pu et al. (2021)
	CNT (5 wt%)/PEEK	30% increase in the ultimate resistance	Kumar & Sathiya (2021)
	SWCNTs (5 wt%)/ABS	31% and 93% increase in tensile strength and modulus	Shofner et al. (2003)
Micro	Cu (40 vol%)/Fe (10 vol%)/ABS	31% reduction in tensile strength for Fe (45 µm 10 vol%)	Nikzad et al. (2011)
	Bast fiber (10–30%)/PP & Hemp fiber (10–30%)/PP	50% and 143% increase in tensile strength and Young's modulus	Milosevic et al. (2017)
	GF (4–8 wt%)/PLA	54% and 61% increase in ultimate strain and tensile strength	X. Li et al. (2018)

End of Table 1.1

Fiber scale	Fiber (%)/ matrix composition	Improvements regarding plain polymeric matrix	References
Milli	GF (18 wt %)/ABS	51% increase in tensile strength	Carosella et al. (2024)
	CF (40 wt%)/ABS	115% increase in tensile strength	Palanikumar et al. (2020)
	CF (10 wt%)/PA 12	102% and 251% increase in tensile and flexural strength	Mohammadian & Nasirzadeh (2021)
	CF (13 wt%)/ABS	200% increase in tensile strength	G. Liu et al. (2021)
	CF/ABS	Shear strength 14 MPa improved by 20%	W. Zhang et al. (2018)
Meter	AF (4.7 vol%)/PLA	62% and 67% increase in yield strength and ultimate resistance	Rimkus et al. (2022)
	CF (34.5 vol%)/PA	194% increase in the ultimate resistance	Van Der Klift et al. (2015)
	GF (35 vol%)/PA	209% and 33% increase in flexural and tensile strength	Goh et al. (2018)
	CF (34 vol%)//PLA	164% increase in flexural strength	Nanya Li et al. (2016)
	E-GF (54.8 wt%)/PP	800% increase in flexural modulus	Vaneker (2017)
	Recycled CF (8.9 vol%)/PLA	25% and 313% increase in flexural and tensile strength	Tian et al. (2017)
	CF/PA AF/PA GF/PA	386% increase in impact resistance 777% increase in impact resistance 1233% increase in impact resistance	Caminero et al. (2018)

Note: CNT = carbon nanotubes; MWCNT = multi-walled CNT; SWCNT = single-walled CNT; CF = carbon fiber; GF = glass fiber; AF = aramid fiber.

Fiber-reinforced PLA composites produced via FFF have emerged as a promising approach for improving mechanical properties. Short fiber additives can significantly boost the stiffness and often the strength of the polymer, effectively creating lightweight composite materials with superior performance-to-weight ratios (Panerai et al., 2023; Shanmugam, Das et al., 2021). Glass fiber additions can likewise boost modulus by 50% (Bodaghi et al., 2023). In addition to mechanical gains, these rigid synthetic fibers confer greater thermal stability and a higher heat deflection temperature (HDT) on PLA composites, thanks to their low thermal expansion and high heat resistance. Carbon fibers, in particular, have an extremely low coefficient of thermal expansion, which helps constrain the polymer's shrinkage during cooling and can reduce warping and dimensional distortion in printed parts (Tammaro et al., 2024). On the other hand, natural fibers (e.g., wood, flax, hemp, and cellulose) have also been explored as reinforcements for PLA to maintain biodegradability and sustainability. These bio-based fibers are attractive due to their low environmental impact and density; however, their effect on PLA is often mixed: they increase stiffness but can compromise strength due to poorer interfacial bonding and fiber irregularities. Natural fibers thus offer greener composites but usually underperform relative to carbon or glass fiber reinforcements in mechanical metrics (Kennedy et al., 2025).

Table 1.1 shows that the addition of short fibers to PLA generally increases the composite's stiffness (Young's modulus). It can either increase or slightly decrease the composite's ultimate tensile strength, depending on fiber type, content, and dispersion. Neat PLA printed under standard conditions typically exhibits a tensile strength of approximately 50 MPa and a Young's modulus of around 1 GPa, with an elongation at break of a few percent (M. Cao et al., 2022). When reinforced with short carbon fibers (PLA-CF), the material often exhibits a trade-off among strength, ductility, and stiffness. For instance, M. Cao et al. (2022) found that adding a high loading (≈30 vol%) of chopped carbon fiber to PLA increased the modulus by ≈21% (from 1.04 to 1.26 GPa) and slightly improved elongation at break, but the tensile strength dropped by about 9% compared to neat PLA (from 54.5 to 49.4 MPa). The reduction in strength despite the addition of fibers was attributed to microstructural issues, including poor interfacial bonding and fiber agglomeration within the filament, which created stress concentrators. SEM fractography revealed that the PLA-CF fracture surface exhibited numerous pulled-out fibers, voids, and randomly oriented fibers, indicating weak fiber-matrix adhesion and non-uniform fiber distribution. These factors limit stress transfer capacity, undercutting the potential strength gains from the CF.

At the same time, CF at optimum composition may improve mechanical strength. For example, when fiber dispersion and adhesion are better controlled, short carbon fiber reinforcement has been reported to significantly increase PLA tensile strength (e.g., by 50–150% at moderate fiber loadings) (M. Cao et al., 2022). In all cases, the stiffness benefit of carbon fibers is clear, even the poorly bonded PLA-CF composite showed a higher Young's modulus than neat PLA, and the fibers' contribution to load carrying becomes more consistent as their alignment along print pathways approaches unidirectional. Recycled carbon fibers have also been shown to be effective reinforcements in PLA. Tammaro et al. (2024) demonstrated that PLA with 20 wt% recycled CF achieved a 54% higher storage modulus (stiffness in DMA) than neat PLA. They observed that increasing fiber content beyond a small threshold yielded diminishing returns in strength/modulus due to fiber clustering and the reduced aspect ratio of recycled fibers. Still, the overall trend with carbon fillers is improved rigidity and, if processing is optimized, retention or enhancement of strength.

Natural fiber reinforcements in PLA commonly increase the modulus but decrease tensile strength and ductility relative to neat PLA. Siddiqui et al. (2024) studied wood-fiber-filled PLA (20 wt% wood flour) printed at 100% infill and found that, across all build orientations, the composite was weaker than pure PLA. Neat PLA specimens showed a tensile strength up to ≈50 MPa (in the best orientation), whereas the wood-PLA composites reached only around 20–30 MPa, representing a roughly 40–60% reduction in strength when wood fiber is added. On the other hand, Young's modulus of wood/PLA was higher than that of neat PLA. For example, in one orientation, the composite's tensile modulus was ≈1.40 GPa vs. ≈1.2 GPa for the neat polymer. The stiff wood particles thus increased the material's rigidity (and its flexural modulus as well), but at the expense of tensile strength. Wood/PLA samples showed elongation at break dropping to essentially zero (a few percent or less). In contrast, neat PLA can exhibit a 6% strain-to-break, a typical outcome for particle- or fiber-filled brittle matrices. Similar trends are reported with other natural fibers like rice husk, flax, or sisal: moderate fiber loadings (5–20%) tend to improve PLA's stiffness and sometimes impact toughness, but tensile strength often declines as fibers do not carry load effectively past initial elastic deformation. Nonetheless, the consensus is that short natural fibers provide sustainability benefits and stiffness gains but do not reinforce PLA as effectively as carbon or glass fibers in terms of absolute mechanical performance.

The FFF fabrication process can involve micrometer-sized metal powders to improve the mechanical performance of polymeric materials (Nikzad et al., 2011); however, such fillers are more commonly used to modify the electrical properties of polymeric composites (Cheng et al., 2024; Y. Li et al., 2023). The research literature also includes nanosized additives such as graphene (Banupriya et al., 2025; Dul et al., 2016; Y. Wu et al., 2023), single-walled carbon nanotubes (SWCNT) (Shofner et al., 2003), and multi-walled carbon nanotubes (MWCNT) (Dul et al., 2018; Sharifi et al., 2024; Sheikh & Behdinan, 2024). However, pure graphene is expensive and rarely used in polymeric composites (Bhawal et al., 2016); similarly, SWCNTs are rarely used for the same reason (Hisham et al., 2024). Most 3D-printed nanocomposites use MWCNTs (Hisham et al., 2024; Nanya Li et al., 2016). Still, some types of carbon nanotubes may adversely affect the mechanical performance of printed materials (Kavosi et al., 2020; Khare et al., 2014), so such modifications require particular caution when mechanical resistance is essential. For instance, adding 13 wt% of millimeter-sized carbon fibers increased the polymeric composite's tensile strength and elastic modulus by 250% and 400%, respectively (Love et al., 2014). Using 10 wt% SWCNTs resulted in only 39% and 61% increases in these parameters (Shofner et al., 2003).

This mechanical enhancement results from an increase in fiber-matrix contact area, which improves fiber anchorage resistance and, thus, the overall mechanical performance of the FRP composite.

On the other hand, continuous fibers have superior tensile properties compared to short fibers. Carbon, glass, and aramid filaments are the typical continuous reinforcements. Table 1.2 (Farh et al., 2026) summarizes the results of continuous macro-fiber applications. These findings contributed to understanding the structural development required to continuously reinforce polymeric materials. Figure 1.4 highlights the importance of the compatibility condition, ensuring reliable interaction between the matrix and the fiber reinforcement. There has also been a growing interest in developing functionalized materials with a wide range of properties, such as thermal (Stepashkin et al., 2018), electrical conductivity (Saari et al., 2015), piezoelectric (K. Kim et al., 2014), and electric transparency (Roper et al., 2014).

Despite the rapid progress of AM technologies, most systems use a limited range of commercial and proprietary resins, which restricts the development of the products' physical and chemical properties (Kalsoom et al., 2016). Thermoplastics are the typical matrix materials for FFF. PLA is one of the most investigated thermoplastic materials; it operates at 180–230 °C, and the FFF process does not require a heated bed (Plymill et al., 2016).

Table 1.2. Performance analysis of the FFF-fabricated polymeric composites with continuous reinforcement

References	Fiber/matrix type	Benefits	Strength [MPa]
Van Der Klift et al. (2015)	CF (34.5 vol%)/PA	Elastic modulus: 35.7 GPa	475
Bettini et al. (2017)	AF (8.6 vol%)/PLA	The triple and sextuple increases in tensile modulus and strength regarding the unreinforced reference	206
Dickson et al. (2017)	CF (11 vol%)/PA	Elastic modulus: 7.73 GPa Flexural strength: 250 MPa Flexural modulus: 13.0 GPa	216
	GF (10 vol%)/PA	Elastic modulus: 8.42 GPa Flexural strength: 197 MPa Flexural modulus: 4.21 GPa	206
	AF (10 vol%)/PA	Elastic modulus: 4.98 GPa Flexural strength: 126 MPa Flexural modulus: 6.65 GPa	164

End of Table 1.2

References	Fiber/matrix type	Benefits	Strength [MPa]
Goh et al. (2018)	CF (41 vol%)/PA	Elastic modulus: 13 GPa Flexural strength: 430 MPa Flexural modulus: 38.1 GPa	450
	GF (35 vol%)/PA	Elastic modulus: 7.2 GPa Flexural strength: 149 MPa Flexural modulus: 14.7 GPa	600
Nanya Li et al. (2016)	CF (34 vol%)/PLA	Flexural strength: 156 MPa	91
Matsuzaki et al. (2016)	CF jute (40–50 vol%)/PLA	Elastic modulus: 19.5 GPa	185
Tian et al. (2016)	CF (1K bundle, 27 wt%)/PLA	Flexural strength: 335 MPa Flexural modulus: 30 GPa	–
Vaneker (2017)	GF (54.8 wt%)/PP	Flexural modulus: 13.06 GPa	–
Tian et al. (2017)	Recycled CF (8.9 vol%)/PLA	Flexural strength: 263 MPa Flexural modulus:13.3 GPa	260
Caminero et al. (2018)	CF/PA	Impact strength: 82.26 kJm^2	–
	GF/PA	Impact strength: 280.95 kJm^2	–
	AF/PA	Impact strength: 184.76 kJm^2	–
Melenka et al. (2016)	AF/PA	Elastic modulus (4 vol%): 1.78 GPa Elastic modulus (8 vol%): 6.92 GPa Elastic modulus (10 vol%): 9.0 GPa	31.1 58.8 83.0
Hao et al. (2018)	CF (3K bundle)/Epoxy resin	Elastic modulus: 161.4 GPa Flexural strength: 202 MPa Flexural modulus: 143.9 GPa	792.8
T. Yu et al. (2019)	CF (48.7 wt%)/PA	A 40% increase in flexural strength regarding chopped CFRP samples	270.6

Note: CF = carbon fiber; GF = glass fiber; AF = aramid fiber; PA = polyamide; PP = polypropylene.

Babagowda et al. (2018b), Cruz Sanchez et al. (2017), Lanzotti et al. (2019), and P. Zhao et al. (2018) investigated the mechanical properties of recycled PLA produced in filament form. The viability of recycled PLA for AM and a proposed methodology for polymer recycling in FFF have been introduced. The investigation demonstrated the potential to develop AM samples from recycled PLA; however, polymer degradation has been observed due to repeated recycling (Babagowda et al., 2018a). A comparison of the mechanical properties of virgin PLA and recycled PLA (up to three recycling cycles) demonstrated almost the same strength of the once and twice recycled test specimens compared to the virgin

PLA. On the other hand, the third recycling process affected the strength results negatively (T. Yu et al., 2019). A reduction in the tensile strain rate of PLA was observed after repeated recycling. It was found that after five cycles of PLA recycling, the tensile modulus and tensile strength increased, whereas the elongation at break decreased by 10% (Kalsoom et al., 2016). Hao et al. (2018) recommended reducing layer height to improve the mechanical performance of FFF objects.

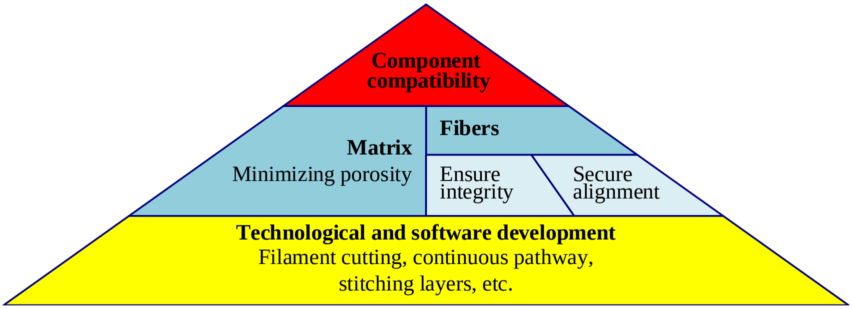

Fig. 1.4. Performance-influencing factors of AM composites with continuous fibers (Farh et al., 2026)

The studies (Paciorek-Sadowska et al., 2019; X. G. Zhao et al., 2018) describe specific requirements for adapting the properties of recycled PLA for 3D printing. Tian et al. (2017) proposed a systematic investigation of innovative research by recycling and remanufacturing process based on 3D-printed PLA carbon fiber composites. The Continuous carbon fiber-reinforced PLA matrix was recycled from 3D-printed components, converted into PLA-impregnated carbon fiber filament, and remanufactured as a feedstock material for the FFF 3D printing process. The carbon fiber content was (8.9 vol%). The results showed an increase in flexural strength (263 MPa) compared with the original 3D-printed samples; however, the flexural modulus decreased from 15 GPa in the original samples to 13 GPa in the remanufactured composite. The improvement in flexural strength was attributed to enhanced fiber-matrix interface.

However, Bettini et al. (2017) highlighted the broad range of PLA applications in FFF research. Among the alternative polymers available on the market, PLA’s low thermal shrinkage and low-temperature printability supported its selection for this study. In addition, a continuous aramid filament reinforces the PLA matrix to prevent the polymeric composite’s brittle failure because of the aramid toughness and high strain at the peak load compared to carbon and glass fibers.

Thermal properties and dimension fidelity: Fiber reinforcements also impact the thermal behavior of FFF PLA composites. Differential scanning calorimetry (DSC) and dynamic mechanical analysis (DMA) reveal changes in thermal transitions and stability due to fiber addition. Carbon and glass fibers, which have higher thermal stability, can increase the thermal degradation threshold and HDT of PLA composites. They also often act as nucleating agents that alter PLA's crystallinity. In one study, the addition of short carbon fibers caused the PLA's cold crystallization temperature to decrease and its crystallinity to more than double (from ≈4% in neat PLA to ≈9% in the composite) (M. Cao et al., 2022). The fibers provided nucleation sites during cooling, promoting the formation of α-phase crystals in PLA that were absent in the pure polymer. This increase in crystallinity can enhance stiffness at moderate temperatures and slightly raise the glass transition temperature (some composites show a marginal increase in T_g of 1–2 °C with fiber addition). In DMA, fiber-filled PLA exhibits a higher storage modulus across the entire temperature range and often shows a smaller drop in modulus beyond the T_g, indicating improved thermal-mechanical stability (Tammaro et al., 2024). Natural fibers can similarly nucleate crystallinity in PLA (although their thermal stability is lower than that of carbon fibers), sometimes resulting in a more pronounced cold-crystallization exotherm in DSC for composites.

Following the principles of composite mechanics (Gribniak et al., 2017), reinforcement integrity ensures that the fibers transfer loads from the polymeric matrix, thereby distributing and shielding the continuous filaments from harsh environmental and mechanical loads. Thus, interfacial adhesion is critical for preventing delamination and ensuring satisfactory mechanical performance of the FRP composite. Proper alignment and uniformity of the fibers guarantee consistent mechanical properties across the printed structure; controlling fiber distribution enhances the reinforcement's efficacy; and reducing material porosity diminishes mechanical property scatter and boosts the durability of FRP composites. Despite the rapid advances in AM technologies (Fig. 1.4), the FRP fabrication industry still relies on a limited range of commercial and proprietary resins, which limits efforts to enhance the product's physical and chemical properties (Kalsoom et al., 2016). Furthermore, the above composite mechanics' conditions are valid only when the composite integrity conditions are satisfied.

1.2. Composite integrity

Following the classification of Lumpe et al. (2019), reinforced polymers belong to the multi-material category, in which inter-fractional integrity affects mechanical performance (Dizon et al., 2018). Another study (Kabir et al., 2020) identified the aspects schematically depicted in Figure 1.5 that affect the mechanical performance of additively manufactured polymeric composites. The AM preparation stage describes the 3D printing design processes that govern manufacturing success and efficiency. For example, the design of printing support determines the essential procedure for complex product topologies (Ezair et al., 2015). Banjanin et al. (2018) further systematized the literature on the key issues affecting the mechanical performance of FFF components.

The manufacturing stage in Figure 1.5 determines the center factors that affect the quality of the AM object (Kabir et al., 2020). Thus, the material parameters mainly determine the mechanical performance of the 3D-printed object. On the other hand, the so-called machine factors describe ME efficiency. In addition, the matrix material is sensitive to changes in moisture content and electrical conductivity, requiring drying and the removal of electric current from the print supply (Chortos, 2022; Kabir et al., 2020; Mora et al., 2020). The process parameters are the most studied factors (Banjanin et al., 2018; Kabir et al., 2020). Summarizing the results reported in the literature (Chacón et al., 2017; Hamel et al., 2018; Hanon et al., 2021; Hetrick et al., 2021; Huang et al., 2019; Lee & Wu, 2020; Ning et al., 2017; Qiao et al., 2008; Reddy et al., 2023; Sood et al., 2010), Table 1.3 (Farh et al., 2026) systemizes the essential effects on mechanical performance.

In addition to the geometric conditions (Table 1.3), the mechanical anisotropy of AM components, arising from layer thickness and filament diameter, contributes to the performance diversity discussed in more than half of the works reviewed by Reddy et al. (2023). This trend is consistent with the results in Table 1.3, indicating a controversial effect of layer thickness on the mechanical performance of AM parts, especially in the presence of fiber reinforcement. In addition, the raster pattern determines the current research object in the literature, thereby optimizing the AM objects' weight and stiffness (strength), e.g., (Gribniak et al., 2022; Misiūnaitė et al., 2025; Šostakaitė et al., 2024).

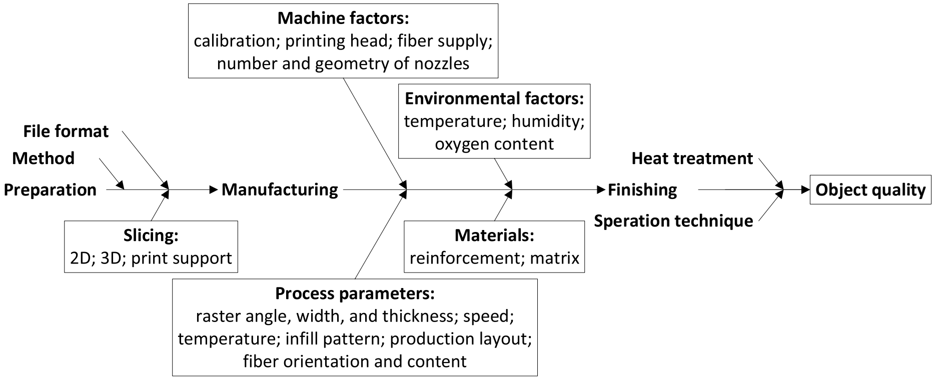

Fig. 1.5. Factors affecting AM quality (Farh et al., 2026)

Table 1.3. Effect of the FFF settings on the mechanical performance of the material

Parameter	Effects	Results	References
Printing speed	Minimal effect on the tensile strength until a certain speed; substantial impact on costs.	The strength decreases when a specific speed limit is exceeded.	Chacón et al. (2017), Huang et al. (2019), Ning et al. (2017), and Reddy et al. (2023)
Raster or bed angle	Essential effect on the tensile strength, toughness, and ductility of reinforced material with 100% infill.	A ±45° raster reduces strength but increases toughness and ductility (compared to a 90° raster).	Bhandari et al. (2019), Chohan et al. (2020), Hamel et al. (2018), Hanon et al. (2021), Hetrick et al. (2021), Lee & Wu (2020), Ning et al. (2017), Rayegani & Onwubolu (2014), and Sood et al. (2010)
	Rastering does not affect the tensile strength of the neat polymer at 100% infill.	The modulus of elasticity decreases by 30%, increasing the cross-section from 6×1.25 mm to 13×8 mm.	Huang et al. (2019), Neng Li et al. (2019)
Raster pattern	Substantial effect on tensile, compression, flexural, and impact properties.	The maximum tensile strength of 34.2 MPa for PLA + CF was achieved with 0° orientation, 100% infill, and a 0.3 mm layer thickness.	Reddy et al. (2023)
		A solid pattern is less efficient in terms of impact resistance (due to limited energy absorption) and ultimate elongation.	Hanon et al. (2021), Qiao et al. (2008)
		A significant correlation appeared between the number of shells and flexural stiffness.	Hamel et al. (2018)

End of Table 1.3

Parameter	Effects	Results	References
		The maximum 36.9…37.9 MPa tensile strength of the ABS part at 0° orientation and 50°…60° raster.	Rayegani & Onwubolu (2014), Sood et al. (2010)
		The maximum 2390 kJ/m^2 impact strength of the ABS part at 30° orientation and 60° raster.	Chohan et al. (2020)
Build direction	The most stable sample orientation ensures better mechanical performance.		Caminero et al. (2018), Chacón et al. (2017)
Layer thickness	The reduction in thickness improves packing density and interlayer adhesion.		Ning et al. (2017)
	A thick raster increases the bonding surface temperature and improves the layer bond performance and impact resistance.		Caminero et al. (2018), Sood et al. (2010)
	Short carbon fibers reduce inter-layer bonding performance.	CF increases the porosity of ABS, especially at a 45° raster.	W. Zhang et al. (2018)
Annealing		Annealing tripled the interlayer bonding strength.	Bhandari et al. (2019)

The lightweight polymeric materials demonstrate sufficient mechanical resistance for load-bearing applications (Neng Li et al., 2019; Šostakaitė et al., 2024). However, AM parts should replace conventionally fabricated components, maintaining equivalent mechanical performance (Dizon et al., 2018; Shanmugam, Rajendran, et al., 2021). Increasing performance requirements drive the advancement of polymeric materials through polymer modifications or through reinforcement of compositions. On the other hand, the thermo-mechanical properties of polymer-based composites still need improvement (Nikzad et al., 2011). Another study (Motaparti et al., 2017) demonstrated that the strength of an FFF component is directly related to the intermolecular diffusion occurring across the boundary between the fused filaments. The significance of bond quality between neighboring filaments depends on the printing parameters and the polymer's melt viscosity (Cicala et al., 2018). Reinforcement can address mechanical performance limitations (Kumar & Sathiya, 2021).

Although various reinforcement options exist, continuous filaments outperform short fibers in terms of mechanical strength (Goh et al., 2019). The layered structure and anisotropy of a 3D-printed reinforced plate are similar to those of a composite laminate (Ramesh et al., 2021). Thus, Tian et al. (2017) reported a tensile strength of 260 MPa for the additively manufactured PLA composite with continuous carbon fibers. The entire reinforcement filament system ensures mechanical properties comparable to those of pultruded materials (Goh et al., 2019). Figure 1.6 illustrates the relationship between fiber volume content and the tensile strength of polymeric composites. Remarkably, Figure 1.6 considers the short-term performance of the composite. However, creep and aging mechanisms substantially reduce the long-term resistance of polymeric composites. For instance, the 0.35 and 0.8 coefficients reduce the strength of GFRP and CFRP pultruded bars for structural design purposes. Another study (Rossini et al., 2019) discussed this issue in detail. The biodegradability of the materials further complicates the estimation of the mechanical performance of AM-reinforced composites (Hedayati et al., 2020).

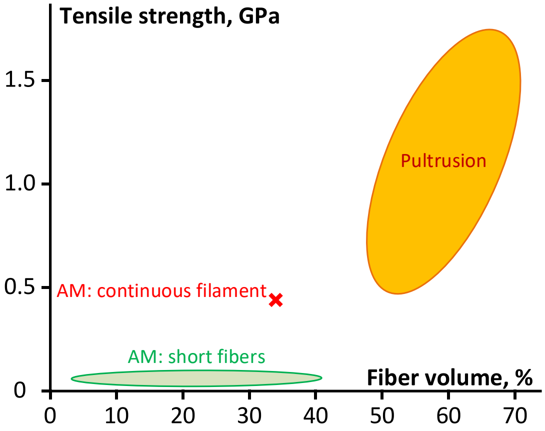

Fig. 1.6. Fiber effect on the tensile strength of polymeric materials (Farh et al., 2026)

Typical fibers, especially carbon fiber, have smooth surfaces devoid of active groups that can interact with the polymer matrix. Modifying the interface may enhance and solidify the contact between the fiber and polymer. Methods for interfacial modification in non-AM FRP composites have been extensively developed and thoroughly examined (L. Liu et al., 2015). Research on fiber surface modifications and the incorporation of coupling agents in AM composite materials has primarily focused on FFF (Caminero, Chacón, García-Moreno, & Reverte, 2018; Filgueira et al., 2017) and SLA and SLS (Jing et al., 2017; Kleijnen et al., 2017; Yan et al., 2011) technologies. However, the fiber-matrix interface in FFF technology for load-bearing composite materials has not been explicitly explored (Bettini et al., 2017; Rimkus et al., 2022). In particular, additional research is needed to develop surface modifications for carbon fibers in FFF-based composite materials to achieve optimal mechanical, optical, and electrical properties.

1.3. Continuous reinforcement technologies

The evolution of AM technologies for continuous fiber composites has progressed over recent decades, leading to the development of various reinforcement methodologies. Categorizing these approaches is challenging due to the field's foundational complexity. The prevailing basis for classification focuses on how the thermosetting matrix and reinforcing fibers are supplied to the printing head and on how material deposition occurs during fabrication.

In-situ impregnation is a continuous-fiber AM approach in which dry fibers are impregnated directly within the heated printhead, immediately before deposition, by contacting the fiber bundle with a molten thermoplastic or low-viscosity thermosetting resin during extrusion (Varma et al., 2022). The impregnated tow is then extruded through the nozzle and consolidated on the build surface as a composite bead, building the part layer by layer. For thermoset systems, rapid solidification can be achieved using integrated ultraviolet (UV) curing or localized heating near the nozzle, reducing dependence on long, high-temperature post-curing cycles. By avoiding pre-impregnated feedstock, the method increases flexibility in fiber-matrix selection, reduces material costs and storage constraints, and enables independent control of fiber and matrix feed rates, allowing local adjustment of reinforcement content. Because impregnation occurs immediately before placement, wetting and consolidation can be promoted while the material remains hot, thereby improving interfacial adhesion and interlaminar integrity when process conditions are well controlled. The technique is also attractive for large-scale parts and complex reinforcement layouts, since fiber placement can be tailored along selected toolpaths. Key challenges include achieving sufficient infiltration within the nozzle's limited residence time, maintaining stable fiber tensile strength to avoid waviness or buckling, and controlling bead compaction to limit voids and ensure consistent consolidation.

The prepreg extrusion technology employs pre-impregnated fibers coated with a thermoset or thermoplastic resin to distribute the matrix material uniformly (Dickson et al., 2020). Typically, the process uses two print heads: the first extrudes a thermoplastic material to form the external layers and the path that includes the reinforcing fiber; the second extrudes the pre-impregnated fiber compound. This continuous fiber, coated with a thermoset, is deposited into the designated path created by the first nozzle. The partially cured resin in the prepreg minimizes the need for extensive post-processing, thereby accelerating production cycles. Commonly employed matrix materials include PLA, PC, PETG, and PA;

reinforcement fibers include glass, carbon, and aramid (Pokorný et al., 2023). In practice, this strategy improves process stability because the fiber-matrix ratio and wet-out quality are defined during filament manufacturing, thereby reducing variability associated with on-head impregnation and facilitating consistent deposition. The approach also enables high fiber continuity along the programmed toolpath, supporting efficient load transfer in the primary reinforcement direction. However, the use of pre-impregnated feedstock imposes constraints on fiber routing and minimum bending radius, and the fixed reinforcement content limits the ability to vary the fiber volume fraction locally within a single part.

The foundational principle of the prepreg coextrusion technique is continuous composite fiber extrusion (Y. Yang et al., 2023), in which the fiber core, preimpregnated with a thermoset matrix, is combined with a thermoplastic material that serves as an adhesion layer between the composite layers. This approach incorporates two nozzles: one extrudes composite fiber, and the other extrudes thermoplastic material. The heated nozzle combines thermoplastic filament with pre-impregnated fibers to co-extrude the material onto the print platform, forming the object; the second nozzle deposits thermoplastic filament to create external layers. This technique enables precise control over the volumetric fiber content within the final component. Commonly used matrix materials include PLA, TPU, PC, PETG, and PA, while reinforcement fibers may be made of glass, carbon, or basalt.

The in-line impregnation technique combines conventional fibers with the deposition of thermosetting material using AM methods. It leverages the design flexibility of robotic deposition in AM while maintaining the mechanical advantages of typical fabrication processes. In this method, dry fibers are impregnated with a thermosetting material, such as epoxy resin, through a resin bath before entering the heated printing head. The impregnated fibers are then deposited onto the build platform through a nozzle (Rimašauskas et al., 2019). A key advantage of in-line impregnation is the use of raw fibers, which are less expensive than pre-impregnated materials, enabling the production of parts with customized composite properties. This technique uses vinyl esters, acrylics, and epoxy resins as matrix materials, with reinforcement fibers such as continuous carbon, glass, basalt, aramid, and natural fibers.

In-situ consolidation is primarily based on the automated fiber placement approach. This technique is enhanced by incorporating FFF, enabling a wide range of material-building options. Pre-impregnated fiber strips, typically coated with thermosetting resins such as epoxy, are deposited directly onto a build plate or mold fabricated using FFF (Struzziero et al., 2021). During deposition, the fiber strip passes through a nozzle and is pressed onto the matrix by a drum, which is heated by an external source to facilitate on-the-spot curing. The method's heat-treatment compatibility allows the use of high-performance thermoplastics from the PAEK family (PEK, PEEK, PEKK, etc.), low-temperature thermoplastics (e.g., PA and ABS), and even water-soluble thermoplastics for matrix construction. Each layer is fully bonded and solidified during deposition, ensuring superior mechanical and dimensional properties for the final component while significantly reducing curing time. This approach is particularly advantageous for manufacturing high-performance parts with complex geometries and stringent tolerances, where precision and strength are crucial. Carbon and glass fibers are the primary reinforcements, and the reinforcement and matrix materials are largely consistent with those used in related technologies.

1.4. Mechanical performance of composites

Typical studies employ standard mechanical testing methods to characterize mechanical properties, such as strength, impact resistance, and hardness. Still, reinforcement integrity is essential in AM for structural applications, as it controls material performance during fabrication, unlike in conventional production processes (Dizon et al., 2018; Ghebretinsae et al., 2019; Lumpe et al., 2019). Therefore, the characterization of multi-materials requires specific procedures. Numerous studies have investigated the influence of FFF processing on mechanical performance (Blanco et al., 2014; Cazón et al., 2014; Kęsy & Kotliński, 2010; Ryu et al., 2019), thermo-mechanical properties (Akbari et al., 2018; Blanco et al., 2014; Reichl & Inman, 2018), and manufacturing accuracy (Hong et al., 2018; Khoshkhoo et al., 2018; Yap et al., 2017). The lack of standardized test methods for the mechanical performance of AM parts (Chacón et al., 2017) leads to diverse methodologies reported in the literature.

Table 1.4 (Farh et al., 2026) summarizes the experimental results published in the literature. It shows that ABS and PLA are typical AM materials, consistent with observations by Ramesh et al. (2021). This table includes the following standardized test methods: ASTM D638-14 (ASTM International, 2014a) and ASTM D638-10 (ASTM International, 2010a) for tensile properties of plastics; ASTM D3039-17 (ASTM International, 2017) and ASTM D3039-14 (ASTM International, 2014b) for tensile properties of polymeric composites; ASTM D790 (ASTM International, 2010b) for flexural properties; ASTM D6110 (ASTM International, 2018) for Charpy impact resistance; ASTM D256 (ASTM International, 2006) for impact resistance; ASTM D3518-13 (ASTM International, 2013) for in-plane shear response; ASTM D7264-07 (ASTM International, 2007) for flexural properties of polymeric composites; ISO 527 (ISO, 2012) and ISO R527 (ISO, 1966) for tensile properties; ISO 179 (ISO, 1982) for Charpy impact properties; ISO R178 (ISO, 1975) for flexural properties; GB/T 1040 (SAC, 2006) for tensile properties; and GB/T 9341 (SAC, 2008) for flexural properties.

Table 1.4. Characterization of fused filament fabrication parts

References	Material	Test/sample, loading speed	Standard	Results
Rimkus et al. (2022)	PLA, infill 100%	Tension/dumbbell-shaped	ASTM D638-14	39.3…44.8 MPa
	PLA + aramid	Tension/tabbed plate	ASTM D3039-17	47.3…54.1 MPa
Van Der Klift et al. (2015)	PA + CF	Tension/ tabbed plate, 2 mm/min	–	128…516 MPa
Caminero et al. (2018)	PA + CF, GF, and AF	Charpy impact/notched prism, 10 J	ASTM D6110	19.5…285 kJ/m^2
W. Zhang et al. (2018)	ABS + short CF	Shear/notched tabbed plate	ASTM D3518-13 ASTM D3039-14	10.6…43.0 MPa
Chacón et al. (2017)	PLA, infill 100%	Tension/dumbbell-shaped, 2 mm/min	ASTM D638-10	18.9…89.3 MPa
		Bending/prism, 2 mm/min	ASTM D790-10	3.14…4.52 GPa
Huang et al. (2019)	ABS HP181 infill 100%	Tension/dumbbell-shaped, 5 mm/min	GB/T 1040.2:2006	12.0…33.6 MPa
		Bending/prism, 20 mm/min	GB/T 9341:2008	27.3…64.4 MPa
		Impact/notched prism	ASTM D256-06	4.64…21.51 kJ/m^2
Reddy et al. (2023)	PLA + CF, infill 60…100%	Tension/dumbbell-shaped, 10 mm/min	ASTM D638	13.9…34.2 MPa
Hanon et al. (2021)	PLA, infill 10…90%	Tension/dumbbell-shaped, 10 mm/min	ISO 527-2:2012	9.57…58.3 MPa
Lee & Wu (2020)	PLA + short CF, infill 40…60%	Tension/dumbbell-shaped	ASTM D638	28.7…34.1 MPa
		Charpy impact/notched prism	ASTM D6110	8.33…14.0 mJ
Hetrick et al. (2021)	Onyx + aramid, infill 100%	Charpy impact/notched prism	ASTM D6110-18	1.92…35.3 J
Vălean et al. (2020)	PLA, infill 100%	Tension/dumbbell-shaped, 2 mm/min	ISO 527-1:2012	38.8…51.5 MPa

End of Table 1.4

References	Material	Test/sample, loading speed	Standard	Results
		Modulus of elasticity/ dumbbell-shaped	–	2.41…4.42 GPa
Hamel et al. (2018)	PLA, infill 20…80%	Bending/178 mm prism, AMT SSA 1000 (Structural Stress Analyzer) education device	–	AM optimization process
Rayegani & Onwubolu (2014)	ABS P400	Tension/dumbbell-shaped	ISO R527:1966	3.95…38.9 MPa
Sood et al. (2010)	ABS P400	Tension/dumbbell-shaped, 1 mm/s	ISO R527:1966	9.12…18.1 MPa
		Bending/prism, 2 mm/s	ISO R178:1975	18.8…39.2 MPa
		Impact/notched prism, 3.8 m/s	ISO 179:1982	343…482 kJ/m^2
Chohan et al. (2020)	ABS P400	Tension/dumbbell-shaped	ASTM D638	17.2 MPa
		Bending/prism	ASTM D790	16.1 MPa
		Impact/notched prism	ASTM D256	2390 kJ/m^2
Bhandari et al. (2019)	PETG and PLA with short CF	Tension/dumbbell-shaped cut, 5 mm/min	ASTM D638-14	6.81…38.7 MPa
Ghebretinsae et al. (2019)	Onyx + CF	Tension/tabbed plate, 1 mm/min	ASTM D3039	538…585 MPa
		Bending/prism, 1 mm/min	ASTM D7264-07	242…303 MPa
Ray et al. (2003)	PLA + CN	Bending/plate, 2 mm/min	ASTM D790	86…134 MPa

Note: AF = aramid fiber; CF = carbon fiber; GF = glass fiber; ONYX = Nylon 6 + chopped CF; CN = carbon nanoparticles.

Most tensile tests use dumbbell-shaped samples ASTM D638 for both reinforced and plain polymer samples, except for resin-matrix composites reinforced with oriented filaments (modulus of elasticity exceeding 20 GPa), for which testing follows ASTM D3039. In addition, since the existence of an elastic limit in polymeric materials represents a rough approximation, the adequacy of the generally accepted “elastic modulus,” “stiffness,” and “rigidity” definitions is questionable. Moreover, the exact stress-strain characteristics of polymeric materials depend strongly on factors such as the rate of stress application, temperature, and load history. In addition, the AM printing pathways affect the polymer structure, further compromising the adequacy of the above characteristics. The ±45° raster is typical in manufacturing layouts and is particularly effective at resisting shear and torsion (Ramesh et al., 2021). At the same time, unidirectional samples exhibited the highest mechanical performance (both resistance and stiffness) along the fiber direction; however, such elements are prone to interlayer splitting failure (Caminero et. al., 2018; Rimkus et al., 2022; Van Der Klift et al., 2015).

The growing need for new designs for additive manufacturing (DfAM) to ensure an optimal engineering performance of AM parts is evident. In this context, the optimization procedure proposed by Hamel et al. (2018) represents a remarkable achievement: the Pareto set of processes determines the AM settings for building functional parts, enabling engineers to optimize them for specific process conditions without additional testing. Rayegani and Onwubolu (2014) examined the relationships between building orientation, raster angle, and pathway overlap (air gap) and the tensile strength of ABS polymer parts. Moreover, Chohan et al. (2020) employed a neural network optimization algorithm to relate printing setup and mechanical performance parameters of ABS parts; the laboratory tests demonstrated prediction errors of less than 3%. However, the analysis of Table 1.4 reveals that only impact resistance is optimized, consistent with the literature results (Hanon et al., 2021; Rayegani & Onwubolu, 2014; Sood et al., 2010).

The appearance of continuous reinforcement complicates the prediction of mechanical performance. Therefore, Ghebretinsae et al. (2024) and Rimkus et al. (2022) employed finite element (FE) modeling to analyze the load-bearing capacity of reinforced AM composites. The comparative analysis of the modeling and experimental results revealed substantial room for improvement in FE predictions when voids and layer imperfections are accounted for. On the other hand, FE simulations can serve as an idealized reference to improve the quality of AM processes (Gribniak et al., 2021a; Misiūnaitė et al., 2025; Rimkus et al., 2022).

Since AM uses a layer-by-layer construction method, the bond quality between adjacent layers perpendicular to the loading direction affects the strength of the fabricated components. The literature analyzes the interlayer characteristics of AM in thermoplastics, including interlayer bonding resistance (Gan, 2009), crosswise tensile strength, interlaminar shear strength (Gupta & Ogale, 2002), and interlaminar fracture toughness (L. Liu et al., 2015). It was found that the tensile properties in the plane are superior to those in the direction orthogonal to the manufacturing path across different AM techniques, including FFF (Goh et al., 2019), SLS (Lordi & Yao, 2000), and inkjet (X. Xu et al., 2002). In the poly-jet method, the ultimate tensile strength measured in the direction transverse to the fabrication pathway was only 60% of the in-plane strength (X. Xu et al., 2002). Jing et al. (2017) reported high fracture strains in the manufacturing direction of SLS specimens, leading to interlayer brittle fracture in the perpendicular direction, which requires particular care in load-bearing components. The fiber-matrix interfacial shear stress, influencing stress transfer, determines the impact toughness, off-axis strength, and functional performance of FRP composites (Liao et al., 2018). Most studies assessed interfacial properties through SEM images (Turner & Gold, 2015).

Modifying the interface structure and arrangement may improve the mechanical performance (W. Zhang et al., 2018). Still, optimizing this part of the internal structure remains limited, as most existing research focuses on the macroscopic mechanical properties of composite materials. Thus, a more detailed exploration is needed to identify the mechanisms of interfacial resistance in composites across three levels: macroscopic, mesoscopic, and microscale (Nakagawa et al., 2017). Macroscopic methods can assess the interfacial adhesion between fibers and the polymer matrix. Nevertheless, these experimental methods focus on qualitative comparisons of interfacial bonding characteristics and cannot adequately measure the interfacial strength. Therefore, the literature lacks a quantitative analysis of the fiber-to-matrix interfacial characteristics of AM composites. Additionally, the temperature gradients associated with FFF processes necessitate further research into their effects on the composite interface (Melenka et al., 2016). The fiber-matrix interaction models require an understanding of micro- and nanomechanical interlocking, residual stresses arising from differences in the coefficients of thermal expansion, nonbonding energy, and sliding-frictional stress (Araya-Calvo et al., 2018; Gardner et al., 2016).

1.5. Influence of fused filament fabrication parameters on the mechanical performance

Young et al. (2018) compared the interlayer properties of the FFF-fabricated pure polymers with those of their counterparts produced using conventional techniques. So, the interlayer fracture toughness of the compression-molded polymers was four times higher (6.11 kJm2) than that of the FFF polymeric material (1.57 kJm2). In FFF, reducing printing speed, bed temperature, and layer thickness, and increasing nozzle temperature, enhances interlayer bonding (Chacón et al., 2017; Hamel et al., 2018; Hanon et al., 2021; Huang et al., 2019; Reddy et al., 2023). Interlayer adhesion decreases with increasing fiber content. The higher thermal conductivity of the fiber compared to the polymeric matrix leads to lower interlaminar shear strength in composite materials due to increased cooling rates and reduced bond-forming time (Xie et al., 2002; N. Zhang et al., 2023).

Layer thickness is crucial in determining strength and stiffness. Studies (Hanon et al., 2021; Ning et al., 2017) have shown that a thin layer enhances interlayer bonding, thereby improving tensile and flexural strength in PLA and HT-PLA. This enhancement maximizes interlayer bonding while maintaining dimensional accuracy. However, for certain composites, such as continuous carbon fiber-reinforced thermoplastics, a layer thickness of 0.125 mm may yield the best results by balancing print quality and strength (Caminero et al., 2018; Chohan et al., 2020). N. Zhang et al. (2023) observed a reduction in shear strength from 13 MPa to 10.5 MPa when the layer thickness and printing speed were increased from 0.18 mm to 0.3 mm and from 60 mm/s to 100 mm/s, respectively.

The effect of printing speed on mechanical properties is particularly notable in pure and carbon fiber-reinforced ABS materials. Lower speeds, such as 60 mm/s, were optimal for achieving higher tensile and shear strengths in fiber-reinforced ABS, as slower speeds allow better interlayer bonding (Huang et al., 2019; W. Zhang et al., 2018). Increasing speed often introduces voids and weakens mechanical performance due to inadequate interlayer fusion (Lee & Wu, 2020).

Orientation during printing significantly influences the tensile, flexural, and impact resistance of the printed parts. Aligning layers with the loading direction yielded the highest tensile strength, as fibers aligned parallel to the load direction demonstrated greater load-bearing capacity than other configurations (Rayegani & Onwubolu, 2014; Sood et al., 2010). Nikzad et al. (2011) reported a 42% increase in tensile resistance in the orthogonal direction to the production pathway in ABS reinforced with carbon fibers compared to pure ABS. Thus, the fibers strengthen in-plane properties but reduce the interlayer adhesion. The raster angle affects layer alignment and load distribution. A 45° raster angle generally optimizes tensile and impact performance, particularly in fiber-reinforced composites, by enabling efficient load transfer and interlayer interaction (Hamel et al., 2018; Hetrick et al., 2021; Lee & Wu, 2020; Qiao et al., 2008; Vălean et al., 2020).

Nozzle temperature affects layer bonding and, in turn, tensile and flexural strength. Higher temperatures improve material flow and bonding, but must be optimized to prevent overheating and warping. For example, 230°C was optimal for FRP composites, enhancing layer adhesion and mechanical performance without compromising part geometry (Chohan et al., 2020; Ramesh et al., 2021). Similarly, a 200°C–220°C range is used for other materials, such as carbon fiber-reinforced PLA, where strong interlayer bonding is essential to maximize tensile properties (Hanon et al., 2021; Ning et al., 2017). Filgueira et al. (2017) also found that increasing the nozzle temperature from 210 to 240 °C increased PLA fracture toughness from 2167 J/m² to 3907 J/m².

The infill percentage (the density of the interior mesh) is a crucial parameter that affects mechanical properties, especially in composites. Higher infill densities generally produce stronger and stiffer parts, since more material is present to bear load. Studies on PLA and PLA-CF have shown that increasing infill from low levels (20–30%) up to intermediate levels (50–70%) can markedly improve tensile strength and modulus. For example, Gunasekaran et al. observed that raising infill from 10% to 50% roughly doubled the tensile strength of PLA prints. In composites, sufficient infill is needed to form continuous load paths; sparse infill can leave unsupported fiber ends and large voids that act as defects. However, beyond a certain point, the benefits of higher infill diminish. Interestingly, extremely high infill (near 100% solid) does not always yield the toughest parts: fully dense prints may suffer from residual thermal stresses and lack energy-absorbing void space. One study on short-glass-fiber PLA composites found that samples with 50% and 75% infill exhibited higher overall toughness (energy absorption) than those with 100% infill (Plamadiala et al., 2025). The presence of some porosity or cellular structure allowed those parts to absorb more deformation energy before failure, whereas the 100% infill samples, being very stiff and constrained, fractured more abruptly. Infill patterns also play a role: different lattice geometries (grid, hexagon, gyroid, etc.) at the same nominal infill percentage yield different effective densities and stress distributions. Guessasma and Belhabib (2022) showed that, for a given infill rate, the infill pattern influenced the achieved part density and tensile performance; for example, a gyroid infill might produce a stronger part than a rectilinear infill at equal infill content due to better load transfer. Thus, the internal architecture of FFF parts introduces an "architectural randomness" or variability in properties: the arrangement of filament beads and voids means the material is not a continuous solid but a periodic structure. Short fibers within those beads may further accentuate anisotropy, as they tend to align with the print extrusion direction, resulting in higher strength along filament paths than across layers. If the infill lines are discontinuous or non-uniform, the fibers can be irregularly oriented, reducing composite efficiency. Optimizing infill density and pattern is therefore critical for fiber-reinforced prints to ensure sufficient load-bearing continuous fiber networks while minimizing weight and avoiding large stress concentrations from pores or misaligned fibers.

Although the multidirectional fibers are printed layer by layer, the through-thickness fibers may introduce anisotropy. Quan et al. (2015) developed FFF-based technology to fabricate multi-directionally reinforced composites, such as 3D-braided structures, but further development is needed to achieve efficient through-thickness reinforcement and overcome the anisotropic properties of FRP composites. The literature indicates that precise process control is critical to maximizing the FFF potential for producing high-performance composite structures; careful optimization of fabrication parameters will further enhance the strength, stiffness, and overall durability of polymeric composites.

1.6. Design for additive manufacturing

FRP composites offer advantageous material properties, making them highly desirable for various applications and attracting substantial interest from academia and industry. Still, conventional methods do not ensure the efficient fabrication of FRP composites (Kabir et al., 2020). For instance, variable-stiffness (VS) composites allow fibers to follow curvilinear paths within the building plane, thereby modifying load paths, improving stress distribution, and enhancing structural performance. However, fabricating VS composites using traditional methods, such as hand layup, is challenging because accurately directing fiber orientation is difficult. AM addresses this challenge by providing an automated, precise method for aligning fibers with computer-aided design (CAD) specifications, thereby enabling the production of complex FRP composites (Punera & Mukherjee, 2022): the AM technologies open previously inaccessible design spaces for FRP composites by enabling multi-scale topology optimization.

This investigation focuses on the FFF, the most widely adopted AM process for fabricating FRP composites using short and continuous fibers. One of the earliest studies (Christian et al., 2001) on the feasibility of fabricating short-fiber-reinforced composites using the FFF process demonstrated the integration of fibers into the filament feedstock. The ME technique has also proven particularly effective for fabricating continuous fiber-reinforced composites (Rimkus et al., 2022; Van Der Klift et al., 2015).

The design for additive manufacturing (DfAM) is categorized into four phases (Wiberg et al., 2021): component selection, design optimization, manufacturing preparation, and post-processing. The initial phase emphasizes component selection and assembly design. The second phase focuses on design support, involving CAD and optimization techniques. The third phase focuses on applying rules, software, and simulation methods to support and validate manufacturing success. In the final phase, the component undergoes adaptation and preparation for post-processing, including detachment from the build plate, removal of support structures, heat treatment, and surface improvement.

One of the essential benefits of DfAM is its ability to facilitate topology optimization (TO), in which the geometry is modified by varying the spatial density of mesh elements (Rezaie et al., 2013). This method is widely used in the conceptual design phase to minimize material use while maintaining structural integrity and performance. For FRP composites, strategically placing material where it is most needed improves strength-to-weight ratios (Y. Xu et al., 2024). In the DfAM for FRP composites, most TO algorithms employ finite element analysis, thereby discretizing the design domain.

Design strategies for AM-FRP composites focus on integrating the TO and fiber paths. Computation algorithms, such as the penalized solid orthotropic material method, allow simultaneous optimization of material distribution and fiber orientation (Y. Xu et al., 2024; Zhe Yang et al., 2022). This strategy maximizes the mechanical performance of the manufactured part by aligning fiber paths with the load-bearing directions, resulting in lightweight, efficient composites. The resulting output is typically a vector map of short fibers that specifies their orientations and positions. Process planning supports the creation of toolpaths that replicate this vector map, thereby fabricating continuous fibers that influence the mechanical performance of the final composite components. Toolpath generation is particularly significant when designers leverage AM to produce continuous fiber-reinforced composites; this generation follows the TO stage (Jiang et al., 2019; Y. Xu et al., 2024; Zhe Yang et al., 2022).

Yang et al. (2022) found that the TO of continuous FRP composites improved stiffness by 30% compared to traditional methods. Additionally, the stiffness-to-weight ratio improved by 26%, proving the substantial benefits of optimized material distribution in lightweight applications such as aerospace. Continuous fiber angle optimization ensures optimal fiber orientation for maximum stiffness and strength, while also achieving significant weight reduction in AM components (Chohan et al., 2020; S. Li et al., 2020). The optimized fiber path resulted in a 35% increase in tensile strength compared to non-optimized designs (Jiang et al., 2019). These examples demonstrate the effectiveness of design optimization for AM and identify areas for further investigation. However, the effectiveness of FFF composites requires optimizing key process parameters, including layer thickness, printing speed, nozzle temperature, bed temperature, and infill density, as summarized in Table 1.5 (Farh et al., 2026). This table demonstrates the potential for DfAM optimization and identifies the focus for further research.

Table 1.5. Optimizing fused filament fabrication for mechanical performance

References	Materials	Tested properties	Optimal parameters	Improvement results
Caminero et al. (2018)	PA + CF/GF/AF (long)	Impact resistance	BO: on-edge; LT: 0.10–0.125 mm; RA: 0	CF: from 24.7 kJ/m^2 to 82.3 kJ/m^2; GF: from 86.3 kJ/m^2 to 281 kJ/m^2; AF: from 86.4 kJ/m^2 to 185 kJ/m^2
W. Zhang et al. (2018)	ABS + CF	Tensile and shear strength	LT: 0.18 mm; PS: 60 mm/s; RA: 0	Tensile strength from 13.7 MPa to 39.1 MPa; Shear strength from 12.0 MPa to 16.5 MPa

Continued Table 1.5

References	Materials	Tested properties	Optimal parameters	Improvement results
Ning et al. (2017)	PLA + CF	Tensile strength, modulus of elasticity, toughness	ID: 100%; LT: 0.15–0.25 mm; NT: 220 °C; PS: 25 mm/s	Tensile strength from 19.2 MPa to 36.8 MPa; Toughness from 903 kJ/m^3 to 2040 kJ/m^3
Chacón et al. (2017)	PLA	Tensile and flexural strength	BO: on-edge; LT: 0.06 mm; PS: 20 mm/s	Tensile strength from 20.2 MPa to 89.1 MPa; Flexural strength from 14.3 MPa to 65.0 MPa; Modulus of elasticity from 2.7 GPa to 4.4 GPa
Huang et al. (2019)	ABS	Tensile and flexural strength, impact resistance	BO: horizontal; ID: 100%; LT: 0.1 mm; PS: 40 mm/s	Tensile strength from 12.0 MPa to 33.6 MPa; Flexural strength from 27.3 MPa to 64.4 MPa; Impact resistance from 4.6 kJ/m^2 to 21.5 kJ/m^2
Reddy et al. (2023)	PLA + CF	Tensile strength	ID: 100%; LT: 0.3 mm; PS: 80 mm/s	Tensile strength from 13.9 MPa to 34.2 MPa
Hanon et al. (2021)	PLA	Tensile strength	BO: horizontal; ID: 100%; RA: ±45°	Tensile strength from 33.0 MPa to 59.7 MPa
Lee & Wu (2020)	PLA + CF	Tensile strength, impact resistance	BO: 45° inclined; BT: 70 °C; ID: 60%; NT: 220 °C	Tensile strength from 28.7 MPa to 34.1 MPa Impact energy from 8.3 mJ to 14.0 mJ
Hetrick et al. (2021)	Onyx + aramid (long)	Impact energy absorption	BO: horizontal; RA: ±45°; RP: concentric	Impact energy from 2.0 J to 31.0 J
Vălean et al. (2020)	PLA	Tensile strength	BO: horizontal; ID: 100%; LT: 1.25 mm	Tensile strength from 46.8 MPa to 50.9 MPa
Rayegani & Onwubolu (2014)	ABS	Tensile strength	BO: horizontal; RA: ±45°; RG: –0.0025 mm; RW: 0.2034 mm	Tensile strength from 4.0 MPa to 38.9 MPa

End of Table 1.5

References	Materials	Tested properties	Optimal parameters	Improvement results
Sood et al. (2010)	PLA	Tensile and flexural strength, impact resistance	BO: horizontal; LT: 0.127 mm; RA: ±60°	Tensile strength from 9.1 MPa to 18.1 MPa; Flexural strength from 18.8 MPa to 39.2 MPa; Impact resistance from 343 kJ/m^2 to 482 kJ/m^2
Chohan et al. (2020)	ABS	Tensile and flexural strength, impact resistance	BO: horizontal; LT: 0.127 mm; RA: ±60°	Tensile strength 17.2 MPa; Flexural strength 16.1 MPa; Impact resistance 2.39 MJ/m^2
Blok et al. (2018)	PA + C F (long)	Tensile, shear, and flexural strength	FV: 27%; RA: 0	Tensile strength 986 MPa; Flexural strength 485 MPa; Shear strength 31.2 MPa

Note: AF = aramid fiber; CF = carbon fiber; GF = glass fiber. BO = building orientation; BT = bed temperature; ID = infill density; LT = layer thickness; NT = nozzle temperature; PS = printing speed; RA = raster angle; RG = raster gap; RP = raster pattern; RW = raster width; VF = volume of fibers.

Investigating AM accuracy and dimensional fidelity, Parker et al. (2022) demonstrated significant modifications to a commercial 3D printer, Prusa I3 MK3S, to improve the uniformity and smoothness of printed continuous carbon fiber (CCF)/polyphenylene sulfide (PPS) composites. Key upgrades included rewiring the heater coil to a temperature controller, integrating high-temperature type-K thermocouples to precisely regulate nozzle temperature, and installing a dedicated 24 V DC power supply for the temperature controller. Additionally, a cooling fan was added, and the traditional metal extruder rollers were replaced with aluminum feeder drives equipped with polyurethane (PU) rollers to reduce filament damage. Polytetrafluoroethylene (PTFE) tubing was used to introduce the fiber into the nozzle. These modifications led to notable improvements in the accuracy and stability of FFF. The tensile strength of the 50 vol% CCF/PPS composites produced using the upgraded system reached 1.9 GPa, a 37% increase over the tensile strength (1410 MPa) of composites produced with an ordinary printer.

Egorov et al. (2021) introduced a novel FFF-tailored approach for processing continuous textile flax fiber (CTFF) and Nylon 6 (PA6) composites. This method fed CTFF and PA6 filaments through two independent feeding channels; mixing and fiber impregnation were conducted in a localized, heated zone within the nozzle. The feeding mechanism incorporated a gear-like ratchet that increased friction between the filaments, reduced slippage, and improved printing precision. A vital advantage of this technique was the simultaneous impregnation and FFF process, which reduced the residence time of the continuous flax fiber in the heated nozzle, thereby reducing the risk of thermal degradation and deformation. This method significantly enhanced the uniformity and fidelity of the printed composites while improving their mechanical performance. For CTFF/PA6 composites with a continuous flax fiber volume fraction of 22 vol%, the tensile modulus and tensile strength were 5.7 GPa and 82.0 MPa. These values represented increases of 11.8% and 44% in tensile modulus and tensile strength, respectively, compared to composites produced using traditional FFF methods. This enhancement demonstrates the effectiveness of the customized printing technique in improving both the process and the material performance.

H. Li et al. (2021) developed a 3D printer to fabricate CCF/PLA composites under vacuum conditions. The findings demonstrated that the porosity of the vacuum-printed CF/PLA composites was significantly reduced to 4.1, thereby enhancing interlayer bonding. Furthermore, the specimens exhibited flexural strengths of 268.0 MPa and flexural moduli of 25.7 GPa, representing increases of 24.5% and 8.4%, respectively. Similarly, Zaldivar et al. (2017) explored the design flexibility of 3D printing by introducing pre-printed cavities in the interlayer direction of ABS parts. These cavities were subsequently filled with milled carbon fiber (MCF)/epoxy resin, and the compatibility between ABS and epoxy resin was improved by plasma treatment. The flexural strength and modulus of the 10 wt% MCF/ABS composites were 68.7 MPa and 3.1 GPa, respectively, 14.1% and 34.8% higher than those of composites without epoxy infiltration and plasma treatment. The above technological improvements highlight FFF’s effectiveness in producing higher-quality composite materials.

1.7. Biodegradable composites

Developing biodegradable polymeric composites with natural fibers for AM is increasingly essential in addressing environmental, industrial, and technological challenges (Elfaleh et al., 2023; Phiri et al., 2023). Figure 1.7 presents a multi-component view of the issue. In particular, traditional AM materials, such as synthetic polymers, often contribute to long-term environmental degradation. On the contrary, biodegradable composites minimize the persistence of waste, aligning with global efforts to reduce plastic pollution (M. Islam et al., 2024). In addition, natural fibers (e.g., jute, flax, and hemp) and biodegradable polymers (e.g., PLA and PHA, and polyhydroxyalkanoates) decompose naturally, supporting the circular economy. Manufacturing and disposal processes for biodegradable materials typically emit fewer greenhouse gases than those for petroleum-based alternatives (Rosenboom et al., 2022). Natural fibers and biodegradable polymers are derived from renewable resources, ensuring material availability without exhausting finite resources; agricultural residues provide fiber sources, turning waste into value-added materials (Hoang et al., 2024; Riseh et al., 2024).

AM is inherently efficient, producing parts with minimal waste. Combining it with biodegradable materials further enhances eco-efficiency (M. Islam et al., 2024). Moreover, natural fibers enhance the mechanical properties of polymeric composites, making them suitable for lightweight, durable structures (Khalid et al., 2021) and fostering innovation by pushing the boundaries of AM to create novel, eco-friendly materials and designs (Gribniak, 2023). The following considerations may balance performance and sustainability.

Material selection. PLA, PHA, polycaprolactone (PCL), and starch-based polymers ensure biodegradability, processability, and compatibility for FFF, SLA, and SLS (Hussain et al., 2024). The polymer's melting or glass transition temperature should be suitable for the AM process to avoid premature degradation during printing. Flax, jute, hemp, coir, sisal, or bamboo fibers may ensure sufficient mechanical performance and acceptable processing (Khalid et al., 2021). Surface treatments (e.g., alkali and silane coupling agents) enhance interfacial bonding with the polymer matrix and reduce water absorption (Mohammed et al., 2022).

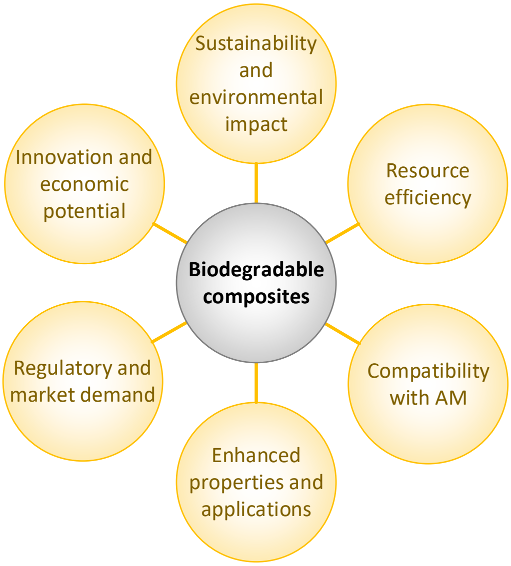

Fig. 1.7. Development challenges of the biodegradable composites for AM (Farh et al., 2026)

DfAM and sustainability metrics. New composites require optimizing printing settings, post-fabrication treatments, and material characterization, including long-term performance. The optimum fiber content (usually 10–30 wt%) balances mechanical performance with processability (Radzi et al., 2022). Excessive fiber content can clog AM nozzles and disrupt layer adhesion. Combining (hybridizing) different natural fibers or mixing natural and synthetic fibers can tailor the physical properties of biodegradable composites (Khalid et al., 2021). Eco-friendly additives and nanoparticles (e.g., cellulose nanocrystals and graphene oxide) can further increase the mechanical performance (Mokhena et al., 2024). A life cycle assessment (LCA) can quantify environmental benefits from raw material sourcing to end-of-life disposal (Ali et al., 2023) and assess biodegradation rates under standard and harsh environmental conditions to ensure the eco-friendliness of composite materials (Folino et al., 2023).

The durability *vs.* biodegradability condition describes the fundamental dilemma in developing biodegradable composites that anticipate load-bearing performance. Combining natural fibers with moisture-resistant biopolymers and coatings mitigates the hydrophilic essence of natural filaments (Kamarudin et al., 2022). Controlling processing temperatures diminishes premature fiber degradation (Ceretti et al., 2023). Optimizing AM parameters and the composite formulation address warping and shrinkage issues (Memarzadeh et al., 2023).

1.7.1. Polymeric materials

Biodegradable polymers are derived from bio-based or eco-friendly sources, offering a promising solution to the growing plastic waste crisis (Dananjaya et al., 2024). These polymers naturally decompose in the environment, making them environmentally sustainable alternatives to conventional petroleum-based polymers (Larson et al., 2013). Prominent biodegradable polymers include PHA, PLA, polybutylene succinate (PBS), polycaprolactone (PCL), polyglycolic acid (PGA), polybutylene adipate-co-terephthalate (PBAT), poly (lactic-co-glycolic acid) (PLGA), starch-based polymers, and cellulose-based polymers (Samir et al., 2022). These materials exhibit diverse and desirable properties, including high mechanical strength, favorable thermal behavior, and effective barrier performance (Tan et al., 2016). These polymers, often sourced from renewable materials such as cornstarch or sugarcane, significantly reduce dependence on fossil fuels (Post et al., 2021). By lowering carbon emissions and mitigating the environmental impacts of conventional polymeric materials, they reduce the ecological footprint through natural degradation, thereby minimizing long-term waste accumulation (Lagman-

Bautista, 2020). From a technological perspective, biodegradable polymers exhibit properties aligned with AM, including ease of processing, versatility, and the ability to achieve intricate designs with high precision (Faidallah et al., 2022). Furthermore, biodegradable polymers are widely compatible with various 3D printers, making them accessible for diverse applications.

Biodegradation is the breakdown of polymers by microorganisms and environmental factors (Bher et al., 2022). Internal factors primarily relate to the polymer's inherent chemical characteristics, including molecular weight, chemical structure, and the presence of additives or modifiers. These properties significantly affect the polymer's degradability. In contrast, external factors include environmental conditions such as temperature and humidity, as well as the presence of specific microorganisms or enzymes that metabolize the polymer (La Fuente et al., 2023). The interplay among these factors determines the rate and extent of polymer biodegradation, playing a vital role in reducing accumulated waste worldwide by facilitating the natural decomposition of materials and thereby supporting environmental sustainability. Ongoing research and development are expected to enhance the mechanical performance of these polymeric materials and expand their use as more sustainable matrices for biodegradable composites.

1.7.2. Fiber reinforcement

Extensive research has been conducted on natural fiber-reinforced polymer filaments, mainly through the FFF process. Zhao et al. (2016) developed PLA-based filaments reinforced with bamboo fibers for use in the FFF process, demonstrating improved mechanical properties, including tensile strength and modulus of elasticity. However, the increased natural fiber content also made the filaments more brittle. Kariz et al. (2016) produced FFF filaments by reinforcing PLA with wood powder, incorporating biodegradable additives and binders. Mechanical property evaluations across various filament compositions revealed that bending strength was primarily influenced by the percentages of wood powder and binder, and that strength required optimization. Girdis et al. (2017) fabricated an FFF filament by combining ABS with macadamia nutshell powder. Comparative mechanical tests showed that nutshell reinforcement outperforms wood powder reinforcement.

Pitt et al. (2017) designed FFF filaments by blending glass fiber, wood powder, and a binder. Mechanical properties, including tensile and compressive strength, were investigated and compared with those of molded components. The 3D-printed parts exhibited superior mechanical performance to their molded counterparts. Hofstätter et al. (2016) developed PLA filaments reinforced with carbon fibers. Mechanical testing, tomography, and SEM analysis were performed on the FFF components. The results indicated that tensile strength was reduced due to voids aligned with the extrusion direction. However, the fibers' longitudinal and lateral orientation contributed to an interconnected structural alignment, enhancing the mechanical performance of the printed material.

Le Duigou et al. (2016) investigated the effects of process parameters on the mechanical properties of PLA-wood fiber composites, comparing results from FFF and injection molding (IM). Experimental findings showed that print orientation (0° or 90°) and printing width (reference, doubled, or tripled) were critical parameters influencing mechanical resistance. Still, the FFF process yielded mechanical properties inferior to those of AM.

Depuydt et al. (2019) developed PLA filaments reinforced with bamboo and flax fibers for FFF applications. The results revealed that long bamboo fibers increased stiffness by more than twofold, whereas flax fibers did not. A rotational speed of 350 rpm improved filament smoothness and fiber wetting. On the other hand, Mazzanti et al. (2019) fabricated PLA filaments reinforced with short hemp fibers. The results showed that the components' tensile strength increased by 20% compared with pure PLA. However, the elastic modulus and impact energy decreased. In addition, poor interfacial bonding between fiber and matrix was observed. Franco-Urquiza et al. (2021) investigated the mechanical properties of PLA reinforced with jute fiber fabrics. The findings revealed that the tensile strength and elastic modulus increased by 10% compared to pure PLA. Still, there is a lack of systematic studies that optimize material composition and fabrication settings, underscoring the need for further research.

1.7.3. Additives and fillers

The additives and fillers include impact modifiers, flame retardants, plasticizers, and reinforcing agents, improving mechanical strength, flame resistance, thermal stability, and biodegradability (Singh et al., 2020; Wissamitanan et al., 2020). Table 1.6 (Farh et al., 2026) characterizes the biodegradable materials reported in the literature. These results demonstrate enhanced mechanical properties and promising features, ensuring a broader range of applications while maintaining the inherent environmental benefits of biodegradability. Thus, by tailoring the blend composition, manufacturers can balance biodegradability, mechanical strength, and other functional properties. This versatility ensures the creation of biodegradable materials tailored to meet specific industry requirements, including packaging, agricultural applications, and medical and electronic devices.

Table 1.6. Characterizing biodegradable materials

References	Materials	Properties		
		Mechanical	Thermal	Morphology
Gkartzou et al. (2017)	PLA + Kraft lignin (20 wt%)	A 0.5 MPa decrease in tensile strength with an increase in brittleness	Gradual increase in T_g and T_m	Poor compatibility with small lignin domains, causing local defects
Stoof et al. (2017)	PLA + Hemp and harakeke (30 wt%)	A 31% decrease in tensile strength and a 43% increase in modulus of elasticity	–	Coarse microstructure and increased porosity
Tran et al. (2017)	PCL + Micro-cocoa shell (50 wt%)	A 52% increase in modulus of elasticity	A 1.3 °C increase in T_c and a reduction of T_d	Homogeneous distribution of microfiller
C.-S. Wu et al. (2017)	PHA + Palm fiber (20 wt%)	A 43% reduction in tensile strength	–	Homogeneous fiber distribution
Q. Zhang et al. (2018)	PLA + Poplar wood powder (0…10 wt%)	A 1.5 kJ/m^3 decrease in impact and a 7 Nm increase in torsion resistance	–	Uneven PLA structure with numerous cracks and filler agglomeration
Umerah et al. (2020)	PLA + Coconut shell (1 wt%)	A 50% increase in tensile strength	Additional decomposition phase	Particle agglomeration
Scaffaro et al. (2022)	PLA + Fishbone powder (20 wt%)	A 23% increase in flexural stiffness	–	Homogeneous distribution and solid structure
Qin et al. (2022)	PLA + $CaCO_3$ (20 wt%)	A 50 MPa increase in compression strength	–	Filler clustering and local defects
Fico et al. (2022)	PLA + Ceramic waste (10 wt%)	A 2.5 GPa reduction in flexural modulus	A 5.7 °C and 13.8 °C reduction in T_g and T_m	Heterogeneous filler distribution and surface discontinuities

Note: PCL = poly(ε-caprolactone); PHA = polyhydroxyalkanoate; PLA = polylactic acid; T_c = crystallization temperature; T_d = decomposition temperature; T_g = glass transition temperature; T_m = melting temperature.

Hybrid materials add a new dimension to the biodegradable polymers. AM techniques enable the integration of biodegradable polymers with non-polymeric components such as metals or ceramics (C.-H. Kim et al., 2023). These hybrid materials combine the beneficial properties of biodegradable polymers, such as environmental sustainability, with the unique features of metals and ceramics, including electrical conductivity or thermal resistance (Kunwar et al., 2021), which offer potential for applications such as lightweight yet durable structural components, sustainable medical implants, and environmentally friendly electronic devices (Bastola et al., 2018). The promise of a sustainable future using advanced 3D-printed biodegradable materials is growing as research in this field advances.

1.8. Numerical modeling of fused filament fabrication

Despite widespread use, FFF faces notable limitations in structural applications due to mechanical issues, including residual stresses, geometric inaccuracies, and poor interlayer adhesion. These problems primarily arise from the complex thermal cycles during fabrication, during which the polymer transitions from a semi-molten to a solid state, resulting in internal stresses and distortions (Šenkeřík et al., 2024). Addressing these effects requires simulation frameworks that can model the sequential deposition and thermal evolution of the material, as demonstrated in recent finite element studies (Syrlybayev et al., 2021).

The mechanical performance of FFF components is susceptible to thermal gradients and cooling rates, which are influenced by process parameters such as nozzle temperature, printing speed, and layer thickness (S. Islam & Bagheri, 2025; F. Liu et al., 2025; Mosleh et al., 2024; Ulkir et al., 2024). Finite element (FE) simulations are a powerful tool for predicting stress distribution and deformation patterns. However, experimental optimization remains resource-intensive, underscoring the need for robust models to simulate the FFF process with high fidelity (Behseresht et al., 2024; Z. Hu & Mahadevan, 2017). A key advancement in this domain is the implementation of element activation strategies within the FE modeling framework, enabling the progressive construction of the FFF part in a virtual environment (Fianko et al., 2025). This approach captures the sequential nature of material deposition and the evolving thermal and mechanical states of the structure (Brenken et al., 2018). Early studies demonstrated the effectiveness of this method for analyzing residual stress formation in acrylonitrile butadiene styrene (ABS) components (Y. Zhang & Chou, 2006, 2008). Cattenone et al. (2019) emphasized the importance of accurate constitutive modeling for predicting distortions.

Building on these foundations, recent research has explored more advanced activation schemes to enhance the fidelity of numerical simulations in AM. For instance, studies (Khanafer et al., 2022; Syrlybayev et al., 2021) applied the element birth-and-death method proposed by (Y. Zhang & Chou, 2006) to estimate the warpage potential of FFF samples and to investigate the relationship between the FFF process settings and their impact on the fabrication quality of polymeric components. Studies (Brenken et al., 2019; Courter et al., 2017) incorporated time-dependent filament paths and thermal histories into their simulations, thereby enabling a realistic representation of the sequential deposition of material. These studies highlight the growing importance of G-code-driven simulations, where the toolpath data directly informs the activation sequence of finite elements. Typically, G-code determines a routine that transforms a numerical (computer-aided design, CAD) model into a physical object via FFF.

Further advances have been made by integrating finite element activation with process-aware control strategies. A recent study (Matúš et al., 2023) proposed a methodology that uses FE-based stress analysis to inform slicing and deposition strategies, dynamically adjusting infill density and pathway orientation based on local stress distributions. This approach not only enhances structural performance but also improves material efficiency and FFF productivity. The finite element activation technique has evolved from fundamental geometric triggers (e.g., the element centroid within a deposition path) to more sophisticated criteria that involve thermal thresholds or mechanical state variables. This progression enables better modeling of phenomena such as layer bonding, cooling-induced shrinkage, and interlayer stress accumulation, all of which are crucial for ensuring the quality of the fabricated part.

Table 1.7 (Farh & Gribniak, 2025) provides a comparative overview of recent FE modeling studies (Al Rashid & Koç, 2023; Brenken et al., 2019; G. Chen et al., 2023; Hachimi et al., 2024; Syrlybayev et al., 2021; Zhuoran Yang et al., 2025; B. Yu et al., 2025) addressing thermomechanical behavior and warpage in extrusion-based additive manufacturing. The table summarizes the simulation software used, the scope of each study, whether progressive element activation (i.e., sequential simulation of material deposition noted as "Activation") was implemented, whether the detachment of the printed part from the build platform (indicated as "Detachment") was explicitly modeled, and provides the type of outputs and experimental validation reported. Notably, while progressive activation is common, most studies simulate only the printing and cooling phases, assuming perfect adhesion to the build platform throughout. Explicit detachment modeling is critical for realistic prediction of warpage and residual-stress release, but remains rare for polymeric materials and their composites. Although recent advances in finite element modeling have improved the simulation of extrusion-based additive manufacturing, most prior studies have focused on the printing and cooling phases and have not explicitly considered the detachment stage (Table 1.7). This omission limits the ability to realistically predict warpage and the release of residual stress in polymeric materials and their composites.

Table 1.7. Comparative literature analysis related to the thermomechanical simulation of FFF

References	Software	Scope*	Activation	Detachment	Outputs and Validation
Syrlybayev et al. (2021)	ANSYS	TM	Yes	No	Warpage prediction; validated experimentally
Brenken et al. (2019)	ABAQUS	TM	Yes	Partially	Deformation, residual stress; limited large-scale validation
G. Chen et al. (2023)	ANSYS	TM	Yes	No	Warpage/distortion simulation; validated experimentally
Al Rashid & Koç (2023)	Digimat	TM	Yes	No (perfect bond)	Warpage/deflection (infill effects); test validation
Hachimi et al. (2024)	ABAQUS	M	No (test stage)	No	Tensile behavior across raster angles; no warpage validation
Zhuoran Yang et al. (2025)	ANSYS	TM	Yes (birth-death)	No	Warpage prediction; numerical validation
B. Yu et al. (2025)	ANSYS	TM	Yes (birth-death)	No	Warpage/mechanical properties; validated experimentally

* TM = thermomechanical; M = mechanical testing; TME = thermomechanical extended (printing→cooling→detachment).

1.9. Conclusions of the First Chapter and formulation of the dissertation tasks

The literature confirms the feasibility of FRP development by FFF but also reveals unresolved couplings among material selection, reinforcement architecture, and process-induced fields that continue to limit dimensional fidelity and structural reliability. The following gaps motivate this dissertation:

1. The recycling problem is typically studied via repeated reprocessing of the same PLA. In contrast, industrial practice uses partial substitution of virgin PLA with recycled polymer, leaving the true effect on printed-specimen performance insufficiently established.
2. Continuous reinforcement on ordinary single-extruder printers lacks in-process fiber tensioning and exhibits geometry-control constraints, so

the mechanical efficiency relative to theoretical potential remains uncertain and methodology-dependent.

3. For short-fiber composites, the field still lacks an integrated, FFF-specific understanding of how fiber material, geometry, and content affect crystallinity, viscoelastic stability, interfacial integrity, and resulting dimensional fidelity (warpage) under consistent printing conditions.
4. Process modeling studies often omit explicit detachment and do not transfer process-induced residual stresses and geometric distortion fields into subsequent tensile analyses; this limits scientific interpretation of how thermal history and constraint release shape the as-printed mechanical response.

Building on the literature review, the dissertation aims to develop an experimental-computational methodology to assess the mechanical efficiency of reinforced PLA composites and to predict FFF-induced geometric distortion and residual-stress evolution. To achieve this aim, the dissertation integrates literature analysis, physical experiments, material characterization, and finite-element simulations to develop a unified approach to investigate how material composition, reinforcement architecture, and process-induced fields influence the structural response of PLA-based FFF components. In this context, the following fundamental issues should be solved:

1. To evaluate the mechanical performance of PLA-based FFF components by assessing how reinforcement type (continuous and short fibers) and material composition, including virgin PLA, PLA with 40% recycled content, and fiber-reinforced variants, affect load-bearing capacity, stiffness, and failure behavior under standardized testing conditions.
2. To establish the relationships among fabrication process, microstructure, and thermo-physical response by examining crystallinity, viscoelastic behavior, thermal stability, and microstructural features of neat and fiber-reinforced PLA using DSC, DMA, and SEM, and by identifying the dominant failure mechanisms through tensile and flexural testing combined with microstructural evidence of fiber dispersion, interface quality, void formation, and fracture morphology.
3. To develop and experimentally validate a coupled thermo-mechanical modeling framework capable of predicting residual stresses, geometric distortions, and warpage mitigation by integrating toolpath-driven element activation, temperature-dependent material behavior, and mean-field homogenization for short-fiber composites across the printing, cooling, and detachment stages of the FFF process.

2

Materials, Methods, and Research Methodology

This chapter examines two interrelated aspects of FFF of PLA-based components: improving mechanical performance, particularly tensile load-bearing capacity, and enhancing fabrication quality, including dimensional accuracy, process stability, and defect sensitivity. The short-term mechanical performance of polymeric materials can be classified into static and dynamic. This research focuses on the load-bearing capacity and the viscoelastic behavior of PLA-based FFF materials. The experimental program combines static mechanical testing with dynamic thermomechanical characterization. The static performance was evaluated using uniaxial tensile and three-point bending tests, typical of FFF polymers.

Continuous-fiber reinforcement is investigated as a primary strategy to increase strength, using tensile testing and numerical analysis to compare reinforced and unreinforced PLA (including recycled PLA), evaluate practical gains, and identify process-related limitations. In parallel, short-fiber-filled PLA materials, such as carbon and wood-fiber filaments, are studied for their ability to improve ductility, toughness, energy absorption, thermal stability, and manufacturing quality, while also reducing warpage and enhancing dimensional fidelity. The chapter integrates these investigations into a framework that balances structural performance and printability, supports sustainable composite development, and introduces thermo-mechanical process simulation to predict warpage, residual stresses, and deviations between ideal and as-printed mechanical behavior. The research findings of this chapter are presented in the scientific publications (Rimkus et al., 2022; Farh et al., 2024; Farh & Gribniak, 2025).

2.1. Structure of the research program

This chapter is structured around two central aspects of the FFF process of PLA-based components: enhancement of mechanical performance, specifically tensile load-bearing capacity, and fabrication quality, including dimensional fidelity, process stability, and defect sensitivity. These aspects are treated as interdependent rather than independent design objectives, since reinforcement strategies that improve strength may simultaneously introduce manufacturing constraints. At the same time, materials that enhance printability may alter mechanical response.

To address the first aspect, continuous-fiber reinforcement is employed as a direct strategy to increase tensile strength and load-bearing efficiency. The work first establishes a consistent tensile-testing basis for comparing reinforced and unreinforced specimens of identical geometry, then quantifies the baseline tensile response of unreinforced PLA, including recycled-content PLA, to provide a sustainability-oriented reference. The reinforced specimens are subsequently tested in tension to determine the practical gain in load-bearing capacity and to identify the dominant limitations governing reinforcement utilization, including filament-level imperfections introduced during reinforcement and printing, as well as interface-controlled failure mechanisms that limit gains in stiffness and strength. In parallel, numerical interpretation is used to assess the efficiency of reinforcement relative to idealized expectations, highlighting the roles of process-induced variability and geometric effects in reducing the fraction of theoretical reinforcement potential that can be achieved. This approach is intended to quantify the achievable improvement in structural performance and to identify process-dependent limitations, such as printing quality, filament stability, and toolpath continuity, that govern the utilization of reinforcement.

The second aspect focuses on improving fabrication quality using short-fiber-filled PLA filaments, such as carbon fiber (PLA-CF) and wood fiber (PLA-WF). Unlike continuous reinforcement, short fibers remain compatible with standard slicing strategies and complex geometries, offering greater reliability in practical manufacturing and achieving the desired printing quality. Their role in this study is to enhance deformation capacity, ductility, energy absorption, and crack resistance of printed components, and to investigate how fiber type and dispersion influence manufacturing outcomes, including dimensional fidelity, interlayer bonding, and defect formation. Besides improving ductility, toughness, and thermal resistance, short fibers enhance manufacturing quality by reducing shrinkage-induced deformation and process variability. In particular, this study assumes that short fibers can mitigate warpage during cooling by constraining thermal contraction and modifying the thermo-mechanical response of the printed structure.

This chapter is organized into three complementary investigative tracks. The first examines continuous-fiber reinforcement as a strategy for maximizing tensile strength and structural efficiency. The second evaluates short-fiber-filled PLA systems, such as carbon and wood-filled filaments, to evaluate their role in improving toughness, ductility, thermal stability, and manufacturing reliability, as well as their influence on dimensional accuracy and warpage behavior. Together, these tracks establish a framework for balancing mechanical performance and fabrication quality in FFF-printed PLA composites, while also supporting the development of sustainable, high-performance material solutions for functional additive manufacturing applications. Finally, these experimental outcomes motivate the adoption of a systematic process-simulation approach: thermo-mechanical modeling is implemented to predict FFF-induced warpage in neat PLA. It is extended to FRP composite filaments via homogenized composite modeling. At the same time, the resulting residual stress fields and geometric distortion are used to explain deviations between the idealized and as-printed mechanical responses.

2.2. Materials and preparation of test specimens

The First Chapter highlighted a broad range of PLA applications in FFF research. Regarding alternative polymers available on the market, the low thermal shrinkage, biodegradability, low-temperature printability, and recyclability supported the selection of PLA for this study. The choice of continuous aramid filament reinforces the PLA matrix to prevent the polymeric composite’s brittle failure because of the aramid toughness and high strain at the peak load compared to the carbon and glass fibers. The selection of short-fiber composite PLA filaments was motivated by their ability to enhance both the mechanical response and manufacturing reliability of FFF components while remaining compatible with conventional printing processes. CF-PLA was selected for its ability to enhance stiffness, thermal stability, and dimensional accuracy by reducing thermal deformation during cooling. In contrast, wood-fiber-filled PLA was selected as a bio-based alternative that can improve ductility and toughness while supporting the development of sustainable composite materials. Additionally, the presence of short fibers can reduce shrinkage-induced warpage and improve the dimensional fidelity of printed components, making these materials suitable for investigating the relationship among material composition, printability, and fabrication quality in FFF processes.

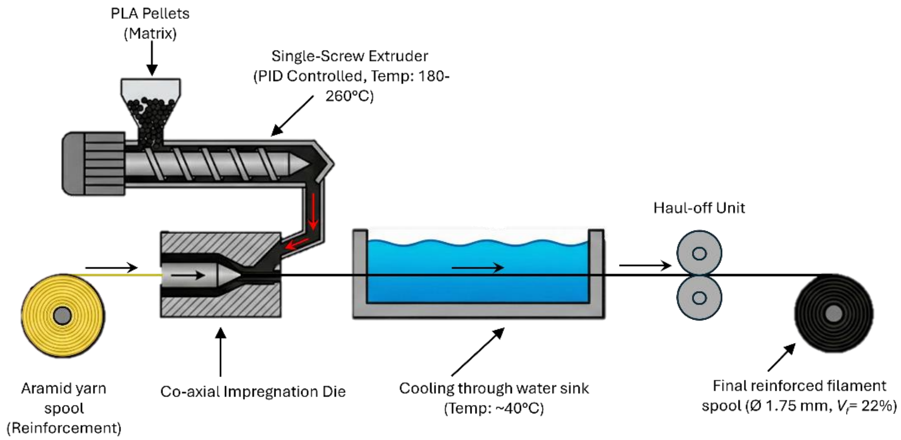

Fig. 2.1. Schematic representation of the continuous filament manufacturing process

2.2.1. Production of continuously reinforced polymer filament

The reinforcement phase (Fig. 2.1) used high-performance Twaron 1610 Dtex para-aramid yarn (0.38 mm diameter, 1K yarn; Teijin Aramid, The Netherlands) to produce the reinforced PLA filaments. The producer provided the following characteristics of the aramid fiber: a 1.44–1.45 g/cm³ density; the 2.7–3.6 GPa tensile strength; the 60–145 GPa modulus of elasticity. Initially, the fiber bundle was coaxially distributed within the PLA matrix using a modified single-screw extrusion line (Nanjing Tengda Machinery, China). The fabrication process was controlled by Pixsys ATR142 PID controllers, which maintained a temperature gradient profile that peaked at 260 °C in the impregnation zone to facilitate polymer melt flow and fiber wetting. Then, it stabilized the subsequent extrusion zones at 180–195 °C. In the post-extrusion phase, the composite filament was passed through an HMI-monitored water bath maintained at approximately 40 °C to rapidly solidify the polymer matrix. The cooled filament was drawn by a haul-off unit operating at 8.0 RPM to achieve a calibrated outer diameter of 1.75 mm. The final continuous aramid-reinforced PLA filament, with a fiber volumetric fraction (V_f) of 22%, was spooled and prepared for additive manufacturing as a feedstock for conventional FFF desktop printers.

2.2.2. Filament characteristics

The study adopted seven different filament types: continuously reinforced PLA with the 22 vol% volumetric fiber content, 40% recycled-content PLA, and neat PLA (Inorega Ltd., Lithuania), PLA (Prusa, Czech Republic), in addition to three commercially available filaments supplied by Porima3D (Turkiye): Porima PLA

(RAL9003), Porima PLA reinforced with carbon fibers (PLA-CF), and Porima PLA reinforced with wood fibers (PLA-WF).

The PLA filament, produced by Prusa, had a nominal diameter of 1.75 ± 0.02 mm, as specified by the manufacturer. According to the manufacturer's technical datasheet, the allowable fabrication parameters include a nozzle temperature of 210 ± 10 °C, a heated bed temperature of 40–60 °C, and a print speed of up to 200 mm/s. A cooling fan speed of 100% is advised to ensure optimal print quality. PLA filament exhibits a tensile strength of 51 MPa, an elastic modulus of 2.3 GPa, and a density of 1.24 g/cm^3. All filaments had a nominal diameter of 1.75 mm and were supplied on 1 kg spools. According to the manufacturer's specifications, Porima3D, the neat PLA filament exhibits a tensile strength of 56 MPa, an elastic modulus of 2.8 GPa, and a density of 1.24 g/cm^3, while the PLA-CF filament possesses a tensile strength of 65 MPa, an elastic modulus of 4.0 GPa, and a density of 1.27 g/cm^3. The PLA-WF filament has a tensile strength of 35 MPa, an elastic modulus of 1.8 GPa, and a density of 1.20 g/cm^3. The PLA-WF filament contains approximately 30 wt% wood filler, whereas the PLA-CF filament contains 10 wt% short carbon fibers. The tensile, elastic, and density values reported above were provided by the manufacturer using molded specimens.

The printing parameters and experimental conditions were selected to ensure reproducible manufacturing using standard FFF equipment and to maintain comparability between reinforced and unreinforced materials. The parameters were chosen based on manufacturer recommendations for PLA-based filaments and prior studies on FFF processing to ensure stable extrusion, proper interlayer bonding, and minimal process-induced defects. Table 2.1 summarizes the experimental design for test specimens across the adopted materials.

Table 2.1. Fabrication specifications for the tested materials

Filament	Geometry standard	Print speed	Temperature		Infill density	Raster angle	Nozzle	Samples
			Extrusion	Build platform				
		(mm/s)	(°C)	(°C)	(%)	(°)	(mm)	(-)
1	2	3	4	5	6	7	8	9
cAFR-PLA V_f = 22 vol.% (In.LT)	ASTM D3039	10	210	60	100	±45	0.8	5
40% recycled-PLA (In.LT)	ASTM D638-14	28	210	60	100	±45	0.4	6

End of Table 2.1

1	2	3	4	5	6	7	8	9
PLA (In.LT)	ASTM D638-14, ASTM D3039	28	210	60	100	±45	0.4	11
PLA (Pr.CZ)	ASTM D638-14	28	210	60	100	±45	0.4	6
PLA (Po.TR)	ASTM D638-14, ASTM D790	30	215	60	20, 60, 100	±45	0.4	6, 6, 6
PLA-CF 10 wt% (Po.TR)	ASTM D638-14, ASTM D790	30	215	60	20, 60, 100	±45	0.4	6, 6, 6
PLA-WF 30 wt% (Po.TR)	ASTM D638-14, ASTM D790	30	215	60	20, 60, 100	±45	0.4	6, 6, 6

Note: cAFR-PLA is continuous aramid-fiber reinforced PLA, (In.LT), (Pr.CZ), and (Po.TR) represent (Inorega Ltd., Lithuania), (Prusa, Czech Republic), and (Porima3D, Turkiye).

2.3. Experimental testing procedures

The experimental program of continuously reinforced thermoplastics consists of two stages. The first stage investigates the mechanical properties of alternative PLA materials and verifies the feasibility of partially replacing the source material with recycled plastic. At the second stage, the mechanical performance of FFF components produced from the partially recycled PLA reinforced with continuous aramid fiber is analyzed. The test campaign included 28 tensile test specimens: 18 were tested in the first stage without reinforcement, and the remaining 10 reinforced polymeric samples were tested in the second stage. All specimens were produced on a Prusa i3 MK3 printer using PrusaSlicer 2.3.3.

The existing FFF hardware and slicing limits necessitate straight, uninterrupted deposition paths to maintain fiber integrity for the adopted pre-impregnated continuously reinforced filament. By matching the testing protocol to these longitudinal printing paths, the characterization captures the composite's effective mechanical potential while eliminating variables associated with fiber curvature and discontinuities. Therefore, uniaxial tensile testing is scientifically justified by the alignment of the loading state with the material's principal reinforcement axis and by practical constraints associated with the adopted reinforcement approach, thereby ensuring a direct measurement of reinforcement efficiency.

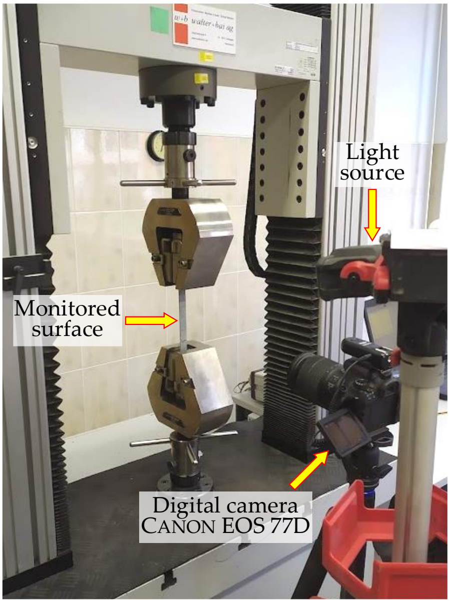

Fig. 2.2. Tensile test setup

The tensile tests were performed using a 100 kN electromechanical testing apparatus (H100KS, Tinius Olsen, Norway) at a loading rate of 2 mm/min. A 100 kN load cell measured the load. Figure 2.2 shows the testing setup. A digital image correlation (DIC) system monitored the relative displacements of the specimen surface (Fig. 2.2). The GOM Correlate software determined the strain distribution maps. The spray paint ensured a high-contrast, random pattern to facilitate the software's tracking of the movement tensors of the pixels recognized in the surface's digital images. This technique enables monitoring the relative displacements of arbitrarily selected pixels after physical tests (Gribniak et al., 2021a, 2021c). A digital single-lens reflex camera, Canon EOS 77D SLR, with an 18-135 mm Canon EF-S lens placed on a tripod at 0.4 m from the monitored surface, captured the digital images, using the following settings: exposure time = 1/100 s, aperture = f/4.0, sensitivity to light = ISO 100, focal length = 24 mm. The 6000×4000 px images were captured at 0.25 kN increments. A remote-control device allowed the camera to avoid unexpected movements.

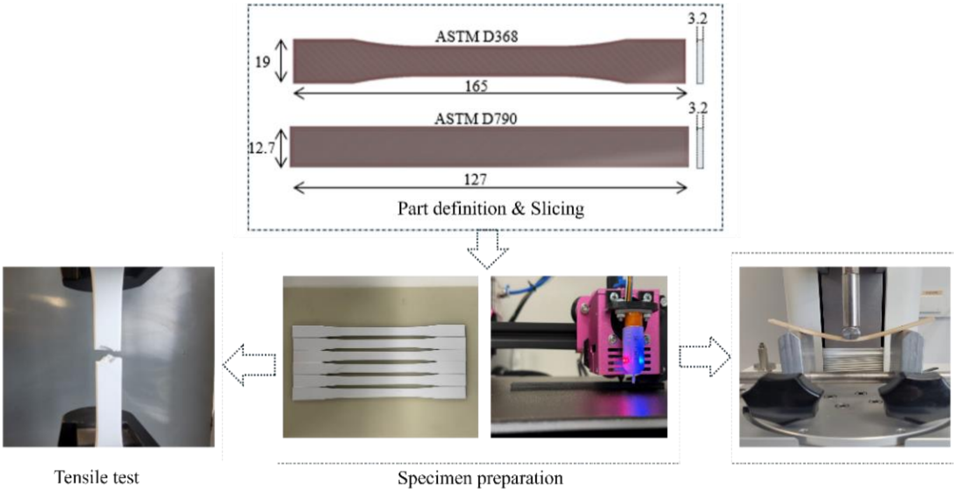

Fig. 2.3. Experimental program workflow

For short-fiber reinforced thermoplastics, the experimental program (Fig. 2.3) comprised: fabrication of additively manufactured specimens using FFF; mechanical characterization under uniaxial tensile and three-point bending; thermo-physical and viscoelastic characterization by differential scanning calorimetry (DSC) and dynamic mechanical analysis (DMA); and microstructural investigation of fracture surfaces using scanning electron microscopy (SEM). All test specimens were fabricated using a BIQU B1 FFF 3D printer with a 0.4 mm nozzle, and the slicing was performed with PrusaSlicer v2.6.1.

2.3.1. Tensile test of recycled polymer

The first testing stage uses tensile specimens from three different PLA materials. Peinado et al. (2015) and Anderson (2017) reported that reusing a PLA that has been recycled multiple times (up to 20) through the FFF process minimally affects the mechanical performance of the printed material. They also did not find a significant alteration of the mechanical properties. These results led the author to hypothesize that there is no adverse effect of using recycled polymers in FFF. Therefore, the locally produced partly recycled PLA (Inorega Ltd., Lithuania) is the object of investigation to verify the above hypothesis. This material contains 40% recycled PLA purchased from the local recycling company. Therefore, no details about the recycling rate are available. The 100% primary PLA from the same producer serves as the reference; the comparative analysis also includes a reputable European PLA manufacturer (Prusa, Czech Republic). Filament materials with a nominal diameter of 1.75 mm were used for FFF.

The unreinforced tensile specimens correspond to Type I according to ASTM D638-14 (ASTM International, 2014a). The printing layout of the dumbbell-shaped test samples (Fig. 2.4a) includes two solid “shells” at the perimeter; the inner part of the specimen was printed in 11 layers with 100% infill, oriented at 45° to the loading direction. The infill angle was altered for every layer. The 3D printing was carried out using a 0.4 mm nozzle at 210 °C and 28 mm/s, with a bed temperature of 60 °C. Six specimens of each material were manufactured using the parameters described above.

The 18 unreinforced samples were tested to compare the mechanical performance of the printed materials. Figure 3.2 shows the stress-strain diagrams and the characteristic failure mechanisms (the actual cross-section dimensions determined the stresses in the polymer).

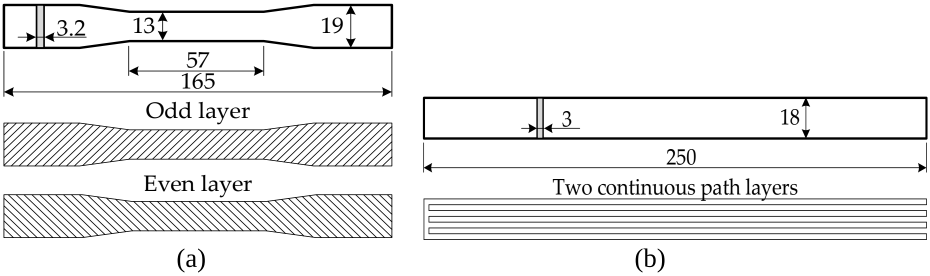

(a) (b)

Fig. 2.4. Sample dimensions (in mm) and printing layout: (a) unreinforced specimen; (b) reinforced plate

2.3.2. Tensile tests of continuously reinforced polymer

The FFF process uses a conventional Prusa i3 MK3 printer with a 0.8 mm nozzle. The specimens were manufactured at 210 °C and a speed of 10 mm/s; the bed temperature was 60°C. The reinforced samples for the tensile tests (Fig. 2.4b) consist of a 250 × 18 × 3 mm square plate, in accordance with ASTM D3039 (ASTM International, 2017). Continuous reinforcement prevents the printing process from being terminated. Therefore, the 3D extruder motion and printing flow were tailored to avoid interrupting or damaging the pathway. The printing code was customized to specify a constant volumetric flow rate of 26 mm^3/s for the fibrous PLA composite. Figure 2.4b shows the extruder’s travel path. Five PLA specimens reinforced with aramid fiber were manufactured using the parameters above. For comparison purposes, five additional samples of the same geometry (i.e., the 250 × 18 × 3 mm square plate) were produced without reinforcement.

2.3.3. Reinforcement efficiency evaluation

Gribniak et al. (2021a, 2021b) developed a methodology for estimating the reinforcement efficiency. It employs a simplified finite element model based on the smeared reinforcement concept. The model's ability to predict the composite's actual mechanical resistance (stiffness and load-bearing capacity) under the assumption of experimental elastic moduli for the composite constituents (PLA matrix and bare fiber) quantifies the reinforcement efficiency. Following this concept, the tensile (Fig. 2.2) expressed in terms of external load P induces two internal forces acting on the aramid fiber N_f and PLA matrix N_p:

$$\mathrm{P} = \mathrm{N}_f + \mathrm{N}_p. \tag{2.1}$$

The following equation explains the above load components by the average strains ε, assuming equality of the considered deformations:

$$\left.\begin{array}{r} E_m A_m \varepsilon_m = E_f A_f \varepsilon_f + E_p A_p \varepsilon_p \\ \varepsilon_m = \varepsilon_f = \varepsilon_p \end{array}\right\} \Longrightarrow E_m A_m = E_f A_f + E_p A_p, \tag{2.2}$$

where E and A are the elastic modulus and area; the indices m, f, and p correspond to the composite, aramid fiber, and PLA matrix parameters. The following formulas express the areas in Eq. 2.2 in the volumetric fiber fraction V_f terms:

$$A_f = A_m \cdot V_f; \quad A_p = A_m \cdot \left(1 - V_f\right). \tag{2.3}$$

The above expression allows simplifying Eq. 2.2 as follows:

$$E_m = E_f \cdot V_f + E_p \cdot \left(1 - V_f\right). \tag{2.4}$$

The elastic modulus E_{test} determined through the reinforcement specimen tensile tests (Fig. 3.1) describes the efficient reinforcement fraction, $V_{f,ef}$, as follows:

$$V_{f,ef} = \frac{E_{test} - E_p}{E_f - E_p}. \tag{2.5}$$

The following coefficient describes fiber reinforcement efficiency:

$$C_{ef} = \frac{V_{f,ef}}{V_f} \times 100\%. \tag{2.6}$$

2.3.4. Tensile and flexural testing of short-fiber reinforced composites

Mechanical testing was conducted to evaluate the tensile and flexural properties of the FFF specimens. Standardized test methods defined by ASTM International were adopted to ensure repeatability and comparability of the measured mechanical properties. Tensile specimens were fabricated in accordance with ASTM D638 Type I geometry. The dumbbell-shaped samples were printed with two solid outer shells at the perimeter. At the same time, the internal region consisted of 11 layers printed with a ±45° raster orientation relative to the loading direction. The infill angle was alternated between successive layers to enhance structural isotropy. Three infill densities (20%, 60%, and 100%) were investigated to assess the influence of internal structure on tensile performance, with six specimens fabricated for each material and infill density. All specimens were printed using a 0.4 mm nozzle at 215 °C, a bed temperature of 60 °C, and a constant print speed of 30 mm/s.

Uniaxial tensile tests were performed using an electromechanical universal testing machine manufactured by Jinan Testing Equipment IE Corporation, equipped with a 100 kN load cell suitable for polymer-based specimens. Testing was conducted under displacement control in accordance with ASTM D638, with a constant crosshead speed of 5 mm/min. All experiments were carried out under laboratory conditions at 23 °C. Force-displacement data and engineering stress-strain curves were recorded. The ultimate tensile strength σ_u was calculated as follows:

$$\sigma_u = \frac{P_u}{A}. \tag{2.7}$$

where P_u is the ultimate tensile load (N), and A is the cross-sectional area (mm^2).

The elastic modulus E was determined from the slope of the linear elastic region of the stress-strain curve as follows:

$$E = \frac{\Delta\sigma}{\Delta\varepsilon}. \tag{2.8}$$

In FFF samples, the initial portion of the force-displacement or stress-strain curve is typically nonlinear (Rimkus et al., 2022). This behavior arises from several microstructural (fabrication-induced) and testing-related factors. However, after the initial adjustment stage, the response enters a quasi-linear elastic region in which stress and strain are approximately linearly related. Therefore, this study determines the elastic modulus using Eq. (2.8) as the slope of the linear fit within the quasi-linear elastic segment of the stress-strain diagram, excluding the initial nonlinear portion associated with seating and microstructural accommodation in the FFF material. This approach is consistent with standard mechanical characterization practices for polymeric materials, e.g., ISO 527 (ISO, 2019).

Flexural specimens were printed as rectangular beams in accordance with ASTM D790 (ASTM International, 2010b), with five specimens per material, and 100% infill density. The infill raster orientation was set to ±45° and alternated between layers, consistent with the strategy used for tensile specimens. Printing parameters, including nozzle diameter, temperatures, and print speed, were identical to those used for tensile sample fabrication. Three-point bending tests were conducted following ASTM D790 using a TX-700 Texture Analyzer. The specimens were tested with a support span length of 51.2 mm and a constant crosshead speed of 1.30 mm/min. Force-displacement data were recorded until specimen failure. The flexural stress and flexural modulus of elasticity were calculated using the following equations:

$$\sigma_f = \frac{3PL}{2bd^2}; \tag{2.9}$$

$$E_f = \frac{\sigma_f}{\varepsilon_f} = \frac{L^2 m}{4bd^3}, \tag{2.10}$$

where σ_f is the flexural stress (MPa), P is the applied load at a given point on the load-deflection curve (N), L is the support span length (mm), b is the specimen width (mm), d is the specimen thickness (mm); L is the support span length (mm), m is the slope of the load-deflection curve, ε_f is the flexural strain.

2.4. Thermal characterization by differential scanning calorimetry

The thermal behavior of the investigated filament materials was characterized via differential scanning calorimetry (DSC) using a Linseis DSC-PT10 (Linseis Messgerate GmbH, Germany), including the glass transition temperature (T_g), cold crystallization temperature (T_{cc}), melting temperature (T_m), and the associated enthalpy changes. DSC measurements were carried out using a laboratory differential scanning calorimeter. Specimens with a mass of approximately 7 ± 1 mg were sealed in hermetically crimped aluminum pans and analyzed under a nitrogen purge atmosphere at a flow rate of 50 mL/min to minimize oxidative degradation during heating.

The analysis was performed using a heat-cool-heat temperature program. The first heating scan was conducted to eliminate the samples' prior thermal history, followed by a controlled cooling scan and a second heating scan to evaluate the materials' inherent thermal transitions. All heating and cooling scans were performed at a constant rate of 10 °C/min from 25 °C to 200 °C.

Thermal transition temperatures (T_g, T_{cc}, and T_m) and the enthalpy values for cold crystallization (ΔH_{cc}) and melting (ΔH_m) were determined from the DSC thermograms using the instrument's analysis software. The degree of crystallinity (X_c) was calculated from the second heating scan using the following equation (Kong & Hay, 2002):

$$X_c(\%) = \frac{\Delta H_m - \Delta H_{cc}}{\Delta H_m^0 \, . w} \times 100, \tag{2.11}$$

where ΔH_m is the measured melting enthalpy, ΔH_{cc} is the cold crystallization enthalpy, and ΔH_m° is the melting enthalpy of a fully crystalline polymer, and w is the mass fraction of the polymer matrix.

2.5. Viscoelastic characterization by dynamic mechanical analysis

Dynamic mechanical analysis (DMA) was performed to characterize the viscoelastic response and temperature-dependent stiffness of the printed materials. DMA testing was carried out using a laboratory dynamic mechanical analyzer (TA Instruments Q800). Measurements were conducted in three-point bending using rectangular specimens machined from printed bars (typical dimensions ≈ 35 × 10 × 3 mm). A periodic deformation was applied at 1 Hz with a small oscillation amplitude (10 μm) to maintain linear viscoelastic conditions. The temperature was increased at a constant rate of 3 °C/min from 25 to 120 °C. The storage modulus (E'), loss modulus (E''), and damping factor (tan δ) were recorded; the DMA-derived transition temperature was defined as the tan δ peak.

2.6. Scanning electron microscopy analysis of short-fiber reinforced polymer

The SEM analysis was employed to examine the microstructural features of the investigated materials and to assess fiber dispersion, interfacial characteristics, and fracture morphology. SEM observations were performed using a field-emission scanning electron microscope (FEI Quanta 450 FEG, Thermo Fisher Scientific, USA). Due to the dielectric nature of the PLA matrix and the organic wood fillers, the specimens were first coated using a VTC-P100 Plasma Vacuum Coater (OptoSense, Turkey). A conductive nanometric layer was deposited under high vacuum (14 Pa) to minimize surface charging, ensure stable electron emission, and improve imaging quality at higher magnifications. Cross-sections of the as-received filaments (PLA, PLA-CF, and PLA-WF) were analyzed to quantify the internal morphology and to confirm the presence and distribution of short reinforcing fibers within the polymer matrix.

SEM was also used to examine the fracture surfaces of additively manufactured specimens subjected to mechanical testing to identify dominant failure mechanisms and damage features generated during loading. Imaging was carried out at an accelerating voltage suitable for polymer-based composites, using secondary-electron mode to resolve surface topography and fiber-matrix interactions.

2.7. Warpage

During fabrication of test specimens, warpage was observed, manifested as out-of-plane bending and edge lifting of the printed parts during cooling. This behavior is characteristic of semi-crystalline thermoplastics such as PLA, where non-uniform heat dissipation through the build thickness generates thermal gradients and differential shrinkage between the upper layers and the region constrained by the heated bed. The accumulated residual stresses can exceed the adhesion forces at the bed-part interface or the interlayer constraint, leading to geometric distortion and, in severe cases, partial detachment. In this study, warpage was quantified by measuring the maximum out-of-plane edge deflection of the printed specimens after cooling and removal from the build platform. The printed samples were placed on a flat reference surface, and the vertical displacement of the lifted edges relative to this surface was measured. The measurements were performed using a Vernier caliper with an accuracy of 0.02 mm. The warpage magnitude was determined as the maximum edge lift (out-of-plane displacement) observed along the specimen’s edges.

Compared to neat PLA, the short-fiber composites exhibited reduced edge warpage: the addition of 10 wt% CF contributed to a reduction in edge warpage of 14.3%, whereas 30 wt% WF reduced edge warpage by 43% (Fig. 2.5). These reductions are consistent with increased geometric fidelity during cooling, reflected by flatter specimens and lower out-of-plane deflection after printing, which is important to consider where tighter control over dimensions is desired. The reduction in warpage is attributed to the presence of rigid short fibers, which increase the effective stiffness of the extruded paths, constrain matrix shrinkage, and reduce thermal contraction by lowering the volume fraction of the shrinking polymer phase. In addition, fiber-induced microstructural constraints and the higher crystalline fraction observed in the wood-fiber composite help stabilize the geometry during cooling by limiting long-range chain relaxation. Short-fiber reinforcement provides a practical advantage in FFF by mitigating distortion driven by residual stress and improving the dimensional fidelity of tensile specimens.

The observed reduction in edge warpage in short-fiber-reinforced composites indicates that fibers can enhance dimensional fidelity, making them useful for applications that require geometric precision. Further progress is expected from improving fiber-matrix compatibility and reducing defect sensitivity (e.g., fiber surface treatment/coupling agents, improved melt impregnation during filament extrusion, and printing strategies that enhance consolidation and alignment with load paths). Future research should emphasize predictive numerical modeling to estimate temperature fields, residual stress development, and part distortion during printing and cooling, thereby enabling geometry compensation and process optimization. Such predictive model-based approaches can reduce reliance on extensive trial-and-error, thereby minimizing time and material waste associated with unsuccessful print attempts. In practice, warpage is not only a dimensional-accuracy issue: it can also trigger printing errors, edge lifting, and local loss of interlayer contact. Therefore, predicting part distortion in advance is essential for selecting process settings and materials that maintain geometric fidelity throughout cooling and part detachment. The next section presents a coupled thermo-mechanical finite element approach for predicting warpage in FFF plastics, based on the simulated thermal history and the resulting evolution of residual stresses.

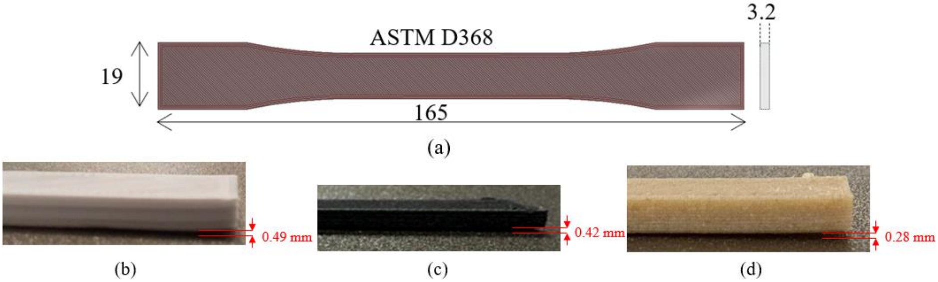

Fig. 2.5. Edge warpage measurements where (a) typical schematic of printed test specimen (dimensions in mm); (b) neat PLA; (c) PLA-CF; and (d) PLA-WF edge warpage

2.8. Thermo-mechanical approach of the fused filament fabrication process

This study presents a numerical simulation of the FFF process, which was performed using two complementary finite-element environments: ABAQUS and Hexagon Digimat. The 3D staged thermo-mechanical framework is described and was implemented in ABAQUS AM modeler for neat PLA, enabling explicit resolution of the sequential manufacturing stages (printing, cooling, and detachment) and their influence on residual-stress development and warpage.

For the short-fiber composite filaments (PLA-CF and PLA-WF), Digimat was adopted because it provides a practical workflow for modeling fiber-reinforced polymer materials and direct coupling with Digimat-AM for process-level distortion prediction. For composite material modeling, the most suitable choice is Digimat-MF, as it is specifically designed for the mean-field homogenization of representative volume element (RVE) models for short-fiber composites and efficiently delivers the effective, generally anisotropic thermo-mechanical properties required by process simulations. In this approach, an RVE representation of the microstructure (fiber content, morphology, and orientation state) is defined, and the homogenization procedure computes the equivalent macroscopic constitutive response. Accordingly, Digimat-MF provides the most direct and computationally efficient route for generating a composite material card suitable for subsequent warpage simulation in Digimat-AM.

This research builds upon the above findings, namely, that FFF-fabricated PLA specimens can develop edge warpage and out-of-plane distortion during cooling, which affects dimensional fidelity and may influence the mechanical response, in addition to the findings of a prior program (Šostakaitė et al., 2024) that investigated additive drone manufacturing using a desktop 3D printer and commercially available polymeric materials. The comparative analysis presented by Šostakaitė et al. (2024) outlines key material properties, including tensile strength, modulus of elasticity, and thermal characteristics. These insights, together with PLA’s compatibility with desktop FFF printers, justify its selection for this study, given its non-toxicity, ease of processing, and affordability. Additionally, recent studies have reinforced the appropriateness of PLA-based materials for drones, highlighting their favorable strength-to-weight ratio, ease of printing, and suitability for complex geometries (Kantaros et al., 2025; Plamadiala et al., 2025).

2.8.1. Specimen design and fabrication parameters

The experimental phase employed tensile specimens conforming to the ASTM D638-14 (ASTM International, 2014a) geometry. The test specimens were produced using a Prusa i3 MK3 printer and sliced with PrusaSlicer 2.3.3 (Prusa Research, Prague, Czech Republic), which offers the resolution and control required for research-grade FFF.

Figure 2.6 shows the research workflow. The slicing parameters were selected to ensure complete material deposition and minimize interlayer defects, based on studies by Šenkeřík et al. (2024) and Mosleh et al. (2024). The test phase was designed in direct response to the fabrication challenges identified in the preceding research, particularly inadequate adhesion and warpage during FFF. Building on these findings, the present work applies a detailed staged thermo-mechanical simulation framework to systematically investigate the thermal and mechanical evolution of printed parts under constrained geometries and weight-sensitive applications. The previous tests (Rimkus et al., 2022; Farh et al., 2024; Šostakaitė et al., 2024) defined the specific printing settings to ensure the sample's warpage during physical testing. To induce warpage, the specimens were printed on a replacement spring steel sheet coated with smooth, double-sided PEI (polyethylenimine), and no additional adhesion measures were used. The physical experiment was conducted in an open-chamber environment to simulate the printing conditions. After fabrication and cooling under laboratory conditions (at 20 °C) until the printing bed temperature reached 25 °C, the test samples were removed by bending (flexing) the spring steel sheet to mechanically detach the specimen, after which the specimen edge debonded due to the cooling-induced release.

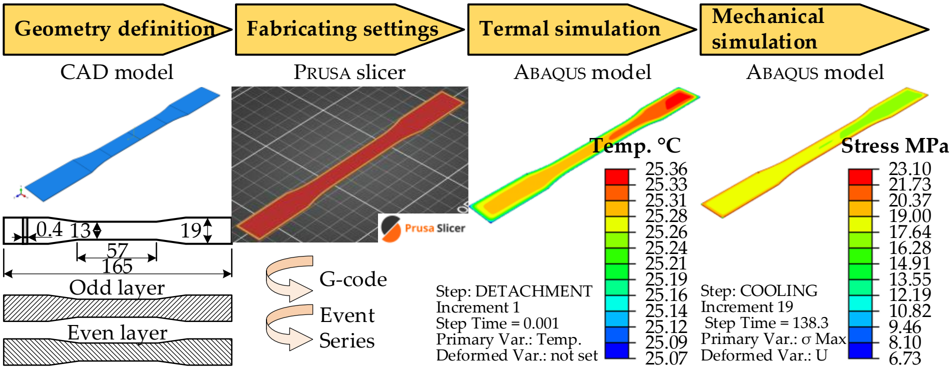

Fig. 2.6. Numerical simulation workflow

Thus, in the first fabrication trial, the dumbbell-shaped test sample layout included two solid shells along the perimeter of the print; the inner part of the specimen was printed in 11 layers, yielding a total thickness of 3.2 mm. The first layer height was 0.2 mm, with subsequent layers at 0.3 mm each, and a 100% infill with a ±45° orientation, alternating the infill angle between layers. Printing was conducted using a 0.4 mm nozzle at 210 °C and a speed of 30 mm/s; the printing bed temperature was maintained at 60 °C. Warpage was observed at the microscale in the 3D printed part. To observe macroscale warpage, the second fabrication stage used the same parameters as the first but with a reduced thickness of 0.4 mm, printed in two layers of 0.2 mm each. This modified geometry was selected to facilitate observation of warpage during physical testing.

2.8.2. Fabrication code conversion and element activation

A central innovation of this study is the automated conversion of G-code into a time-resolved event series compatible with FE simulations in ABAQUS (Simula, Dassault Systems, Version 2020, Providence, RI, USA). G-code, which encodes the printer's toolpath and associated process parameters, is parsed using a custom Python script. This script extracts the time-dependent filament centerlines and deposition sequences from the G-code file generated by slicing software. It converts them into an event series that defines the activation intervals of finite elements within the simulation domain. The resulting event series specifies the nozzle's position in the *x*, *y*, and *z* axes over time, as well as the extrusion status, as shown in Table 2.2. The *x*, *y*, and *z* columns specify the spatial coordinates of the extruded filament centerline at time *t*. The final column indicates the deposition status, where 1 denotes active extrusion, and 0 represents non-depositing movements. Since the deposition path in the G-code is not always continuous, the nozzle may perform non-depositing movements during travel. The filament cross-section was approximated as a rectangle, with dimensions matching the major and minor axes of the elliptical profile shown in Figure 2.7.

Table 2.2. A fragment of an event series input example

t [s]	*x* [mm]	*y* [mm]	*z* [mm]	Activation
0	–8.75	0.20	49.74	0
0.0003	–8.75	0.20	49.74	1
0.0096	–8.75	0.20	89.25	1
0.0138	8.75	0.20	89.25	1
0.0231	8.75	0.20	49.74	1
0.0234	8.45	0.20	48.68	1
…	…	…	…	…

The element activation strategy uses a progressive element birth approach, in which elements are activated when their centroids intersect the defined deposition path. This method, first introduced by Zhang and Chou (2006), has been widely adopted in simulations for its ability to replicate the sequential nature of FFF. In this study, the filament's elliptical cross-section was approximated as a rectangle, and a binary state variable was assigned to each element, indicating activation (1) or inactivity (0) at a specific time. The generated G-code includes the necessary instructions for FFF, such as printing speed, extrusion temperature, and print path. As previously described, the custom Python script transforms this G-code into an event series for FE analysis. Figure 2.7 illustrates the element activation process, which is based on the time-dependent filament coordinates provided by the event series described in Table 2.2. As shown in Figure 2.7, the filament's elliptical cross-section is approximated as a rectangle. Thus, an element is activated and included in the analysis if its center lies within these rectangular boundaries.

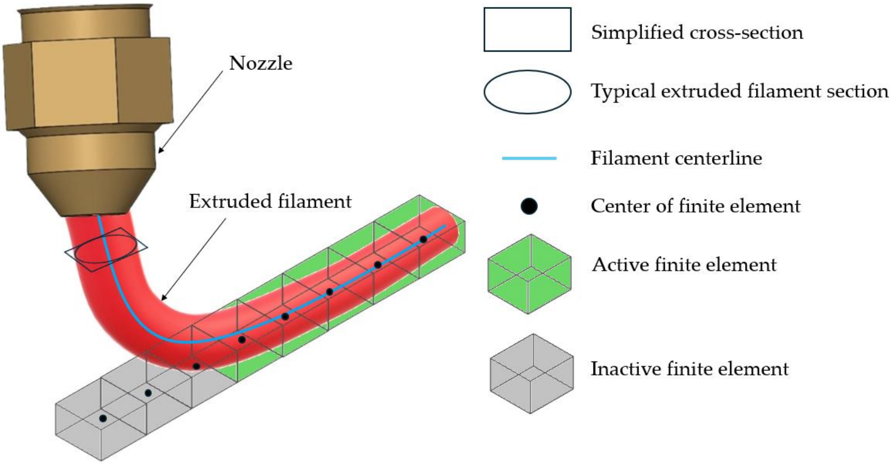

Fig. 2.7. Element activation approach

This approach is consistent with the methodology used by Syrlybayev et al. (2021), who applied a similar element activation scheme to simulate warpage in FFF parts. Their work demonstrated that accurate modeling of the deposition sequence significantly improves the prediction of thermal gradients and mechanical distortions. The present study extends this concept by integrating the event series directly into the FE simulation framework, enabling a seamless transition from slicing to simulation.

Automating G-code conversion significantly improves simulation efficiency, enhancing reproducibility and scalability of simulation workflows. This capability is particularly valuable for parametric studies and optimization tasks, where multiple simulations must be conducted under varying process conditions.

2.8.3. Thermal simulation

In the FFF process, the filament is extruded at a temperature T_f and deposited onto a heated build platform maintained at T_b. The classical heat conduction equation governs the transient thermal behavior of the printed part (Hussein et al., 2013):

$$\rho c \frac{\partial T}{\partial t} = \nabla \cdot (k \nabla T) + q, \tag{2.12}$$

where ρ is the material density, c is the specific heat capacity, $\frac{\partial T}{\partial t}$ is the time rate of change of temperature, T is the temperature, ∇ is the divergence operator, k is the thermal conductivity, and q is the internal heat source.

The initial temperature distribution follows Schoinochoritis et al. (2017):

$$T(x,0) = T_f, \quad x \in \Omega_{f;} \tag{2.13a}$$

$$T(x,0) = T_b, \quad x \in \Omega_b, \tag{2.13b}$$

where the vector $\boldsymbol{x} = (x, y, z)$ determines the position; Ω_f is the boundary of the extruded and deposited material; Ω_b is the surface of the print bed; T_f and T_b are the extrusion and print bed temperatures. The Neumann boundary conditions, accounting for convective and radiative heat exchange, are expressed as follows (Schoinochoritis et al., 2017):

$$k_f \frac{\partial T}{\partial n} + q_c + q_r = 0, \quad \boldsymbol{x} \in S(t), \tag{2.14a}$$

where $S(t)$ is the external surface of the body (changing during the element activation); $\boldsymbol{n}$ is the vector normal to the surface of the body; q_c and q_r represent the convective and radiative heat fluxes, which are defined as follows:

$$q_c = h(T - T_s); \tag{2.14b}$$

$$q_r = K_b(T^4 - T_s^4)e, \tag{2.14c}$$

where h is the heat transfer coefficient, K_b represents the Stefan-Boltzmann constant, T_s is the surrounding temperature, and e is the emissivity.

Table 2.3 summarizes the temperature-dependent physical properties of PLA used in the thermal simulation, as reported by Espinach et al. (2018), Farah et al. (2016), and Song et al. (2017). In this table, T is the material temperature; E is the deformation modulus; ν is Poisson's ratio; σ_y is the yield strength; α is the thermal expansion coefficient; k is the thermal conductivity; c is the specific heat capacity; ρ is the density. The transient thermal simulation used 3D eight-node linear heat-transfer brick elements (DC3D8) in ABAQUS (Simula, Dassault Systems, Version 2020, Providence, RI, USA). Figure 2.8 illustrates the thermal problem considered in this work. This formulation requires specifying the temperature-dependent thermal properties of the PLA filament, as well as the filament and printing bed temperatures (T_f and T_b), the emissivity (surface radiation) factor (e), the heat transfer coefficients of the filament and build platform (h_f and h_b), and the surrounding and room temperatures (T_s and T_a). The simulation comprised three distinct phases: printing, cooling, and detachment. During printing, newly activated elements were initialized at an extrusion temperature of 210 °C, while the build platform was maintained at 60 °C. These boundary conditions were applied exclusively during the printing phase and removed during cooling and detachment to replicate the physical release of the printed part.

Table 2.3. Physical properties of PLA material

T [°C]	E [MPa]	v [–]	σ_y [MPa]	$\alpha\times10^{-5}$ [1/°C]	k [W/(m·°K)]	c [J/(kg·°K)]	ρ [kg/m^3]
25	1860	0.36	25.0	7.9	0.11	1590	1250
30	1800	0.36	25.0	7.9	0.11	1590	1250
40	1727	0.36	25.0	7.9	0.11	1590	1250
50	1603	0.36	18.9	7.9	0.11	1590	1250
60	1000	0.36	15.3	7.9	0.11	1750	1250
70	300	0.36	11.7	7.9	0.11	2300	1250
80	50	0.36	8.2	7.9	0.11	1590	1250
90	10	0.36	7.0	7.9	0.11	1590	1250
100	1*	0.36	7.0	7.9	0.11	1950	1250
150	1*	0.36	7.0	7.9	0.11	1950	1250
200	1*	0.36	7.0	14.4	0	1950	1250
210	1*	0.36	7.0	14.4	0	1950	1250
220	1*	0.36	7.0	14.4	0	1950	1250

* Assumed non-zero value to ensure the solution converges.

Heat transfer was modeled using the temperature-dependent thermal properties of PLA reported by Khanafer et al. (2022) and Syrlybayev et al. (2021). The film coefficients were set at 72 W/m^2·°C during printing and 67 W/m^2·°C during cooling, while the emissivity values were 0.92 and 0.0, respectively. These values were selected based on experimental data and validated modeling practices in the literature. For example, Khanafer et al. (2022) used similar thermal parameters to simulate heat flow in FFF processes, emphasizing the importance of accurate boundary conditions in predicting thermal gradients.

The thermal model also considered conduction between the filament and the build platform, as well as between adjacent filament layers. Convection to the surrounding environment was included to simulate natural cooling (Fig. 2.8). The detachment stage was assumed to involve no heat exchange, representing the part's removal from the printer and exposure to ambient conditions. This staged thermal modeling approach is consistent with the methodology proposed by Cattenone et al. (2019), enabling comprehensive simulation of residual stress evolution and post-printing deformation. The present study builds on this by explicitly modeling the detachment phase, which is critical for understanding warpage behavior in the part's unsupported regions.

The simulations were performed by varying the number of FE in the model from 9000 to 548720 and were executed on a workstation equipped with 16 GB of RAM and an AMD Ryzen 9 5900HX processor running at 3.30 GHz. Additional FE simulations were performed to evaluate the sensitivity of warpage to variations in extrusion temperature. Increasing the temperature from 200 °C to 220 °C, as recommended by the manufacturer's datasheet. Within the manufacturer's allowable range, the selected temperatures reflect a practical scenario encountered in desktop FFF.

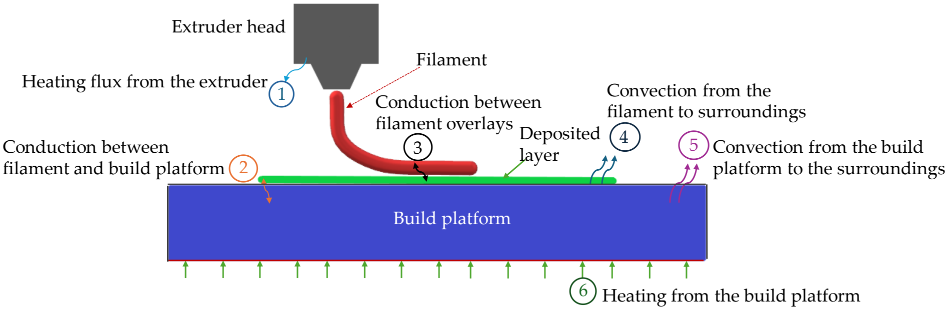

Fig. 2.8. Heat transfer scenarios during the fused filament fabrication process

2.8.4. Mechanical simulation

In ABAQUS, engineering quantities are represented in Voigt notation rather than in tensor form, with the internal tensor-to-matrix transformation (Voigt mapping) performed automatically by the software. Thus, it internally transforms the assumed physical properties (Table 2.3) into second- and fourth-order tensor mappings, thereby building the stiffness matrix $S(T)$. Cattenone et al. (2019) incorporated the computed time-dependent temperature distribution as externally prescribed, solution-independent conditions into a thermo-elastic-plastic constitutive model to evaluate the total strain, which is expressed as follows:

$$\varepsilon = \varepsilon_e + \varepsilon_{pl} + \varepsilon_t, \tag{2.15a}$$

where ε is the total strain, and ε_e, ε_{pl}, and ε_t are the elastic, plastic, and thermal strain components, with individual components defined as follows:

$$\varepsilon_e = S(T) \cdot \sigma, \tag{2.15b}$$

$$\varepsilon_{pl} = \lambda \sigma_{dev}, \tag{2.15c}$$

$$\varepsilon_t = \alpha(T)\nabla T, \tag{2.15d}$$

where σ is the stress in Voigt notation; $S(T)$ defines temperature-dependent compliance (the inverse of stiffness matrix); σ_{dev} is the deviatoric part of the stress tensor; $\alpha(T)$ determines the temperature-dependent second-order coefficient of thermal expansion tensor; λ is the plastic flow factor, determined according to the following criterion (Lubliner, 2008):

$$\lambda \begin{cases} = 0, & \sigma_{vm} < \sigma_y(T); \\ > 0, & \sigma_{vm} \geq \sigma_y(T), \end{cases} \tag{2.16}$$

where σ_y is the yield stress and σ_{vm} is the effective Von Mises stress that can be described as follows:

$$\sigma_{vm} = \sqrt{2(\sigma_{dev})^T \sigma_{dev}/3}, \tag{2.17}$$

where the operator $(\square)^T$ indicates transposing the deviatoric part of the tensor.

Eq. (2.16) describes two cases: (1) the elastic behavior of the material when the equivalent stress is below the yield stress; this means no plastic deformation occurs, and therefore, the plastic flow multiplier (λ) is zero, keeping the stress state within the yield surface boundary; and (2) the material undergoes plastic deformation when the equivalent stress reaches or exceeds the yield stress. In this case, the stress state is on the yield surface. Eq. (2.16) is valid for describing neat PLA, as the material can be reasonably approximated as an isotropic thermo-elastic-plastic continuum. Under these assumptions, the Von Mises yield criterion provides an appropriate description of the initiation of plastic deformation in the polymer during the deposition, cooling, and detachment stages of the FFF process simulation. The short-fiber-reinforced composites are modeled using a more advanced multiscale homogenization framework that accounts for the composite microstructure through RVE-based material modeling.

The mechanical simulation employed 20-node quadratic brick elements (C3D20R) and used the temperature distribution from the thermal model as a solution-independent boundary condition. During printing and cooling, the bottom surface of the specimen was constrained in all translational degrees of freedom to simulate adhesion to the build platform. Figure 2.9 shows the boundary constraints. These constraints were removed during the detachment phase to simulate the release of residual stresses and the onset of warpage. The mechanical simulation predicted residual stress accumulation and geometric deformation, with maximum displacement localized at the specimen edges due to non-uniform cooling. This behavior aligns with the findings of Zhang and Chou (2008), who noted similar deformation patterns in ABS components. The current study confirms that PLA exhibits similar behavior, with stress accumulation during cooling and relaxation upon detachment.

A convergence study was conducted to determine the optimal mesh density and time step. The convergence study revealed that a mesh resolution of one element per filament cross-section yields adequate accuracy, with minimal variation in predicted warpage. This finding aligns with the recommendations of Barocio et al. (2019), who emphasized the importance of mesh refinement in capturing localized thermal and mechanical gradients. Espinach et al. (2018) reported that PLA exhibits significant shrinkage during cooling, which must be adequately accounted for in the model to ensure reliable prediction of warpage. The current study incorporates temperature-dependent material properties to enhance the simulation's fidelity.

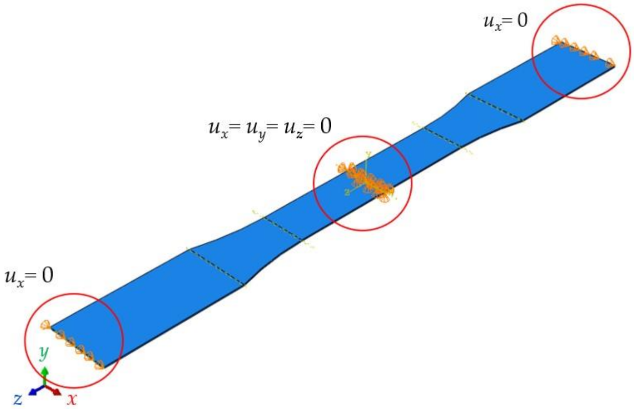

Fig. 2.9. Detachment boundary conditions

2.9. Conclusions of the Second Chapter

This chapter outlines the methodological framework used to investigate PLA-based components manufactured by FFF, integrating mechanical testing, thermal and viscoelastic characterization, microstructural analysis, and thermo-mechanical FE simulations. The obtained conclusions are as follows:

1. A two-track research structure was established to investigate continuous-fiber reinforcement and short-fiber-filled PLA composites under

controlled FFF conditions. This organization ensures methodological consistency by fabricating all materials with identical printing parameters and standardized specimen geometries.

2. Continuous-fiber reinforcement was implemented through a coaxially impregnated aramid-PLA filament manufactured on a modified extrusion line and processed on an ordinary desktop FFF printer. This approach enables uninterrupted deposition of the reinforcement pathway. It is expected to clarify the practical applicability and processing constraints of continuous reinforcement under conventional printing conditions by separating filament-manufacturing conditions from the subsequent printing-stage imperfections.
3. A reference mechanical-testing baseline was established using standardized ASTM D638 and D3039 geometries. This systematic approach provides a consistent methodological foundation for comparative analysis by ensuring that short-fiber-reinforced filaments and PLA with a deliberate 40% substitution of virgin polymer by recycled material are examined within the same standardized testing framework.
4. Short-fiber PLA composites containing carbon or wood fibers were selected as commercially representative reinforcement systems, and their mechanical, thermal, viscoelastic, and microstructural characteristics were investigated using tensile and flexural testing, DSC, DMA, and SEM. This integrated methodology is expected to reveal structure-property interactions because all characterization techniques were conducted within a unified fabrication-and-testing framework.
5. Dimensional fidelity was introduced as a methodological parameter through controlled observation of warpage during cooling, linking fabrication quality to thermal contraction and constrained shrinkage in FFF. Combining this metric with the short-fiber investigation provides a coherent basis for subsequent process modeling because geometric deviation is treated as an inherent thermo-mechanical outcome rather than an isolated print defect.
6. The coupled thermo-mechanical simulations were formulated to enable the prediction of FFF-induced warpage and to evaluate the evolution of residual stresses that accompany the thermal cycle. This finite-element modeling framework was adopted to reproduce the printing, cooling, and detachment phases for neat and composite PLA materials. To support this framework, an automated G-code parsing procedure was developed to convert the slicer-generated toolpath into a time-resolved event series for finite-element activation. This solution accelerates model preparation and reduces manual implementation errors by transferring the deposition sequence directly from the fabrication model to the numerical domain.

3

Characterization and Simulation of Mechanical Performance and Process-Induced Deformation

This chapter presents experimental and numerical results to clarify how material selection, reinforcement strategy, and process conditions affect the mechanical performance and fabrication quality of FFF-printed PLA components. It integrates tensile and flexural testing, thermal and viscoelastic characterization, microstructural observations, and thermo-mechanical simulations (the Second Chapter) to explain the relationships among reinforcement architecture, process-induced variability, and structural response. Particular attention is given to comparing unreinforced, recycled, and fiber-reinforced PLA systems and evaluating the effectiveness of continuous and short fibers in improving load-bearing capacity, ductility, dimensional fidelity, and resistance to warpage and development of the residual stresses. The analysis highlights the balance between mechanical enhancement and manufacturability, validates predictive modeling for explaining deviations between ideal and as-printed behavior, and outlines implications for designing sustainable, high-performance PLA composites for functional additive manufacturing. Accordingly, this chapter clarifies the effect of fiber on the trade-offs among strength, stiffness, ductility, and dimensional fidelity in FFF-printed PLA components, considering fiber type, fiber volume fraction, and infill density. Neat PLA, PLA-CF, and PLA-WF are evaluated under uniaxial tensile and three-point bending at multiple infill densities to distinguish densification effects from material effects. SEM, DSC, and DMA are used to identify failure-controlling microstructural features, crystallization behavior, and temperature-dependent stiffness, while thermo-mechanical modeling predicts FFF-induced warpage and residual stress. The research findings are reported in related scientific publications (Rimkus et al., 2022; Farh et al., 2024; Farh & Gribniak, 2025).

3.1. Analysis of continuously reinforced components

3.1.1. Tensile test results

Figures 3.1 and 3.2 show the tension test results for continuously reinforced (Section 2.3.2) and unreinforced specimens with a partial replacement of virgin PLA by recycled plastic (Section 2.3.1). Table 3.1 summarizes the test results. The results of Figure 3.1 indicate a substantial improvement in load-bearing capacity due to fiber reinforcement; the ultimate load increased by 67% in the reinforced samples.

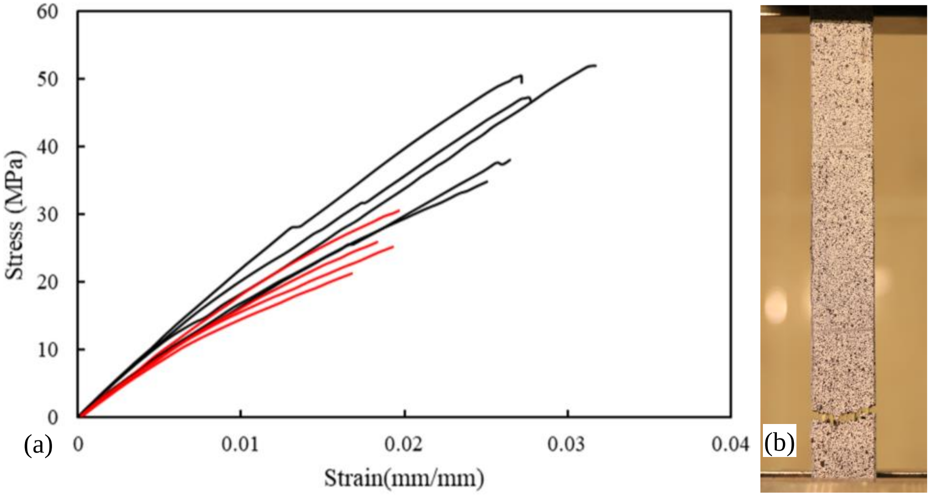

Fig. 3.1. Reinforced samples: (a) stress-strain diagrams;
(b) characteristic failure

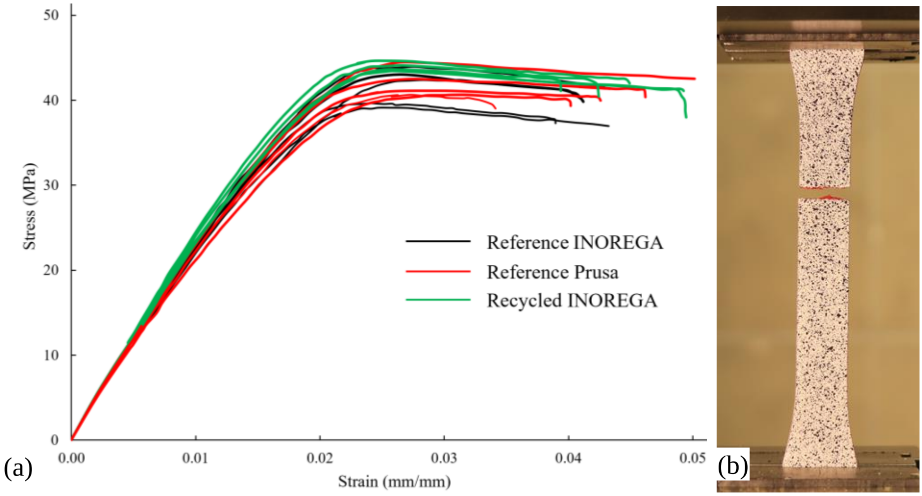

Fig. 3.2. Unreinforced samples: (a) stress-strain diagrams; (b) characteristic failure

Table 3.1 presents the mechanical performance of the tested samples, expressed as tensile strength. This table also includes the average strength value of identical specimens and the coefficient of variation (CV%). Table 3.1 and Figure 3.2a also show that the mechanical characteristics of partially recycled PLA remain competitive with the primary PLA material by Inorega and the alternative PLA by Prusa. At the same time, the recycled polymer almost doubles production efficiency, making FFF technology economically viable. Furthermore, the 40% replacement of PLA with recycled plastic appears to reduce the scatter in test results. This outcome identifies the object of further research and, therefore, motivates the development of a reinforced composite using partially recycled PLA.

Table 3.1. Summary of the tensile test results

Group	Type	Strength (MPa)	Average (MPa)	CV (%)
Unreinforced	Reference Prusa	40.8	42.1	4.00
		42.6		
		41.3		
		44.6		
		40.5		
		42.5		
	Reference Inorega	44.2	42.1	5.00
		43.0		
		42.5		

End of Table 3.1

Group	Type	Strength (MPa)	Average (MPa)	CV (%)
		43.9		
		39.3		
		39.8		
	Recycled Inorega	43.8	43.9	1.26
		43.2		
		44.2		
		43.6		
		43.7		
		44.8		
Reinforced	Reference (unreinforced) Inorega	33.3	31.4	14.4
		28.6		
		38.4		
		27.5		
		29.0		
	Reinforced Inorega	47.3	50.8	5.10
		52.3		
		50.7		
		49.5		
		54.1		

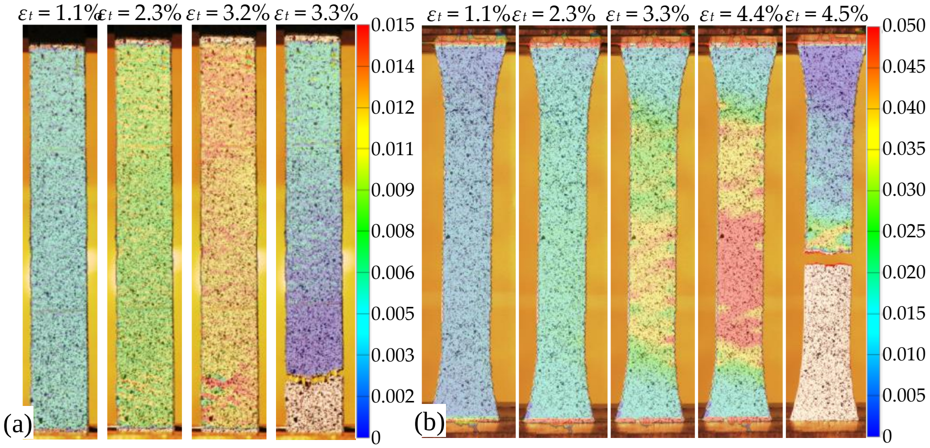

Fig. 3.3. Strains mapped with DIC: (a) reinforced plate; (b) unreinforced sample

Figure 3.3a shows an example of DIC analysis. These results align with the Prusa manufacturer's specified characteristics of such specimens: the modulus of elasticity E_p = 2.2 GPa; the yield strength f_y = 50.8 MPa; the elongation at the yielding point ε_y = 2.9%.

3.1.2. Evaluating fabrication quality

Gribniak et al. (2021a, 2021b) related the reinforcement efficiency of continuous filaments in an FRP composite to the bonding performance of the reinforcing material in a polymer matrix. Post-processing, such as cutting test samples, can diminish the validity of the mechanical analysis. Furthermore, the relatively small diameter of the aramid yarn in this study complicates the analysis of the fiber-bond defects in the tensile samples. This study includes reinforced specimens made of transparent PLA from the same producer as the polymeric material used in the mechanical tests (Fig. 3.4a). This solution allows investigation of fiber-matrix bonding using an optical microscope without cutting the samples.

The 250 × 18 × 3 mm square-plate specimen was printed in transparent PLA to assess bond quality and fiber alignment. The interfacial connection was observed using a 100× digital microscope DG-3X (Scalar, Japan). Figure 3.4b shows the fiber-matrix bonding fragment, which exhibits visible defects in the bond due to air voids around the fiber. Notably, Figure 3.4b illustrates the duplicated manufacturing process, in which the aramid yarn was first reinforced into the extruded PLA filament, and the 3D printer then produced the reinforced product. Thus, this methodology accumulates the defects of both manufacturing stages. Therefore, such FFF technology raises the quality requirements for raw materials. This requirement differs from that of the technology considered for the FFF process, in which the reinforcement yarn is consolidated with the polymer during 3D printing.

On the other hand, current manufacturing equipment enables control of the quality of the reinforced PLA extrusion process. At the same time, the standardized dimensions of the reinforced filament enable printing of reinforced components with slightly customized 3D printers, making the manufacturing process more flexible. Remarkably, the customization process should also account for printing parameters, such as nozzle diameter, printing speed, and temperature. Figure 3.5 illustrates the printing results for the specimens using non-optimal printing parameters (chosen solely to ensure a stable printing process). Switching from a 0.4 mm nozzle to a 0.8 mm nozzle produced a more uniform distribution of the reinforcement yarn in the printed structure. However, the customized parameters did not allow precise geometry to form in both samples.

When the default settings are altered, the resulting cross-sectional shapes are irregular (Figs. 3.5a and 3.5b). The irregularities become apparent in the reference sample (Fig. 3.5c). This result indicates there is sufficient room to improve the

FFF parameters. The partial debonding of the aramid yarn (Fig. 3.1b) could reduce the stiffness of the reinforced polymer. Q. Hu et al. (2018) reported that yarn impregnation before PLA filament extrusion could improve bond quality. Additionally, yarn alignment in the printed specimen significantly affects the mechanical performance of the resulting product (Goh et al., 2019). Therefore, the filament must be stretched without weaving or misalignment. The ability of FFF printing equipment to stretch the filament could solve this problem (Abtew et al., 2020).

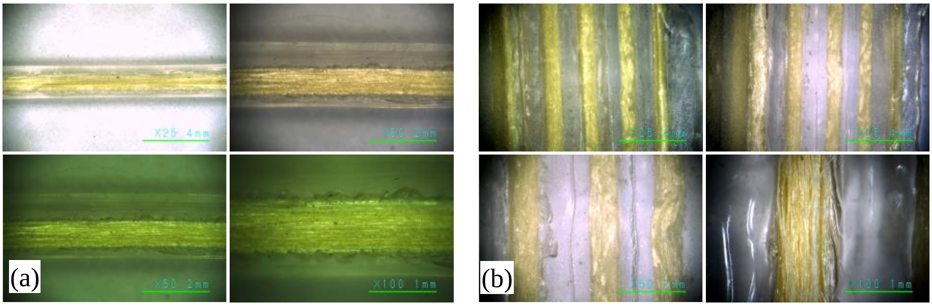

Fig. 3.4. Reinforced samples from transparent PLA: (a) raw material (reinforced PLA filament); (b) printed reinforced sample at different magnifications

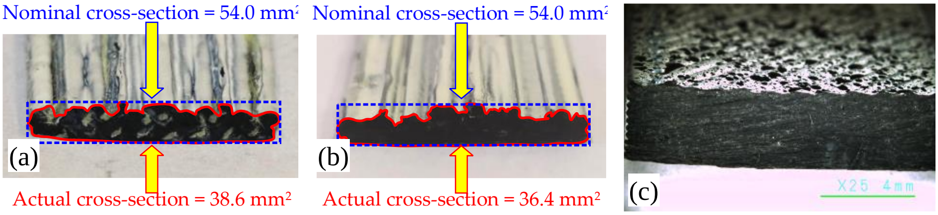

Fig. 3.5. Printing defects: (a) reinforced specimen; (b) unreinforced sample manufactured through a 0.8 mm nozzle; (c) unreinforced reference produced through a 0.4 mm nozzle

3.1.3. Reinforcement efficiency and mechanical performance

This study employs the approach of Gribniak et al. (2021a, 2021b) to quantify the efficiency of the developed reinforced composite using the nonlinear finite element (FE) software Atena, as described in Section 2.3.3. The 3D solid FE model represents the polymer matrix, and fracture mechanics principles describe PLA failure. A 1D material model coincides with the FFF direction and determines the reinforcement; an elastic-brittle constitutive law defines fiber failure.

At the first stage, the constitutive PLA law was tailored using the "Reference Inorega" samples (Fig. 3.1a). Figure 3.6a shows the FE model using isoparametric eight-node hexahedral finite elements with an average size of 0.7 mm and eight Gauss integration points. The FE model approximates the actual cross-section dimensions (Fig. 3.5b). The modeled steel plates protect the specimen supports, as in the physical tests. Isoparametric eight-node brick finite elements with eight integration points are used to discretize the steel plates, assuming perfect contact with the polymer. The Newton-Raphson iteration procedure controls the solution of the deformation problem.

Figure 3.6b shows the model verification results, identifying the following parameters: a 2.2 GPa modulus of elasticity; a 100 MPa tensile strength; and a 58 N/m fracture energy. Remarkably, the calibrated strength exceeds twice the maximum stress estimated in Figure 3.7a. The possible explanation for the increase in strength relates to the printing pathway, which corresponds to the tensile stresses. Differences in the solidification structure could also alter the estimated strength. The results, shown in Figure 3.7a, assume a monolithic structure for the printed PLA. However, Figures 3.4 and 3.5 show voids and defects that reduce the cross-sectional area. In light of these findings, particular care should be taken when applying the nominal characteristics of the polymeric material in the numerical analysis of manufactured structures, given the FFF effect on the material's structure, which is far from monolithic (Abouzaid et al., 2021).

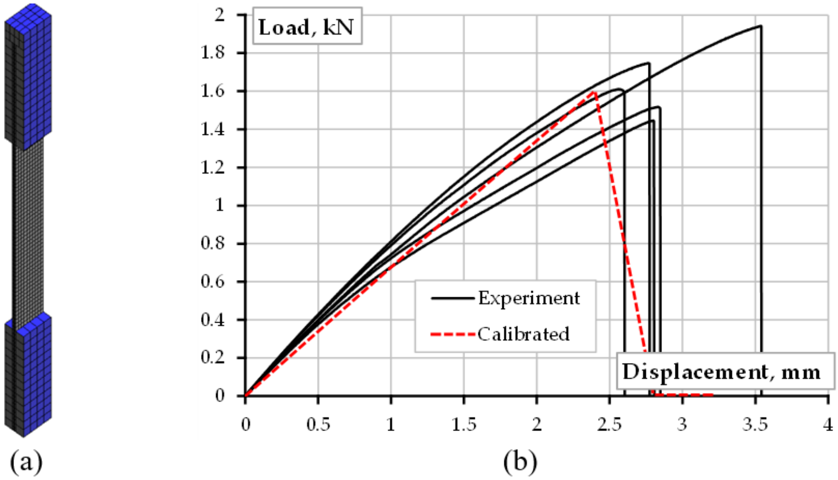

Fig. 3.6. Unreinforced sample: (a) FE model; (b) model verification result

At the second stage, the volumetric fiber content was the simulation variable (all other model parameters were kept constant); the simulated geometry approximated the cross-section. Figure 3.7 shows the simulated stress distribution in the reinforced specimen and compares the numerical prediction and test results. The tensile displacement, applied in small increments (0.3 mm), determined the model's load-bearing capacity. The first model assumes a volume fraction V_f = 22%, corresponding to the nominal reinforcement content; the overestimation of the axial stiffness, *EA*, and the strength, f_u, is apparent. Reducing the fiber content to 3.0% and 1.5% remedies the strength values and stiffness predictions, respectively. Thus, Eq. 3.6 defines a 6.8% reinforcement efficiency with respect to axial stiffness, increasing to 13.6% with respect to load-bearing capacity.

The simulation results with the reference fiber content (V_f = 22%, Fig. 3.7) define the space for improving FFF technology to develop reinforced composites. At the same time, the experimental results reveal beneficial ductility in the developed composite; the deformation at the test specimens' maximum resistance exceeds 1.35 times the predicted value. This outcome determines the object for further analysis. Additionally, a comparative study of DIC-traced relative displacement maps (Fig. 3.3) reveals a uniform strain distribution in the reinforced specimens until the onset of polymer fracture, supporting the continuous reinforcement concept.

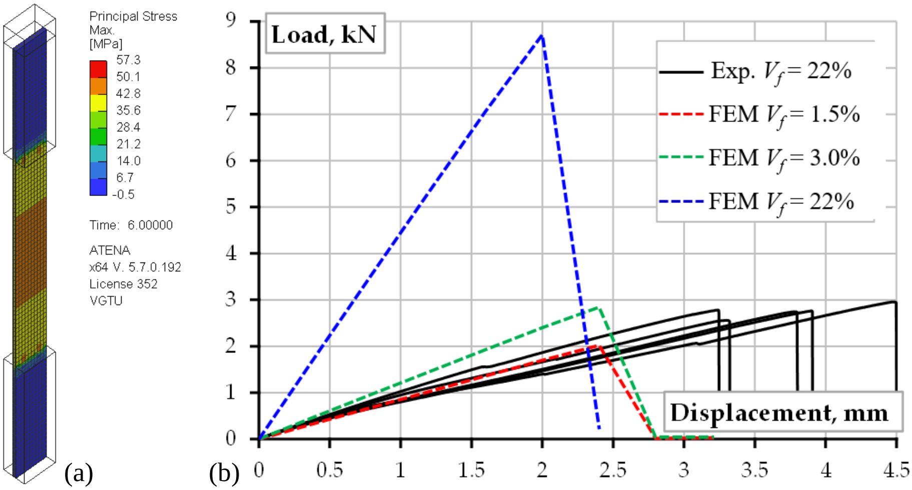

Fig. 3.7. Reinforced sample: (a) predicted stress distribution; (b) efficiency estimation results where Exp. and FEM denote the experimental and finite element models, respectively

3.1.4. Sustainability and polymer recycling perspectives

Despite the complexity of recycling (Colorado et al., 2020), existing technologies enable efficient reuse of PLA materials. Paciorek-Sadowska et al. (2019) and X. G. Zhao et al. (2018) formulated the principles for adapting recycled PLA for

FFF. The low-temperature printability, along with a solid scientific foundation in the literature, stimulates investigations into PLA waste recycling and makes it a valuable resource for further AM development. Anderson (2017) and Peinado et al. (2015) demonstrated the efficient applicability of reused PLA (recycled up to 20 times) without noticeable loss of mechanical performance in the FFF components. The present study's outcomes also support the hypothesis that there is no adverse effect from the application of recycled polymers. Two observations can be made based on Table 3.1 and Figure 3.2:

- The 40% replacement with recycled material considered in this study does not harm the PLA strength and modulus of elasticity. At the same time, this modification nearly halved the cost of PLA, making FFF economically viable. Future research should optimize the replacement content.
- The considered modification reduced the strength scatter (CV in Table 3.1). This result indicates a beneficial effect of recycled plastic on the mechanical performance of FFF parts, warranting further research.

3.1.5. Limitations of the proposed approach

Using pre-impregnated continuous fiber-reinforced PLA filaments in a standard single-extruder FFF system has inherent limitations that become more pronounced when transitioning from simple, flat test specimens to complex 3D structures. While tensile specimens printed using this method exhibit enhanced mechanical performance due to the superior tensile strength of continuous fibers, the technique faces significant scalability challenges, particularly for applications such as drone components or structurally demanding geometries. A fundamental limitation lies in the lack of control over fiber orientation and placement in three-dimensional space. Current open-source slicing software generates two-dimensional, layer-by-layer toolpaths that are inadequate to handle uninterrupted, curvilinear reinforcement trajectories within volumetric objects. This constraint leads to inefficiencies in fiber alignment and compromised structural continuity, especially in non-planar or overhanging sections. Moreover, the inability to dynamically adjust fiber paths limits the ability to customize reinforcement layouts to meet load-bearing demands across different regions of the part. Fiber buckling, misalignment, and delamination are likely to occur when the filament is forced to conform to complex surfaces without appropriate in-situ control mechanisms, such as robotic fiber placement or multi-axis toolpath adaptation.

In addition, using a single extruder inherently limits the ability to modulate fiber volume fraction or selectively alternate between reinforced and non-reinforced regions during printing. Experimental evidence has also shown that, even in flat specimens, reinforcement efficiency is significantly reduced, with stiffness contributions reaching only approximately 31.8% of the theoretical potential, largely due to poor fiber-matrix bonding and geometric irregularities introduced during filament production and deposition. These drawbacks are compounded in complex geometries, where achieving dimensional precision, material homogeneity, and continuity of reinforcement is more difficult.

As a result, the method proves inadequate for manufacturing high-performance, large-scale, or intricately shaped components that require tailored mechanical behavior and reliability. Given these limitations, short-fiber-reinforced filaments offer a more practical alternative. This approach, while offering slightly lower mechanical performance, enables an isotropic distribution of reinforcement, compatibility with existing software and hardware, and the reliable fabrication of complex geometries without the need for sophisticated fiber-management systems. The trade-off favors printability and structural consistency over maximum tensile strength, particularly in applications where geometric complexity and reproducibility are prioritized.

3.2. Characterization of a short-fiber-reinforced polymer

The results are discussed as follows: mechanical performance is first evaluated through tensile and flexural testing (Section 2.3.4), in which the effects of infill density across filament types (PLA, PLA-CF, PLA-WF) on stiffness, strength, ductility, and energy absorption are quantified. Table 3.2 summarizes the test results, and Figures 3.8 and 3.9 show the representative load-displacement responses.

The mechanical trends are then interpreted using thermal (Section 2.4) and thermomechanical (Section 2.5) characterization, relating changes in crystallization behavior (e.g., cold crystallization and crystallinity level) and the temperature-dependent retention of stiffness in the glass-transition region to the mechanical performance of PLA composites. The discussion is linked to microstructural observation from SEM (Section 2.6), emphasizing interfacial gaps, voids, and fracture features to explain the observed strength trade-offs and damage-tolerance mechanisms in the composites. Finally, process-induced dimensional effects are addressed through warpage observations, which relate residual stress and part distortion during cooling to the stabilizing role of short-fiber reinforcement and highlight implications for print fidelity and dimensional accuracy.

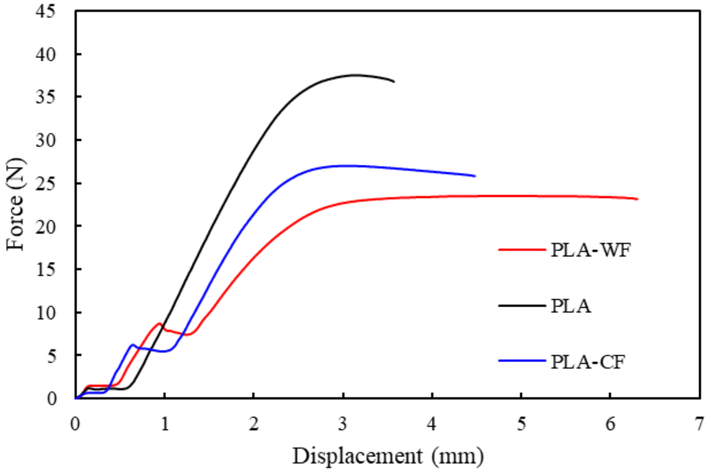

Fig. 3.8. Load-displacement curve for the tensile samples with 100% infill density

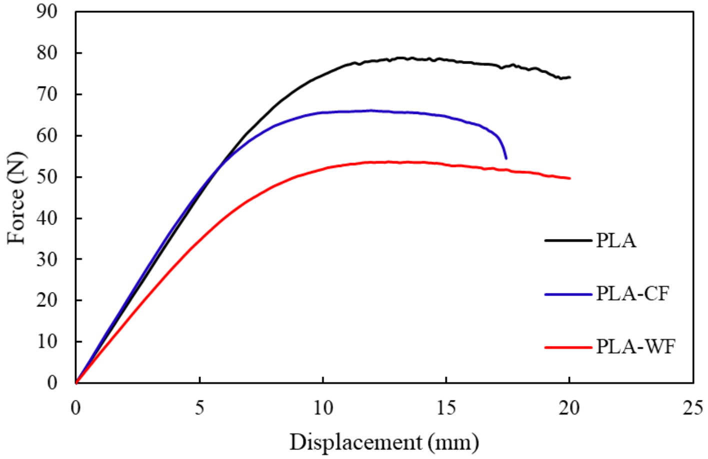

Fig. 3.9. Average force-displacement curve for the flexural samples with 100% infill

3.2.1. Comparative analysis of tensile and flexural properties

Table 3.2 summarizes the tensile properties of the printed specimens as a function of infill density and filament type. Across all materials, increasing infill density from 20% to 100% consistently improved load-bearing performance, reflecting a larger effective cross-sectional area, reduced internal void content, and a more continuous stress-transfer path through the gauge section. For neat PLA, Young's modulus increased from 1.45 ± 0.11 GPa (20% infill) to 2.08 ± 0.15 GPa (100% infill), while tensile strength increased from 25.0 ± 0.65 MPa to 39.9 ± 2.10 MPa.

A similar monotonic trend was observed for toughness, which increased from 256 kJ/m³ at 20% to 813 kJ/m³ at 100%, consistent with progressively improved interlayer bonding and reduced premature crack initiation associated with porosity. Elongation at break also increased modestly for PLA, from 2.95 ± 0.48% to 3.87 ± 0.45%, suggesting that densification improved strain accommodation by delaying void-driven localization.

Table 3.2. Summary of tensile mechanical properties

Filament	Infill density	Young's modulus	Tensile strength	Elongation at break	Toughness	Specific strength
	(%)	(GPa)	(MPa)	(%)	(kJ/m^3)	(MPa/g)
PLA	20	1.45 ± 0.11	25.0 ± 0.65	2.95 ± 0.48	256	3.50
	60	1.98 ± 0.05	32.1 ± 0.45	3.31 ± 0.47	547	3.90
	100	2.08 ± 0.15	39.9 ± 2.10	3.87 ± 0.45	813	4.23
PLA-CF	20	1.23 ± 0.02	18.3 ± 0.29	3.63 ± 0.12	293	2.85
	60	1.36 ± 0.03	21.2 ± 0.41	4.18 ± 0.33	763	2.88
	100	1.92 ± 0.02	27.2 ± 0.20	4.45 ± 0.05	985	3.22
PLA-WF	20	1.05±0.02	16.35± 0.35	3.24±0.27	339	2.39
	60	1.24±0.03	19.32± 0.51	3.81±0.21	808	2.48
	100	1.38 ± 0.03	24.1 ± 0.60	5.60 ± 0.70	1268	2.67

Table 3.2 shows that, for the reinforced filaments, the same infill-driven improvements were observed, but with lower absolute stiffness and strength than those of neat PLA at equivalent infill densities. PLA-CF increased in modulus from 1.23 ± 0.02 GPa to 1.92 ± 0.02 GPa and in strength from 18.3 ± 0.29 MPa to 27.2 ± 0.20 MPa as infill increased from 20% to 100%. PLA-WF exhibited a smaller modulus gain (from 1.05 ± 0.02 to 1.38 ± 0.03 GPa) and lower strength overall (from 16.35 ± 0.35 to 24.1 ± 0.60 MPa), consistent with the presence of out/bridging, which becomes more effective as internal porosity is minimized. Damage must propagate through a denser volume of short fibers and associated

microstructural discontinuities, which can reduce effective interlayer cohesion and introduce stress concentrators. Despite the reduced strength, both composites showed markedly enhanced energy absorption at 100% infill; toughness reached 985 kJ/m^3 for PLA-CF and 1268 kJ/m^3 for PLA-WF, exceeding that of neat PLA (813 kJ/m^3). This behavior is consistent with composite-specific dissipation mechanisms such as crack distortion, interfacial debonding, and fiber pull-out.

At 100% infill, the material ranking highlights a clear trade-off between strength/stiffness and ductility/energy absorption. Neat PLA delivered the highest tensile strength (39.9 MPa, Fig. 3.8) and modulus (2.08 GPa). At the same time, PLA-WF exhibited the highest elongation at break (5.60 ± 0.70%) and the highest toughness (1268 kJ/m^3), indicating superior resistance to unstable crack growth under tension. PLA-CF occupied an intermediate position, with moderate stiffness recovery at full infill (1.92 GPa) and elevated toughness (985 kJ/m^3) relative to neat PLA. Table 3.2 shows that increasing infill density is the primary driver of improved tensile performance across all filament types. At the same time, the introduction of short fibers shifts the mechanical response toward greater damage tolerance (higher toughness and, for PLA-WF, higher strain-to-failure) at the expense of reduced tensile strength relative to neat PLA.

Specific strength, expressed as the strength-to-mass ratio, was used as a normalized efficiency index to compare tensile performance across materials and infill densities, while accounting for differences in specimen mass. For neat PLA, the index increased from 3.50 MPa/g at 20% infill to 4.24 MPa/g at 100% infill, indicating that densification improves load-path continuity more than it increases mass. A similar but lower trend was observed for the short-fiber composites: PLA-CF increased from 2.86 to 3.22 MPa/g, and PLA-WF from 2.39 to 2.67 MPa/g when increasing infill from 20% to 100%, confirming that the composites remain less mass-efficient in tensile than neat PLA under the same printing strategy due to defect-controlled failure (fiber pull-out, interfacial gaps, and voids). The difference between the mass increase and the strength-to-mass increase is expected because the metric is ratio-based. The mechanical benefit of higher infill is not purely proportional to added material: increasing infill simultaneously reduces void content, increases interlayer contact area, and strengthens the continuity of load-bearing pathways, which can raise the measured tensile strength faster than the specimen mass. For example, for PLA-WF, mass increased by ≈31% (from 6.85 to 9.011 g) as infill increased from 20% to 100%. In contrast, tensile strength increased by ≈47% (from 16.35 to 24.1 MPa), yielding a smaller but positive net gain of ≈12% in strength-to-mass (from 2.39 to 2.67 MPa/g); this indicates that densification improves structural efficiency through better consolidation and reduced stress concentrations, although the absolute efficiency remains limited by reinforcement dispersion and fiber-matrix bonding quality.

Figure 3.9 presents the representative force-displacement responses obtained from three-point bending, while Table 3.3 summarizes the extracted flexural parameters. Neat PLA exhibited the highest load-bearing capacity, reaching a 77.8 N peak load and a corresponding flexural strength σ_f of 45.94 MPa, indicating the most effective stress transfer through the printed structure under bending. PLA-CF showed an intermediate peak load (65.3 N) and flexural strength (38.56 MPa), but the highest flexural modulus E_f (771.6 MPa), compared with PLA (732.1 MPa), consistent with a stiffer elastic response in the initial loading stage (i.e., a steeper slope in the linear region). In contrast, PLA-WF exhibited the lowest peak load (53.2 N), flexural strength (31.42 MPa), and modulus (578.1 MPa), indicating reduced flexural stiffness and earlier damage initiation under bending.

The combined trends, in Figure 3.9 and Table 3.3, suggest that reinforcement effects depend strongly on the balance between elastic stiffening and defect-controlled failure. The higher E_f of PLA-CF indicates that carbon fibers contribute to stiffness; however, the reduced $P_u$and σ_f relative to neat PLA, failure is governed by stress concentrations and interfacial debonding, which limit ultimate strength despite a stiffer response. PLA-WF shows the largest reductions in both modulus and strength, consistent with weaker fiber-matrix interactions and more significant microstructural discontinuities, which promote earlier crack formation.

Table 3.3. Average flexural properties

Material	P_u (N)	σ_f (MPa)	E_f (MPa)
PLA	77.8	45.94	732.1
PLA-CF	65.3	38.56	771.6
PLA-WF	53.2	31.42	578.1

3.2.2. Thermal transitions and crystallinity

The DSC results (Fig. 3.10 and Table 3.4) indicate that adding CF and WF affects PLA crystallization behavior more than the glass transition. In both heating cycles, the glass transition temperature remained close to 60 °C, with T_g = 60.8 °C (PLA), T_g = 61.9 °C (PLA-CF), and T_g = 61.0 °C (PLA-WF) during the first and second heating, T_g ranged from 59.1 to 60.0 °C, suggesting that the fillers have a limited effect on segmental mobility in the amorphous PLA phase. In contrast, clear differences were observed in cold crystallization. During the first heating, the cold-crystallization peak shifted to lower temperatures with reinforcement, particularly for WF, where T_{cc} decreased from 116.8 °C (PLA) to 114.9 °C (PLA-CF) and 111.7 °C (PLA-WF), consistent with enhanced heterogeneous nucleation and an earlier onset of ordering upon heating. The associated enthalpy of cold crystallization, ΔH_{cc}, was 18.1 J/g (PLA), 16.6 J/g (PLA-CF), and 19.5 J/g (PLA-WF). In contrast, the melting enthalpy, ΔH_m, was 19.4 J/g (PLA), 19.1 J/g (PLA-CF), and 20.4 J/g (PLA-WF), indicating a larger crystalline contribution for PLA-WF. Melting occurred over a narrow range typical of PLA. Still, PLA-WF consistently showed the highest melting temperature, at 153.4 °C in the first heating and 152.5 °C in the second, suggesting slightly more stable, better-developed crystals. After thermal history removal, PLA-CF exhibited a higher T_{cc} of 121.0 °C together with reduced ΔH_{cc} (13.3 J/g) and ΔH_m (17.4 J/g) compared with neat PLA (15.8 J/g and 19.1 J/g), implying that CF may provide nucleation sites but can also restrict chain diffusion and limit crystal growth. These effects are reflected in crystallinity: X_c increased modestly with CF but strongly with WF, rising from 20.7% (PLA) to 24.0% (PLA-CF) and 31.1% (PLA-WF) in the first heating, and remaining 20.4% (PLA), 21.8% (PLA-CF), and 31.2% (PLA-WF) in the second heating. PLA-WF shows consistently higher crystalline fraction and slightly higher T_m. In contrast, PLA-CF shows only small crystallinity changes after thermal standardization, indicating that any mechanical differences in PLA-CF are likely governed more by reinforcement efficiency than by crystallinity independently.

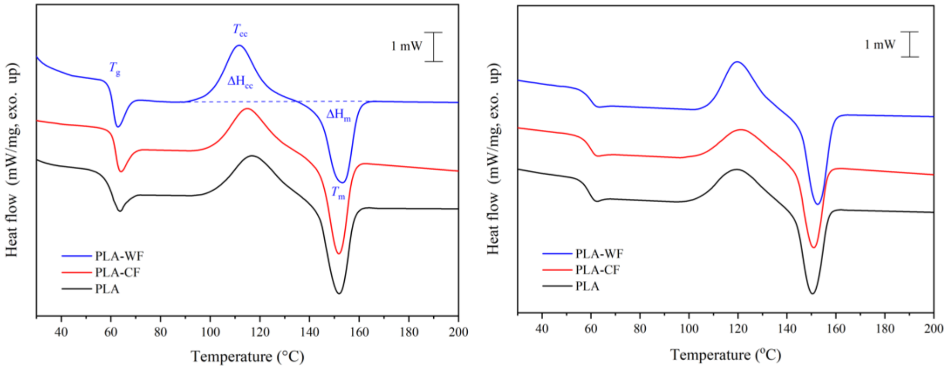

(a) (b)

Fig. 3.10. DSC results: (a) first heating cycle, (b) second heating cycle

Table 3.4. DSC thermal properties

Samples	1st heating						Cooling	2nd heating					
	T_g	T_{cc}	ΔH_{cc}	T_m	ΔH_m	X_c	T_g	T_g	T_{cc}	ΔH_{cc}	T_m	ΔH_m	X_c
	°C		J/g	°C	J/g	%	°C	°C		J/g	°C	J/g	%
PLA	60.8	116.8	18.1	151.9	19.4	20.7	51.2	59.1	119.5	15.8	150.4	19.1	20.4
PLA-CF	61.9	114.9	16.6	151.8	19.1	24.0	50.6	59.9	121	13.3	150.9	17.4	21.8
PLA-WF	61.0	111.7	19.5	153.4	20.4	31.1	49	60.0	119.8	18.9	152.5	20.5	31.2

3.2.3. Viscoelastic behavior and storage modulus

Figure 3.11 shows the DMA thermograms, and Table 3.5 summarizes the analysis results. The DMA storage modulus results (Table 3.5) indicate two distinct thermomechanical regimes: a glassy regime at 30 °C, where the PLA matrix is stiff, and a softened (rubbery) regime at 80 °C, where increased chain mobility results in a pronounced reduction in stiffness.

Figure 3.1 and Table 3.5 show that the storage modulus (E′) decreases by approximately two to three orders of magnitude between 30 °C and 80 °C for all materials.

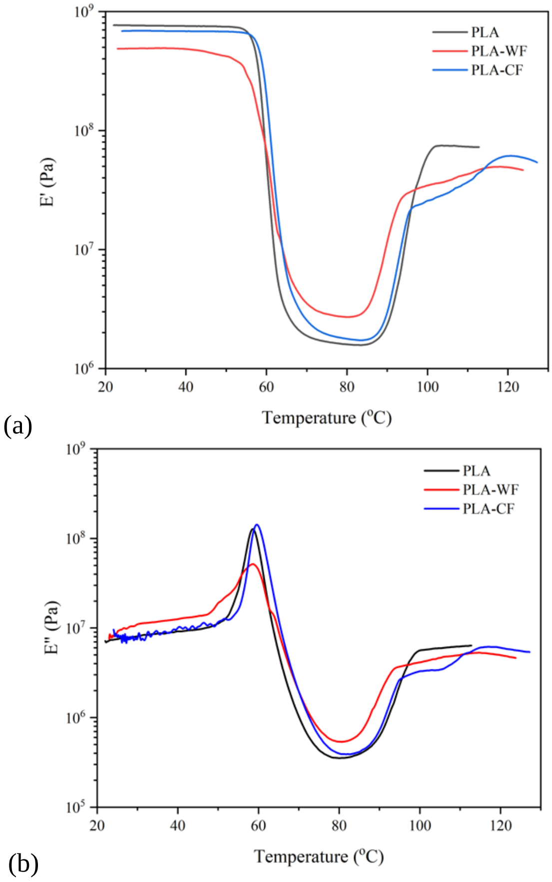

Fig. 3.11. End of figure on the next page

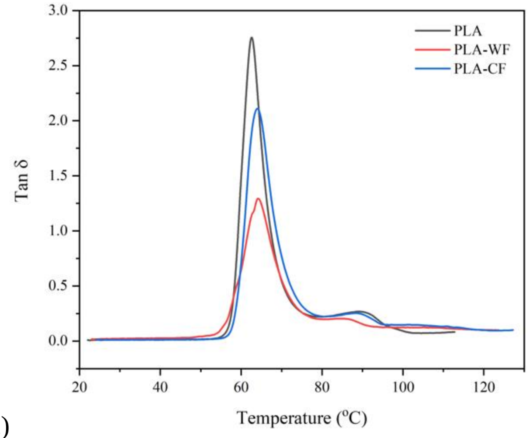

(c)

Fig. 3.11. DMA thermograms: (a) storage modulus; (b) loss modulus; and (c) damping factor

At 30 °C, neat PLA exhibits the highest stiffness (E′ = 761 MPa), followed by PLA-CF (688 MPa) and PLA-WF (490 MPa), suggesting that the glassy response is governed primarily by the matrix and the printed microstructure; any inherent reinforcement benefit is likely moderated by factors such as void content, interfacial load transfer efficiency, and fiber orientation under bending. At 80 °C, the ranking reverses, with PLA-WF retaining the highest modulus (E′ = 2.71 MPa), followed by PLA-CF (1.78 MPa) and PLA (1.60 MPa).

Table 3.5. DMA results: storage modulus comparison

Filament	Storage Modulus @30 °C (MPa)	Storage Modulus @80 °C (MPa)
PLA	761	1.6
PLA-CF	688	1.78
PLA-WF	490	2.71

In terms of modulus retention from 30 °C to 80 °C, PLA retains ≈0.21%, PLA-CF ≈0.26%, and PLA-WF ≈0.55% of the initial stiffness, corresponding to stiffness reductions of ≈476×, ≈387×, and ≈181×, respectively. The superior high-temperature stiffness of PLA-WF is consistent with its higher crystalline fraction, as increased crystallinity and the presence of rigid filler domains impose additional constraints on molecular mobility, thereby improving stiffness retention and thermo-mechanical stability near and above the glass-transition region (Fig. 3.11).

3.2.4. Microstructure analysis

The SEM images of neat PLA (Fig. 3.12a) provide complementary insight into both the internal filament morphology and the fracture behavior of the printed material. Examination of the filament cross-sections at 100× and 500× magnification reveals a relatively dense, uniform internal structure, with a continuous polymer matrix and limited evidence of large voids or inclusions. The cross-sections appear largely homogeneous, indicating stable filament extrusion and consistent material flow during filament production. Occasionally, microvoids and small pores are observed, typical of thermoplastic filaments, and may act as local stress concentrators, but they do not dominate the overall morphology.

The fracture-surface SEM images of neat PLA, observed at comparable magnifications, show a smooth, continuous morphology consistent with matrix-controlled failure. At lower magnification 100×, the fracture surface exhibits limited topographical variation and a largely planar appearance, suggesting relatively uniform stress distribution during loading and a dominant crack path through the polymer matrix and printed raster interfaces. At higher magnification 500× (Fig. 3.13a), localized matrix tearing and shallow deformation features are evident, indicating a brittle-to-semi-ductile fracture response with limited plastic deformation before failure. The absence of fiber pull-out, interfacial gaps, or cracks confirms that fracture in neat PLA proceeds primarily through matrix cracking and interlayer separation rather than through complex energy-dissipating mechanisms. This combination of a homogeneous filament cross-section and a relatively smooth fracture surface is consistent with the mechanical behavior of neat PLA, which exhibits higher tensile and flexural strength than the composite systems but lower toughness, as crack propagation occurs and brittle failure.

Observation of PLA-CF filament cross-sections at 100× and 500× magnification (Fig. 3.12b) reveals short carbon fibers embedded in the PLA matrix, with a generally non-uniform spatial distribution and occasional fiber agglomeration. Localized voids and interfacial gaps are visible around fibers, indicating incomplete wetting and limited interfacial bonding between the carbon fibers and the polymer matrix during fabrication. These microstructural features introduce local stiffness heterogeneities and potential stress concentrators within the filament.

SEM images of the fracture surfaces of printed samples (Figs. 3.13b and 3.14a) show a rough, heterogeneous morphology consistent with the internal structure. At 100× magnification, the fracture surface is non-planar, reflecting non-uniform stress transfer and irregular cracking. At higher magnifications

(500×), frequent fiber pull-out and interfacial debonding are observed, with exposed fiber ends and voids remaining after fiber extraction. Localized matrix deformation and crack deflection around fibers indicate that the presence of carbon fibers promotes energy dissipation during fracture; however, the limited extent of fiber breakage suggests that failure is governed primarily by matrix cracking and interfacial separation rather than by fiber fracture.

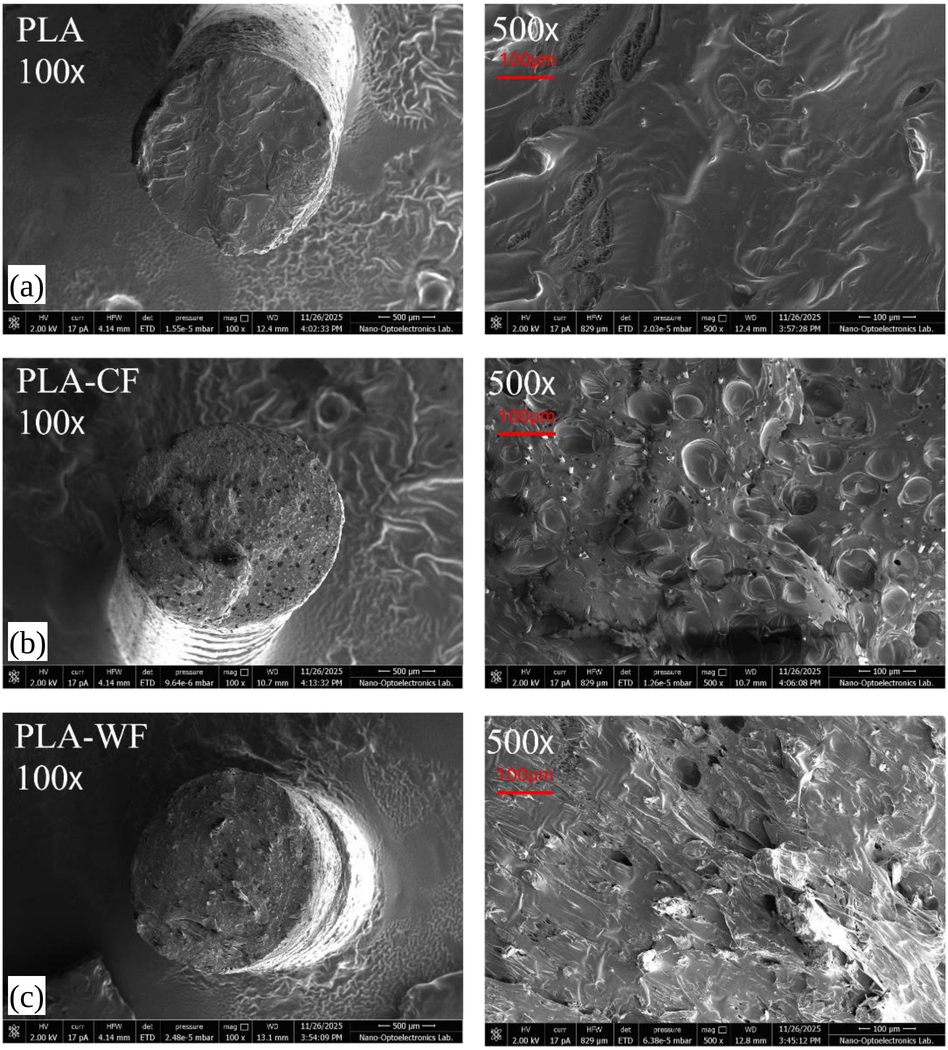

Fig. 3.12. SEM images of the filaments’ cross-section: (a) PLA; (b) PLA-CF; (c) PLA-WF. Note: 100× magnification (left) and 500× magnification (right)

The combined cross-sectional and fracture-surface observations explain the mechanical behavior of PLA-CF: increased stiffness relative to the wood-filled system, but ultimate tensile and flexural strengths remain lower than those of neat PLA due to premature interfacial failure and reduced efficiency of load transfer from the matrix to the short fibers.

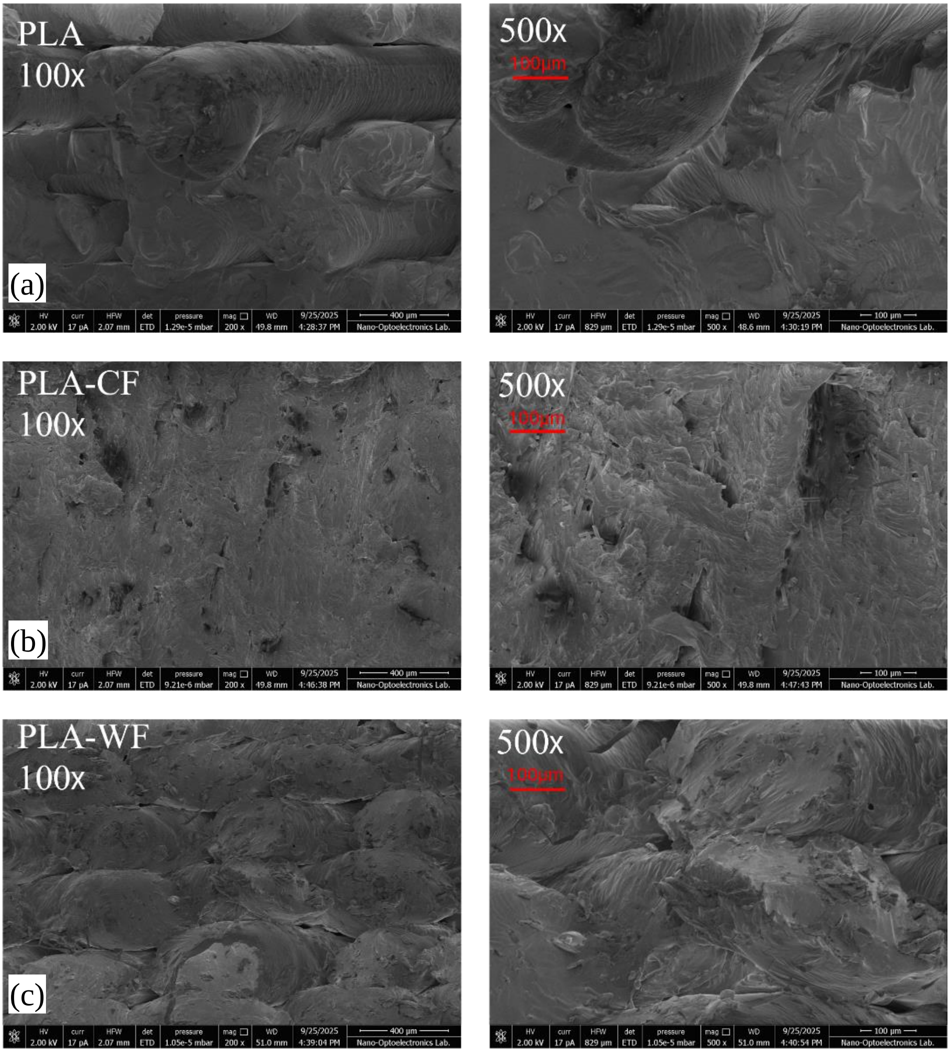

Fig. 3.13. SEM images of fracture surfaces of printed samples: (a) PLA; (b) PLA-CF; (c) PLA-WF. Note: 100× magnification (left) and 500× magnification (right)

For PLA-WF, the SEM images (Fig. 3.12c) of filament cross-sections and fracture surfaces collectively illustrate the strong influence of short wood fibers on microstructural heterogeneity and damage evolution. Examination of the filament cross-sections at 100× and 500× magnifications reveals a non-uniform internal morphology characterized by irregularly distributed short wood fibers within the PLA matrix. Figure 3.12c also shows numerous microvoids, fiber agglomerates, and interfacial gaps surrounding the fibers, indicating incomplete impregnation of the wood fibers by the polymer melt and limited interfacial compatibility. These features cause local changes in stiffness and serve as natural stress concentrators within the filament prepared for FFF.

SEM images of the fracture surfaces of the fabricated samples reveal a heterogeneous internal structure. At a lower magnification of 100× (Fig. 3.13c), the fracture surface appears rough and highly irregular, with multiple crack-initiation sites and pronounced surface undulations, indicating a non-uniform stress distribution during tensile loading. At higher magnification 500× (Figs. 3.13c and 3.14b), extensive fiber pull-out and interfacial debonding are observed, accompanied by elongated cavities left behind after fiber extraction. The surrounding matrix exhibits localized plastic deformation and microvoid coalescence, suggesting that deformation proceeds through progressive damage mechanisms rather than abrupt brittle fracture.

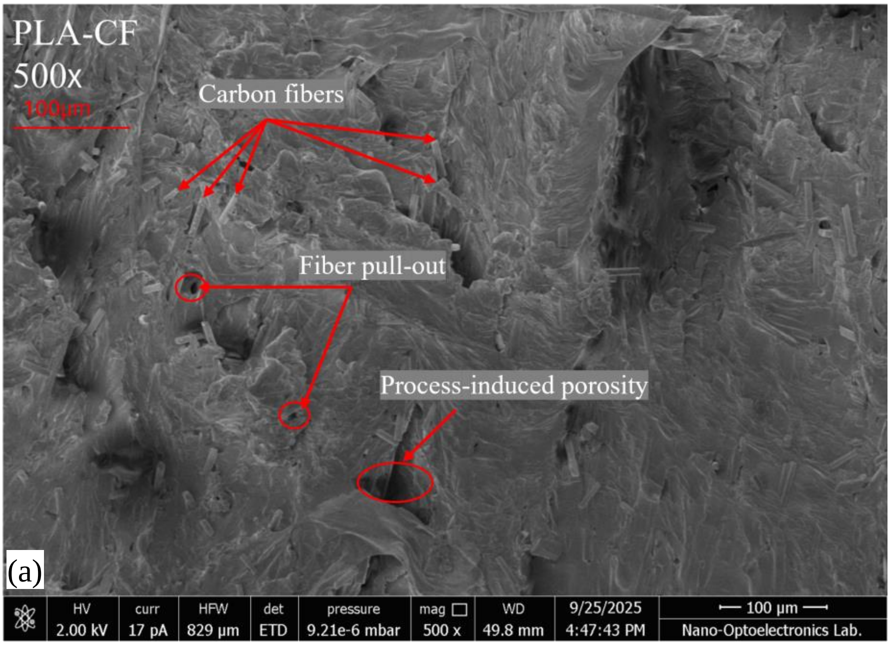

Fig. 3.14. End of figure on the next page

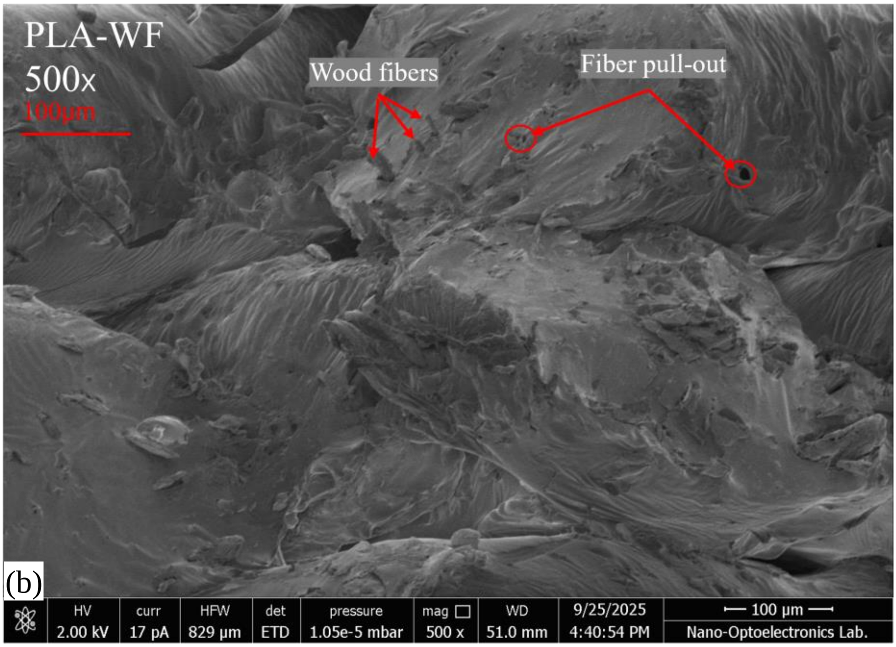

Fig. 3.14. Enlarged SEM images of fracture surfaces of printed samples at 500x magnification: (a) PLA-CF; (b) PLA-WF

Crack distortion and multiple fiber-matrix separation indicate enhanced energy dissipation during fracture. These combined features may explain the mechanical behavior of PLA-WF, which exhibits reduced tensile and flexural strength relative to neat PLA and PLA-CF, but increased strain-to-failure and toughness due to the dominance of progressive damage mechanisms associated with weak fiber-matrix interfaces and heterogeneous microstructure. Figure 3.14a indicates the pull-out of fibers that may limit the toughness of PLA-CF composite (Table 3.2). Figure 3.14b does not show apparent fiber pull-out signs, suggesting fiber fracture as a possible failure mechanism in the PLA-WF composite.

To control the strength of short-fiber FFF composites, the most effective strategies target feedstock conditions, suppress void/neck growth during deposition, and promote interlayer healing. At the pre-processing stage, controlling filament storage humidity and drying is critical because moisture promotes defect formation, such as voids, and property degradation in FFF PLA parts (Lendvai et al., 2024). During printing, the most direct way to reduce printing-pathway-induced internal voids is to calibrate the material flow (extrusion multiplier expressed as a flow rate) to eliminate partial neck-growth voids and increase the effective load-bearing area. Additionally, increasing the extrusion multiplier produced void-free parts and improved in-plane tensile strength by 10% and in-the-build-direction tensile strength by up to 50%, strongly reducing anisotropy (Ghorbani et al., 2022). Typically, parameter optimization (nozzle temperature, speed, layer thickness, raster strategy) helps but is fundamentally constrained by insufficient interface temperature/time for reptation and relaxation. Therefore, in-process localized heating is a high-leverage option: orbiting pre-deposition laser heating increased interlayer temperature and delivered a 100% increase in tensile strength from 17.4 to 34.9 MPa, accompanied by a large increase in strain, in a carbon fiber-reinforced filament (Han et al., 2024). A related in-process laser-heating approach can push FFF parts toward near-isotropic behavior by enabling greater interface relaxation. Applying this approach increased the mechanical strength in the build direction of 3D-printed PEEK from 18.8 MPa to 83.5 MPa (Han et al., 2025). Finally, annealing can relieve residual stresses but often yields only limited direct gains in interlayer strength unless residual-stress effects dominate. In contrast, methods that directly improve intimate contact during deposition, such as mechanical rolling, tend to be more effective for strengthening the printed architecture because they physically close gaps between adjacent pathways and promote better fusion. For instance, roller-assisted consolidation has been reported to reduce void content to about 0.7% by improving contact between adjacent layers (Ghorbani et al., 2022).

3.3. Validation of the thermo-mechanical model

3.3.1. Modeling neat polymer

The following simulations focus on detachment (Fig. 2.5), which affects the deformation and warpage of FFF components under certain fabrication conditions. By explicitly modeling the loss of adhesive contact between the printed part and the build platform, the proposed framework enables a realistic assessment of deformation mechanisms that may arise during and after detachment. This capability is particularly relevant for evaluating the dimensional accuracy and structural integrity of components produced under challenging adhesion scenarios.

Experimental validation was performed using a 0.4-mm-thick specimen. Validation of the FE model involved measuring vertical displacements at 11 predefined locations along the FFF specimen as described in Section 2.7. Figure 3.15a identifies the measurement points for warpage assessment. Figure 3.15b presents the numerical simulation results, and Figure 3.15c compares the experimental and simulated deformation profiles. The results presented correspond to a model comprising 27512 finite elements.

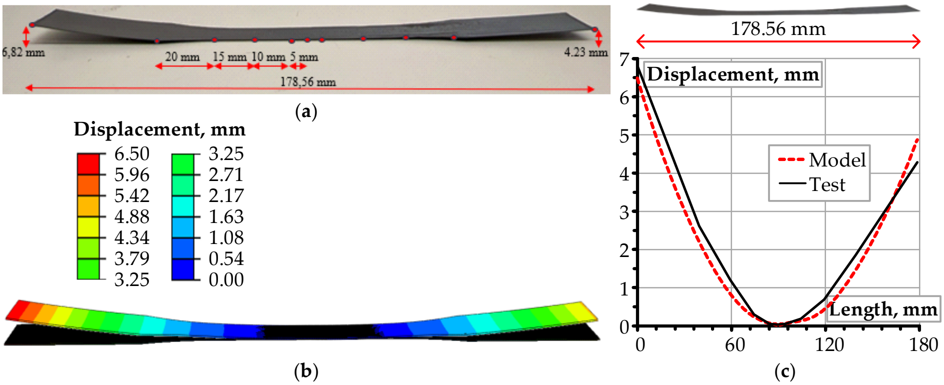

Fig. 3.15. The warpage analysis: (a) experimental measurement points (red circles); (b) FE simulation results; and (c) the comparative analysis of the deformation profiles

Figure 3.16 illustrates the influence of mesh density on the computational efficiency of the warpage simulation. The simulations were performed by varying the number of FE in the model from 9000 to 548720 and the temperature from 200 °C to 220 °C, as described in Section 2.8.4. Within the manufacturer's allowable range, the selected temperatures reflect a practical scenario encountered in desktop FFF. These simulations yielded a 6.7% increase in maximum displacement, underscoring the notable influence of thermal input on deformation behavior. This finding corroborates the conclusions of Liu et al. (2025), who emphasized the critical role of thermal history in determining the final geometry of printed components.

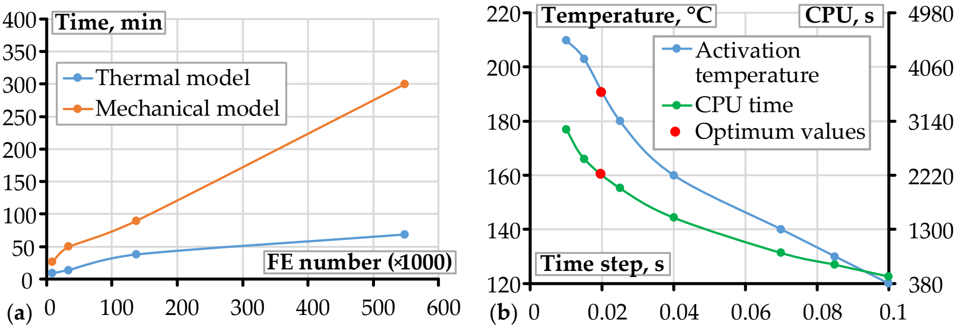

Fig. 3.16. FE mesh optimization: (a) the FE number effect on the simulation duration; (b) the effect of extrusion temperature and assumed time step on the calculation cost

3.3.2. Warpage and residual stress analysis

Residual stresses and warpage remain among the most critical process-induced limitations in FFF, particularly for slender geometries, where thermal gradients, substrate constraints, and non-uniform shrinkage readily generate out-of-plane distortion. Beyond compromising dimensional accuracy and tolerance control, such distortions reflect the presence of locked-in residual stresses that may subsequently relax during handling, detachment, or service, thereby influencing mechanical performance and the reproducibility of failure. The ABAQUS model's ability to replicate experimentally observed warpage patterns confirms its utility for design validation and process optimization of neat PLA parts. The Digimat workflow extends this capability to short-fiber-reinforced composites.

This study develops a staged thermo-mechanical simulation framework that explicitly models the sequential stages of the FFF process: printing, cooling, and detachment. The explicit simulation of the detachment phase distinguishes this framework from previous approaches (Table 1.7), which typically focus solely on the printing and cooling stages. By incorporating the detachment stage, the model enables more realistic predictions of warpage and residual-stress release, as confirmed by experimental validation. Using this framework, the developed thermo-mechanical model (Fig. 2.6) enables efficient prediction of warpage behavior in PLA specimens fabricated via the FFF process. The simulation results indicate that residual stresses were negligible during the printing phase but increased significantly during cooling due to thermal contraction and substrate constraints. Upon detachment, the release of these constraints caused a sudden relaxation of residual stresses, leading to observable warping, predominantly at the specimen edges. This observation underscores the importance of explicitly modeling detachment within the simulation framework, as it is critical for capturing the dominant deformation mechanisms and failure risks arising from the loss of adhesive contact between the printed part and the build platform.

The experimentally measured maximum vertical displacement was 6.82 mm, which aligns closely with the simulation results. The average deviation between the numerical and experimental results was approximately 10.6%, indicating that the model has adequate predictive capability. This level of agreement aligns with findings from Cattenone et al. (2019) and Armillotta et al. (2018), who reported a 12% dimensional deviation in similar simulations involving ABS materials. Syrlybayev et al. (2021) and Barocio et al. (2020) reported comparable simulation errors ranging from 8% to 15%, depending on geometric complexity and applied thermal boundary conditions. In this context, the 10.6% deviation observed in the present study falls within the typical range reported for thermo-mechanical simulations of FFF processes, confirming the model's capability to capture the dominant deformation mechanisms. The agreement between simulated and experimental warpage profiles demonstrates the adequacy of the staged simulation approach, particularly the inclusion of a detachment phase to capture the dominant deformation mechanisms in FFF-fabricated components.

This study extends the understanding of warpage behavior in PLA materials by highlighting the critical roles of thermal contraction and constraint release. This insight is particularly relevant for optimizing the FFF process to minimize warpage and improve part quality. The findings also underscore the importance of thermal modeling in predicting residual stresses and deformation patterns. Automatically generating event series from G-code enhances the versatility of simulations. It reduces manual intervention, avoiding the errors characteristic of manual model updates and thereby speeding up the simulation process.

3.3.3. Convergence and sensitivity studies

A convergence study balances the mesh resolution and time-stepping parameters. The results indicated that using one element per filament cross-section yielded sufficient accuracy, with predicted warpage varying by less than 2.1% across mesh densities. Similarly, time steps of 0.01 s during printing and 0.1 s during cooling and detachment were found to strike a balance between computational efficiency and predictive fidelity. These findings align with recommendations by Syrlybayev et al. (2021), Barocio et al. (2020), and Brenken et al. (2019), who emphasized the importance of mesh refinement and time-step control in capturing localized thermal and mechanical gradients. The extrusion temperature also significantly influenced warpage. Increasing the extrusion temperature from 200 °C to 220 °C increased the maximum displacement by 6.7%, highlighting the warpage's sensitivity to extrusion temperature. This observation supports the conclusions of Liu et al. (2025), who highlighted the role of thermal history in determining final part geometry.

The sensitivity analysis (Fig. 3.16) shows that computational time, for both thermal and mechanical analyses, increases linearly with the number of finite elements. While refining the mesh improves the accuracy of the stress-gradient model, especially when the mesh resolution closely matches filament dimensions, it substantially increases computational cost. Therefore, to obtain sufficiently accurate results, it is recommended to use one element per filament's cross-section and a 0.02 s time step (Δt) for efficient computation, which corresponds to 2220 s CPU time and activation temperature of 192 °C, as shown in Figure 3.15b.

At the same time, developing an appropriate meshing strategy is complex and must be customized to the specific needs of the analysis. While a refined mesh improves the accuracy of stress gradient predictions, it also significantly increases computational costs. This contradiction is apparent in mechanical analyses, where stress concentrations raise the system's sensitivity to mesh refinement. Thus, the increase in accuracy (Fig. 3.16b) does not appear to converge as the number of elements grows, which may result from local stress singularities or the continued rise in stress with mesh refinement, ensuring that the stress state remains within or on the yield surface, depending on the magnitude of the equivalent stress. Uniformly refining the mesh without targeted focus on critical stress regions is also inefficient and raises computational time. In some cases, nonlinear material behavior can also influence this trend (L. Chen & Zhou, 2025; van Huyssteen et al., 2025). Therefore, for smaller models with significant local stress effects and manageable computational costs, a finer mesh is advisable to capture localized mechanical responses. Conversely, for larger models where local variations are less significant relative to the overall geometry, a coarser mesh is generally more suitable for reducing computational demands while maintaining acceptable accuracy. Future research should examine the effects of other process parameters, such as print speed and layer height, on warpage and residual stresses. Furthermore, investigating parameter interactions could yield a more comprehensive understanding of the FFF process and its influence on part quality.

3.3.4. Warpage predictions of short-fiber-reinforced polymers

Within the Digimat-AM workflow, an ASTM D638 Type I geometry was generated as an STL file and sliced in Ultimaker Cura to produce the G-code. Slicing was performed at 100% infill using a ±45° raster pattern, with the infill angle alternated between layers, a print speed of 30 mm/s, and an extrusion temperature of 215 °C. The thickness of the first layer was set to 0.2 mm and subsequent layers to 0.3 mm, resulting in a specimen thickness of approximately 3.2 mm. The homogenized composite material model (from Digimat-MF) and the manufacturing inputs (CAD and G-code/toolpath data) were then imported into Digimat-AM to simulate deposition, cooling, and distortion at reduced computational cost.

Digimat-AM differs from ABAQUS meshing in that it typically uses a voxel-based discretization, where the part domain is represented on a structured grid mapped to brick-like FE. This voxel approach simplifies automated toolpath mapping and enables robust process simulations for complex deposition paths. However, local gradient capture is primarily controlled by voxel size rather than by targeted mesh refinement. In contrast, ABAQUS uses geometry-conforming meshes (structured, tetrahedral, or hexahedral) with selective refinement in regions of high gradients, which is advantageous for detailed residual-stress fields and localized deformation analysis. Model validation of the Digimat-AM warpage simulation was performed by direct comparison with the experimentally measured edge warpage for the three printed materials. The test measurements show a reduction in edge warpage with short-fiber reinforcement, decreasing from 0.49 mm for neat PLA to 0.42 mm for PLA-CF and 0.28 mm for PLA-WF, confirming improved dimensional fidelity during cooling. Digimat-AM simulated both the trend and the location of maximum distortion, predicting a monotonic reduction in the maximum warpage, with the highest deformation concentrated at the specimen edge, where constraint release and thermal contraction effects are most pronounced. Quantitatively, the numerical predictions systematically underestimate the measured warpage for PLA, PLA-CF, and PLA-WF, corresponding to relative deviations of approximately 8.2%, 14.3%, and 17.9%, respectively (Fig. 3.17).

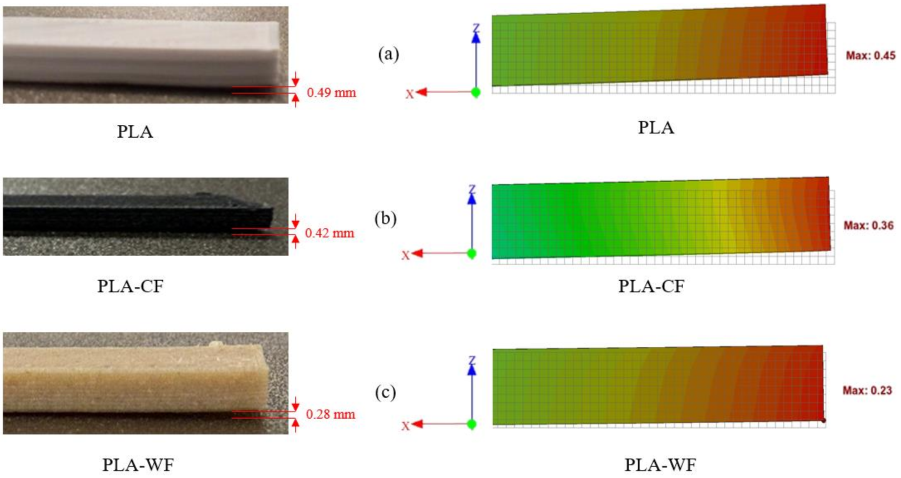

Fig. 3.17. Digimat-AM warpage predictions for short-fiber-reinforced PLA

Despite differences in the magnitudes of measured and simulated deformations (Fig. 3.17), the close agreement in ranking and deformation patterns indicates that the Digimat-AM workflow captures the dominant thermo-mechanical drivers of edge warpage and provides a practical predictive tool for comparing material-dependent distortion and guiding process-level decisions where dimensional accuracy is critical.

3.3.5. Residual stress effect on mechanical performance

The proposed thermo-mechanical model predicted the residual stresses for the test specimen (Fig. 3.18). The temperature history is introduced as a solution-independent boundary condition into the mechanical model to estimate the residual stresses and part deformations generated within the 3D-printed specimen by thermal cycling, cooling, and process constraints. Higher residual stresses were observed along the specimen edges than at other locations.

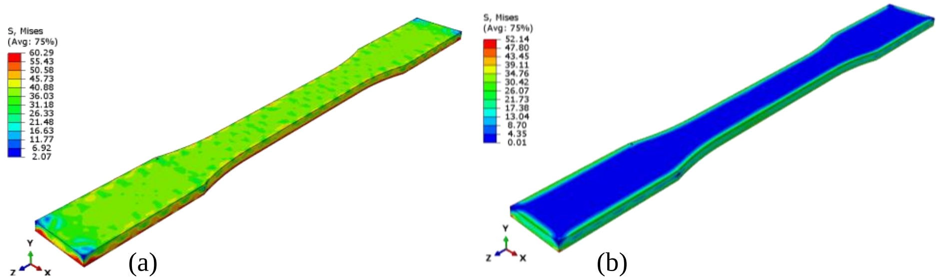

Fig. 3.18. Simulation results: (a) residual stresses of test specimen at the end of extrusion; (b) at the end of cooling, where S is the stress (MPa)

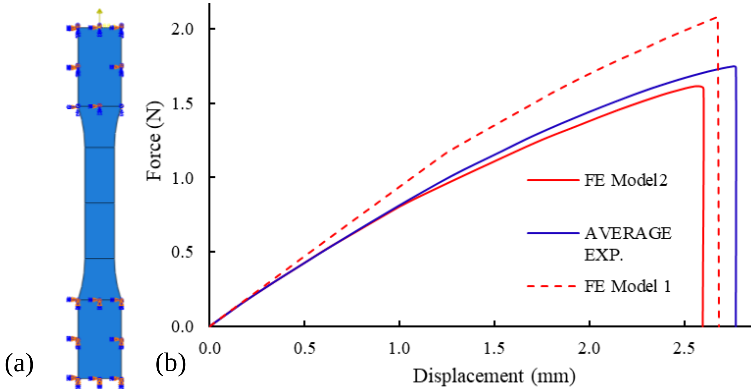

Fig. 3.19. Simulation results: (a) tensile test model; (b) load-displacement diagrams. Note: FE Model 1 and FE Model 2 correspond to the first and second simulation stages

A subsequent tensile test simulation was conducted after the thermo-mechanical analysis. The first tensile test simulation was performed, excluding manufacturing defects in the FFF process. The second tensile test model includes residual stresses and geometry distortion. The latter model indicates the impact of residual stresses on the mechanical performance of the 3D-printed components, and the results were validated through physical testing, achieving acceptable accuracy (Fig. 3.19). The average force-displacement results reported by Rimkus et al. (2022) were used to validate the FE model. The physical test demonstrated tensile load-bearing capacity of 1.7 kN at a displacement of 2.8 mm. The first tensile test model yielded higher predictions than the physical test; however, the second model showed a reduction in tensile load-bearing capacity due to the incorporation of residual stresses and geometric deformation of the test specimen.

3.3.6. Comparison with previous studies, limitations of the model, and further research

The proposed model builds upon and advances earlier work by Zhang and Chou (2006), who introduced the element birth-and-death method for simulating residual stresses in ABS components. Unlike those studies, the proposed staged modeling strategy, which sequentially simulates printing, cooling, and detachment, enables a more comprehensive assessment of residual-stress evolution and warpage than approaches limited to printing or cooling alone. This innovation directly incorporates slicing parameters and toolpath data into the FE model and simulates the post-printing stage, thereby enhancing the fidelity of numerical predictions. In terms of geometric complexity, previous studies, such as those by Syrlybayev et al. (2021) and Armillotta et al. (2018), primarily addressed simplified geometries with manually defined activation sequences. The current workflow (Fig. 2.6) demonstrates the feasibility of automating the simulation of complex deposition paths. This advancement is particularly relevant for engineering applications requiring high geometric accuracy and structural integrity.

Regarding prediction accuracy, the current models achieve an average warpage deviation of 10.6% and 8.2% of the neat PLA for ABAQUS and Digimat models, respectively, which is comparable to the 12% deviation reported by Armillotta et al. (2018) and the 9.5% error observed in multi-material simulations by Syrlybayev et al. (2021). Recent studies, such as those by Yu et al. (2025), also demonstrate strong agreement between simulation and experiment, particularly when considering infill line directions and their impact on mechanical properties. These comparisons confirm that the model performs within the expected accuracy range for thermo-mechanical FFF simulations.

For short-fiber composites, Digimat-AM warpage predictions systematically underestimated PLA-CF and PLA-WF by approximately 14.3% and 17.9%, respectively. The larger deviations in the composites also suggest that the sensitivity analysis should be extended to the Digimat workflow, as warpage predictions are highly sensitive to assumptions in composite material modeling, including temperature-dependent material properties, fiber orientation, porosity, and thermal boundary conditions.

The thermal modeling strategy is crucial for capturing the transient heat-transfer mechanisms that lead to residual stress and warpage. By differentiating among conduction, convection, and radiation effects at each stage of the FFF process, including the critical detachment phase, the model accounts for the evolving thermal boundary conditions governing residual stress formation and warpage. This level of detail is often simplified or omitted in the literature (Cattenone et al., 2019; Khanafer et al., 2022), improving the accuracy of predicted temperature fields and, consequently, the mechanical response of the printed part. The explicit simulation of the detachment stage in the staged approach enables analysis of unsupported regions, where warpage is most pronounced, and failure risk is highest.

Despite these strengths, the model has several limitations. The proposed modeling concept assumes the deposited layer thickness is known and constant, as this parameter directly determines the height of the corresponding finite elements in the simulation. While this assumption is reasonable for relatively thin or simple geometries, it may become inadequate as the height and complexity of FFF structures increase. Therefore, further experimental investigations are essential to validate the accuracy of this simplification, particularly for tall or intricate printed components.

Additionally, the current model does not account for viscoelastic or time-dependent material behavior, which can be particularly significant for polymers near their glass transition temperature (Slavković et al., 2024). Additionally, the current implementation assumes isotropic material properties and does not account for variability in interlayer bonding or environmental factors, such as humidity. Future research should aim to address these limitations by incorporating more advanced material models, including temperature-dependent viscoelasticity and anisotropy, to improve simulation fidelity and deepen understanding of deformation mechanisms. The integration of machine learning (ML) techniques also presents a promising direction. ML models trained on simulation and experimental datasets could facilitate rapid prediction of warpage and residual stress for new geometries and process parameters, significantly reducing computational costs. Furthermore, coupling ML with topology optimization could enable the design of structurally optimized, distortion-resistant components.

3.4. Conclusions of the Third Chapter

1. *Continuous-fiber reinforcement and sustainable manufacturing*. Continuous-fiber reinforcement developed and investigated in this study within the FFF framework reveals fundamental methodological and technological limitations governing its achievable performance under conventional printing conditions. The proposed reinforcement route follows a duplicated manufacturing sequence, in which aramid yarn is first integrated into the PLA filament during extrusion and subsequently processed during 3D printing. This two-stage workflow leads to the accumulation of defects arising from both filament production and printing, in contrast to reinforcement concepts that rely on in-situ polymer consolidation during material deposition. As a result, limitations related to constituent compatibility, composite solidification, fiber alignment, and the lack of in-process fiber tensioning constrain the effective use of continuous reinforcement in typical single-extruder FFF systems. At the same time, the standardized geometry of the

developed reinforced filament enables FFF on minimally customized desktop printers, demonstrating that continuous reinforcement can be made accessible on widely available FFF equipment, albeit with clearly defined efficiency limits.

The mechanical response of the investigated specimens establishes printing-pathway configuration as a governing parameter for load-bearing capacity: when the printing layout is aligned with the principal tensile stress direction, the measured load-bearing capacity of PLA specimens increases by approximately a factor of two relative to nominal manufacturer-reported material parameters, indicating that pathway-controlled stress transfer can substantially amplify structural performance without changing material composition. This finding identifies printing-pathway design as a first-order design variable for FFF components. It provides a rational basis for strength enhancement through geometry-aware manufacturing strategies rather than material over-engineering. Finite-element analysis calibrated against experimental results quantifies the efficiency of the developed continuous reinforcement, yielding effective values of 6.8% in stiffness and 13.6% in load-bearing capacity, which remain substantially below theoretical expectations. In parallel, physical testing shows that the reinforced specimens exhibit increased deformation capacity, with the experimentally observed deformation at maximum resistance exceeding numerical predictions by a factor of 1.35, demonstrating that the developed system promotes ductility and energy absorption that are not captured by idealized reinforcement models and must be considered in performance-based design.

From a sustainability and resource-efficiency perspective, this dissertational work confirms that partial substitution of neat PLA with recycled material is compatible with both unreinforced and reinforced FFF processing and does not compromise mechanical performance. Incorporation of 40% recycled PLA maintained tensile resistance while reducing material costs by nearly 50%, directly improving the economic feasibility of reinforced FFF. In addition, the recycled-content material exhibited improved repeatability of results, with the coefficient of variation in tensile strength decreasing from 5.0% to 1.2%, indicating enhanced process stability. These results establish recycled-content PLA not merely as an environmentally acceptable alternative, but as a technically advantageous feedstock for reinforced FFF, providing a quantitative foundation for integrating sustainability and mechanical reliability in additive manufacturing design.

2. *Short-fiber reinforcement mechanisms and thermo-mechanical properties.* Short-fiber reinforcement investigated in this study modifies the mechanical response of FFF-printed PLA components by shifting performance from maximum strength toward enhanced damage tolerance and dimensional fidelity. Under identical FFF conditions, both carbon-fiber-reinforced (PLA-CF) and wood-fiber-reinforced (PLA-WF) filaments exhibit lower tensile and flexural strengths than

neat PLA, confirming that short-fiber addition does not translate into net strengthening in the printed state. At 100% infill, neat PLA achieves the highest tensile strength (39.9 MPa) and flexural strength (45.9 MPa), whereas PLA-CF and PLA-WF reach reduced tensile strengths of 27.2 MPa and 24.1 MPa, and flexural strengths of 38.6 MPa and 31.4 MPa. These results demonstrate that the efficiency of short-fiber reinforcement in FFF is primarily constrained by interfacial integrity and defect sensitivity rather than by the intrinsic stiffness of the fibers themselves.

Despite reduced ultimate strength, short-fiber-reinforced systems exhibit a pronounced increase in ductility and energy-absorption capacity, particularly for wood-fiber-filled PLA. At full infill, tensile toughness increases from 813 kJ/m^3 for neat PLA to 985 kJ/m^3 for PLA-CF and 1268 kJ/m^3 for PLA-WF, while PLA-WF also attains the highest strain-to-failure (5.6%). This transition from a relatively abrupt matrix-dominated fracture toward progressive damage development is supported by microstructural evidence, reflecting the activation of crack deflection, micro-void formation, and fiber pull-out mechanisms. Consequently, short-fiber reinforcement enables improved damage tolerance and deformation capacity, making these materials suitable for applications where controlled failure and energy dissipation are prioritized over peak load-bearing capacity.

Thermal and viscoelastic characterization establishes a direct link between fiber type, crystallization behavior, and thermo-mechanical stability. Differential scanning calorimetry shows that the glass-transition temperature remains close to 60 °C for all materials. At the same time, PLA-WF exhibits consistently higher crystallinity (31%) and a slightly elevated melting temperature compared with neat PLA and PLA-CF (20–22% crystallinity). Dynamic mechanical analysis further reveals that PLA-WF retains the highest storage modulus at 80 °C (2.7 MPa), compared with 1.78 MPa for PLA-CF and 1.60 MPa for neat PLA, indicating superior resistance to thermal softening near and above the glass-transition region. These thermo-mechanical advantages translate directly into improved dimensional fidelity during cooling, as evidenced by reductions in edge warpage of 14.3% for 10 wt% carbon fiber and 43% for 30 wt% wood fiber relative to neat PLA. Together, these findings establish short-fiber reinforcement (particularly wood-fiber-filled PLA) as an effective strategy for enhancing dimensional fidelity and damage tolerance in FFF components, providing clear guidance for material selection when geometric accuracy and thermo-mechanical robustness govern design requirements.

3. *Computational process simulation and predictive modeling.* The staged thermo-mechanical simulation framework developed and validated in this study enables process-aware prediction of deformation mechanisms in FFF-printed polymeric components. The proposed modeling strategy explicitly incorporates the sequential stages of printing, cooling, and detachment from the build platform,

allowing residual-stress accumulation and release to be traced throughout the entire fabrication process. An automated procedure for converting slicer-generated G-code into a time-resolved event series enables progressive element activation in FE simulations, directly linking the fabrication toolpath with the numerical model. This approach eliminates manual intervention in model preparation and establishes a reproducible simulation workflow directly linked to realistic manufacturing conditions.

Coupling transient thermal analysis with mechanical simulation provides a quantitative prediction of residual stresses and warpage driven by thermal contraction and constraint release. For neat PLA, the ABAQUS-based framework predicts warpage with an average deviation of 10.6% relative to experimental measurements, which lies within the accuracy range reported for thermo-mechanical FFF simulations. Extension of the framework to short-fiber-reinforced composites through Digimat-based homogenized material modeling captures the experimentally observed material-dependent ranking of warpage. It reproduces the edge-dominated distortion mode characteristic of FFF components. Validation against measured edge warpage shows systematic underestimation for PLA, PLA-CF, and PLA-WF, with relative deviations of approximately 8.2%, 14.3%, and 17.9%, confirming that the model reliably captures trends and deformation mechanisms while highlighting the sensitivity of composite predictions to microstructural assumptions.

Integrating the thermo-mechanical solution into subsequent mechanical simulations demonstrates the direct influence of manufacturing-induced residual stresses and geometric distortion on structural performance. When residual stresses and as-printed geometry are introduced into tensile simulations, the predicted load-bearing capacity decreases relative to idealized models that neglect manufacturing effects, and the resulting response shows acceptable agreement with physical tensile testing. This manufacturing-informed assessment establishes that predicting mechanical performance in FFF components requires explicit consideration of process-induced fields rather than relying solely on nominal material properties. Sensitivity analyses further confirm the dominant influence of extrusion temperature, mesh resolution, and time-step selection on prediction accuracy, leading to a practical meshing guideline recommending approximately one finite element per filament cross-section for efficient and reliable simulations. The developed modeling framework provides a quantitative tool to reduce trial-and-error in FFF by enabling the pre-selection of materials, process parameters, and dimensional-tolerance strategies through predictive FE simulations.

General Conclusions

The dissertation explores the relationship between the FFF process, composition, and material properties in PLA-based fiber-reinforced composites. The results indicate that the advantages of fiber reinforcement depend on specific conditions: continuous aramid reinforcement boosts tensile resistance but is constrained by routing and consolidation, whereas short fibers enhance damage tolerance, stiffness retention, and dimensional stability, with ultimate strength influenced by interfacial integrity and internal discontinuities. The proposed modeling workflow provides a tool for predicting geometric distortion and residual stresses, aiding material selection and FFF process optimization when precise geometric accuracy is essential. In practice, the achieved strength-to-weight improvements and the manufacturability on standard equipment indicate immediate relevance for lightweight functional parts such as drone components, small-vehicle/robotic elements, and secondary transportation structures where mass reduction is a governing requirement. The investigation concludes with the following general findings:

1. Continuous reinforcement layup faces severe limitations related to constituent compatibility, composite solidification, fiber alignment, and stretching. The FFF process demonstrates the consequence of duplicate production: aramid yarn reinforcement occurs during filament extrusion, followed by part fabrication during printing; defects from both stages accumulate. The novelty lies in demonstrating a pre-impregnated aramid–

PLA filament that is printable on an ordinary single-extruder FFF system and in quantifying reinforcement efficiency against a theoretical FE reference, approximately 6.8% in stiffness and 13.6% in load-bearing capacity, while identifying process causes (absence of in-process fiber tensioning, routing-driven geometric inaccuracy, and interface defects).

2. The integrated SEM, DSC, DMA, and mechanical characterization reveals fiber-type-specific linkages between the material characteristics and content under identical FFF conditions: wood fiber (30 wt%) increases crystallinity and toughness and reduces edge warpage by 43%, whereas carbon fiber (10 wt%) reduces warpage by 14.3% and raises stiffness with strength governed by interface-controlled defects, thus extending prior literature beyond single-metric comparisons. In practice, these findings provide selection guidance: wood fibers, where dimensional fidelity and damage tolerance dominate, and carbon fibers, where stiffness gains are prioritized, and tolerances remain manageable.
3. Scientifically, the developed staged finite-element framework, driven by the custom-made G-code-based element activation and including printing, cooling, and explicit detachment, advances prior FFF models by automatically transferring fabrication process-induced residual-stress and distortion fields into subsequent mechanical simulation. The warpage predictions show good agreement with the experiments, with an average deviation of 10.6%. A Digimat workflow extends modeling to short-fiber-reinforced composites by using RVE-based homogenization, capturing for the first time material-dependent distortion ranking, and accounting for an edge-dominated warpage mode. In practice, this modeling approach reduces trial-and-error by enabling the pre-selection of materials and dimensional-tolerance parameters.

References

Abouzaid, K., Bassir, D., Guessasma, S., & Yue, H. (2021). Modelling the process of fused deposition modelling and the effect of temperature on the mechanical, roughness, and porosity properties of resulting composite products. *Mechanics of Composite Materials, 56*(6), 805–816. https://doi.org/10.1007/s11029-021-09925-6

Abtew, M. A., Boussu, F., Bruniaux, P., & Liu, H. (2020). Fabrication and mechanical characterization of dry three-dimensional warp interlock para-aramid woven fabrics: Experimental methods toward applications in composite reinforcement and soft body armor. *Materials, 13*(19), 4233. https://doi.org/10.3390/ma13194233

Abusrea, M., Shazly, M., Terutake, M., Wen-Xue, W., & Arakawa, K. (2023). Strength enhancement of CFRP joints composed of partially unmolded laminates manufactured using Vacuum-Assisted Resin Transfer Molding (VARTM). *The Journal of Adhesion, 99*(3), 379–405. https://doi.org/10.1080/00218464.2021.2020112

Ainali, N. M., Bikiaris, D. N., & Lambropoulou, D. A. (2021). Aging effects on low-and high-density polyethylene, polypropylene and polystyrene under UV irradiation: An insight into decomposition mechanism by Py-GC/MS for microplastic analysis. *Journal of Analytical and Applied Pyrolysis, 158,* 105207. https://doi.org/10.1016/j.jaap.2021.105207

Akbari, S., Sakhaei, A. H., Kowsari, K., Yang, B., Serjouei, A., Yuanfang, Z., & Ge, Q. (2018). Enhanced multimaterial 4D printing with active hinges. *Smart Materials and Structures, 27*(6), 065027. https://doi.org/10.1088/1361-665X/aabe63

Al Rashid, A., & Koç, M. (2023). Experimental validation of numerical model for thermomechanical performance of material extrusion additive manufacturing process: Effect of infill design & density. *Results in Engineering, 17*, 100860. https://doi.org/10.1016/j.rineng.2022.100860

Ali, S. S., Abdelkarim, E. A., Elsamahy, T., Al-Tohamy, R., Li, F., Kornaros, M., . . . Sun, J. (2023). Bioplastic production in terms of life cycle assessment: A state-of-the-art review. *Environmental Science and Ecotechnology, 15*, 100254. https://doi.org/10.1016/j.ese.2023.100254

Amar, T. A., Kumar, A., & Yadav, D. (2025). A comparative study on the properties of carbon fiber-reinforced polymer composites developed by hand layup and vacuum bagging molding techniques. *Journal of The Institution of Engineers (India): Series D, 106*(1), 263–275. https://doi.org/10.1007/s40033-023-00631-2

Anderson, I. (2017). Mechanical properties of specimens 3D printed with virgin and recycled polylactic acid. *3D Printing and Additive Manufacturing, 4*(2), 110–115. https://doi.org/10.1089/3dp.2016.0054

Araya-Calvo, M., López-Gómez, I., Chamberlain-Simon, N., León-Salazar, J. L., Guillén-Girón, T., Corrales-Cordero, J. S., & Sánchez-Brenes, O. (2018). Evaluation of compressive and flexural properties of continuous fiber fabrication additive manufacturing technology. *Additive Manufacturing, 22*, 157–164. https://doi.org/10.1016/j.addma.2018.05.007

ASTM International (2006). *Standard test methods for determining the Izod pendulum impact resistance of plastics* (*ASTM D256-06*). https://doi.org/10.1520/D0256-06

ASTM International (2007). *Standard test method for flexural properties of polymer matrix composite materials (ASTM D7264/D7264M-07).* https://doi.org/10.1520/D7264_D7264M-07

ASTM International (2010a). *Standard test method for flexural properties of unreinforced and reinforced plastics and electrical insulating materials (ASTM D790-10).* https://doi.org/10.1520/D0790-10

ASTM International (2010b). *Standard test method for tensile properties of plastics (ASTM D638-10).* https://doi.org/10.1520/D0638-10

ASTM International (2013). *Standard test method for in-plane shear response of polymer matrix composite materials by tensile test of a ±45° laminate (ASTM D3518/D3518M-13).* https://doi.org/10.1520/D3518_D3518M-13

ASTM International (2014a). *Standard test method for tensile properties of plastics (ASTM D638-14)*. https://doi.org/10.1520/D0638-14

ASTM International (2014b). *Standard test method for tensile properties of polymer matrix composite materials* (*ASTM D3039/D3039M-14*). https://doi.org/10.1520/D3039_D3039M-14

ASTM International (2017). *Standard test method for tensile properties of polymer matrix composite materials (ASTM D3039/D3039M-17)*. https://doi.org/10.1520/D3039_D3039M-17

ASTM International (2018). *Standard test method for determining the Charpy V-notch impact resistance of plastics (ASTM D6110-18)*. https://doi.org/10.1520/D6110-18

Babagowda, Kadadevara Math, R., Goutham, R., & Srinivas Prasad, K. (2018). Study of effects on mechanical properties of PLA filament which is blended with recycled PLA materials. *IOP Conference Series: Materials Science and Engineering, 310*, 012103. https://doi.org/10.1088/1757-899X/310/1/012103

Banjanin, B., Vladić, G., Pál, M., Dimovski, V., Adamović, S., & Delić, G. (2018). Production factors influencing mechanical and physical properties of FDM printed embossing dies. In *Proceedings of the 9th International Symposium on Graphic Engineering and Design*. https://doi.org/10.24867/GRID-2018-p28

Banupriya, R., Jeevan, T., Divya, H., Yashas Gowda, T., & Manjunath, G. (2025). 3D-printed graphene-reinforced composites: Opportunities and challenges. *Polymer Composites, 46*(2), 1250–1266. https://doi.org/10.1002/pc.29068

Bastola, A. K., Paudel, M., & Li, L. (2018). Development of hybrid magnetorheological elastomers by 3D printing. *Polymer, 149*, 213–228. https://doi.org/10.1016/j.polymer.2018.06.076

Behseresht, S., Park, Y. H., Love, A., & Valdez Pastrana, O. A. (2024). Application of numerical modeling and finite element analysis in fused filament fabrication: A review. *Materials, 17*(17), 4185. https://doi.org/10.3390/ma17174185

Berman, B. (2012). 3-D printing: The new industrial revolution. *Business horizons, 55*(2), 155–162. https://doi.org/10.1016/j.bushor.2011.11.003

Bettini, P., Alitta, G., Sala, G., & Di Landro, L. (2017). Fused deposition technique for continuous fiber reinforced thermoplastic. *Journal of Materials Engineering and Performance, 26*(2), 843–848. https://doi.org/10.1007/s11665-016-2459-8

Bhandari, S., Lopez-Anido, R. A., & Gardner, D. J. (2019). Enhancing the interlayer tensile strength of 3D printed short carbon fiber reinforced PETG and PLA composites via annealing. *Additive Manufacturing, 30,* 100922. https://doi.org/10.1016/j.addma.2019.100922

Bhawal, P., Ganguly, S., Chaki, T., & Das, N. (2016). Synthesis and characterization of graphene oxide filled ethylene methyl acrylate hybrid nanocomposites. *RSC advances, 6*(25), 20781–20790. https://doi.org/10.1039/C5RA24914G

Bher, A., Mayekar, P. C., Auras, R. A., & Schvezov, C. E. (2022). Biodegradation of biodegradable polymers in mesophilic aerobic environments. *International Journal of Molecular Sciences, 23*(20), 12165. https://doi.org/10.3390/ijms232012165

Blanco, D., Fernández, P., & Noriega, A. (2014). Nonisotropic experimental characterization of the relaxation modulus for PolyJet manufactured parts. *Journal of Materials Research, 29*(17), 1876–1882. https://doi.org/10.1557/jmr.2014.200

Blok, L. G., Longana, M. L., Yu, H., & Woods, B. K. (2018). An investigation into 3D printing of fibre reinforced thermoplastic composites. *Additive Manufacturing, 22,* 176–186. https://doi.org/10.1016/j.addma.2018.04.039

Bodaghi, M., Sadooghi, A., Bakhshi, M., Hashemi, S. J., Rahmani, K., & Keshavarz Motamedi, M. (2023). Glass fiber reinforced acrylonitrile butadiene styrene composite gears by FDM 3D printing. *Advanced Materials Interfaces, 10*(27), 2300337. https://doi.org/10.1002/admi.202300337

Brenken, B., Barocio, E., Favaloro, A., Kunc, V., & Pipes, R. B. (2018). Fused filament fabrication of fiber-reinforced polymers: A review. *Additive Manufacturing, 21,* 1–16. https://doi.org/10.1016/j.addma.2018.01.002

Brenken, B., Barocio, E., Favaloro, A., Kunc, V., & Pipes, R. B. (2019). Development and validation of extrusion deposition additive manufacturing process simulations. *Additive Manufacturing, 25,* 218–226. https://doi.org/10.1016/j.addma.2018.10.041

Caminero, M., Chacón, J., García-Moreno, I., & Reverte, J. (2018). Interlaminar bonding performance of 3D printed continuous fibre reinforced thermoplastic composites using fused deposition modelling. *Polymer Testing, 68,* 415–423. https://doi.org/10.1016/j.polymertesting.2018.04.038

Caminero, M., Chacón, J., García-Moreno, I., & Rodríguez, G. (2018). Impact damage resistance of 3D printed continuous fibre reinforced thermoplastic composites using fused deposition modelling. *Composites Part B: Engineering, 148,* 93–103.https://doi.org/10.1016/j.compositesb.2018.04.054

Cao, L., Xiao, J., Kim, J. K., & Zhang, X. (2023). Effect of post-process treatments on mechanical properties and surface characteristics of 3D printed short glass fiber reinforced PLA/TPU using the FDM process. *CIRP Journal of Manufacturing Science and Technology, 41,* 135–143. https://doi.org/10.1016/j.cirpj.2022.12.008

Cao, M., Cui, T., Yue, Y., Li, C., Guo, X., Jia, X., & Wang, B. (2022). Investigation of carbon fiber on the tensile property of FDM-produced PLA specimen. *Polymers, 14*(23), 5230. https://doi.org/10.3390/polym14235230

Carosella, S., Hügle, S., Helber, F., & Middendorf, P. (2024). A short review on recent advances in automated fiber placement and filament winding technologies. *Composites Part B: Engineering, 287,* 111843. https://doi.org/10.1016/j.compositesb.2024.111843

Cattenone, A., Morganti, S., Alaimo, G., & Auricchio, F. (2019). Finite element analysis of additive manufacturing based on fused deposition modeling: Distortions prediction and comparison with experimental data. *Journal of Manufacturing Science and Engineering, 141*(1), 011010. https://doi.org/10.1115/1.4041626

Cazón, A., Morer, P., & Matey, L. (2014). PolyJet technology for product prototyping: Tensile strength and surface roughness properties. *Proceedings of the Institution of Mechanical Engineers, Part B: Journal of Engineering Manufacture, 228*(12), 1664–1675. https://doi.org/10.1177/0954405413518515

Ceretti, D. V., Edeleva, M., Cardon, L., & D'hooge, D. R. (2023). Molecular pathways for polymer degradation during conventional processing, additive manufacturing, and mechanical recycling. *Molecules, 28*(5), 2344. https://doi.org/10.3390/molecules28052344

Chacón, J. M., Caminero, M. A., García-Plaza, E., & Núñez, P. J. (2017). Additive manufacturing of PLA structures using fused deposition modelling: Effect of process parameters on mechanical properties and their optimal selection. *Materials & Design, 124*, 143–157. https://doi.org/10.1016/j.matdes.2017.03.065

Chen, A. Y., Baehr, S., Turner, A., Zhang, Z., & Gu, G. X. (2021). Carbon-fiber reinforced polymer composites: A comparison of manufacturing methods on mechanical properties. *International Journal of Lightweight Materials and Manufacture, 4*(4), 468–479. https://doi.org/10.1016/j.ijlmm.2021.04.001

Chen, G., Wang, D., Hua, W., Wu, W., Zhou, W., Jin, Y., & Zheng, W. (2023). Simulating and predicting the part warping in fused deposition modeling by thermal–structural coupling analysis. *3D Printing and Additive Manufacturing, 10*(1), 70–82. https://doi.org/10.1089/3dp.2021.0119

Chen, L., & Zhou, D. (2025). Analysis of Numerical Instability Factors and Geometric Reconstruction in 3D SIMP-Based Topology Optimization Towards Enhanced Manufacturability. *Applied Sciences, 15*(11), 6195. https://doi.org/10.3390/app15116195

Cheng, Z., Zhou, J., Liu, Y., Yan, J., Wang, S., Tao, J., . . . Yao, Z. (2024). 3D printed composites based on the magnetoelectric coupling of Fe/FeCo@ C with multiple heterogeneous interfaces for enhanced microwave absorption. *Chemical Engineering Journal, 480*, 148188. https://doi.org/10.1016/j.cej.2024.157810

Chohan, J. S., Mittal, N., Kumar, R., Singh, S., Sharma, S., Singh, J., . . . Dwivedi, S. P. (2020). Mechanical strength enhancement of 3D printed acrylonitrile butadiene styrene polymer components using neural network optimization algorithm. *Polymers, 12*(10), 2250. https://doi.org/10.3390/polym12102250

Chortos, A. (2022). Extrusion 3D printing of conjugated polymers. *Journal of Polymer Science, 60*(3), 486–503. https://doi.org/10.1002/pol.20210609

Christian, P., Jones, I., Rudd, C., Campbell, R., & Corden, T. (2001). Monomer transfer moulding and rapid prototyping methods for fibre reinforced thermoplastics for medical applications. *Composites Part A: Applied Science and Manufacturing, 32*(7), 969–976. https://doi.org/10.1016/S1359-835X(01)00009-4

Cicala, G., Giordano, D., Tosto, C., Filippone, G., Recca, A., & Blanco, I. (2018). Polylactide (PLA) filaments a biobased solution for additive manufacturing: Correlating rheology and thermomechanical properties with printing quality. *Materials, 11*(7), 1191. https://doi.org/10.3390/ma11071191

Colorado, H. A., Velásquez, E. I. G., & Monteiro, S. N. (2020). Sustainability of additive manufacturing: the circular economy of materials and environmental perspectives. *Journal of Materials Research and Technology, 9*(4), 8221–8234. https://doi.org/10.1016/j.jmrt.2020.04.062

Courter, B., Savane, V., Bi, J., Dev, S., & Hansen, C. J. (2017, June). Finite element simulation of the fused deposition modelling process. In *Proceedings of the NAFEMS World Congress*, pp. 11–14.

Cruz Sánchez, F. A., Boudaoud, H., Hoppe, S., & Camargo, M. (2017). Polymer recycling in an open-source additive manufacturing context: Mechanical issues. *additive manufacturing, 17*, 87–105. https://doi.org/10.1016/j.addma.2017.05.013

Dananjaya, V., Somarathna, Y., Siriwardena, S., Sirimuthu, N., Karunanayake, L., & A-beykoon, C. (2024). Effects of latex type and processed-mica waste loading on the structural and thermo-physical properties of natural rubber latex foam composites. *International Journal of Lightweight Materials and Manufacture, 7*(3), 450–466. https://doi.org/10.1016/j.ijlmm.2023.12.002

Depuydt, D., Balthazar, M., Hendrickx, K., Six, W., Ferraris, E., Desplentere, F., . . . Van Vuure, A. W. (2019). Production and characterization of bamboo and flax fiber reinforced polylactic acid filaments for fused deposition modeling (FDM). *Polymer Composites, 40*(5), 1951–1963. https://doi.org/10.1002/pc.24971

Dickson, A. N., Abourayana, H. M., & Dowling, D. P. (2020). 3D printing of fibre-reinforced thermoplastic composites using fused filament fabrication—A review. *Polymers, 12*(10), 2188. https://doi.org/10.3390/polym12102188

Dickson, A. N., Barry, J. N., McDonnell, K. A., & Dowling, D. P. (2017). Fabrication of continuous carbon, glass and Kevlar fibre reinforced polymer composites using additive manufacturing. *Additive Manufacturing, 16,* 146–152. https://doi.org/10.1016/j.addma.2017.06.004

Ding, S., Zou, B., Zhuang, Y., Wang, X., Li, L., & Liu, J. (2023). Hybrid layout and additive manufacturing of continuous carbon/glass fibers reinforced composites, and its effect on mechanical properties. *Composite Structures, 319,* 117133. https://doi.org/10.1016/j.compstruct.2023.117133

Dizon, J. R. C., Espera Jr, A. H., Chen, Q., & Advincula, R. C. (2018). Mechanical characterization of 3D-printed polymers. *Additive Manufacturing, 20,* 44–67. https://doi.org/10.1016/j.addma.2017.12.002

Doumeng, M., Makhlouf, L., Berthet, F., Marsan, O., Delbé, K., Denape, J., & Chabert, F. (2021). A comparative study of the crystallinity of polyetheretherketone by using density, DSC, XRD, and Raman spectroscopy techniques. *Polymer Testing, 93,* 106878. https://doi.org/10.1016/j.polymertesting.2020.106878

Dul, S., Fambri, L., & Pegoretti, A. (2016). Fused deposition modelling with ABS–graphene nanocomposites. *Composites Part A: Applied Science and Manufacturing, 85,* 181–191. https://doi.org/10.1016/j.compositesa.2016.03.013

Dul, S., Fambri, L., & Pegoretti, A. (2018). Filaments production and fused deposition modelling of ABS/carbon nanotubes composites. *Nanomaterials, 8*(1), 49. https://doi.org/10.3390/nano8010049

Egorov, S., Tarasova, T., Skornyakov, I., Hattali, L., Guillaumat, L., & Terekhina, S. (2021). In-nozzle impregnation of continuous textile flax fiber/polyamide 6 composite during FFF process. *Composites Part A: Applied Science and Manufacturing*. https://doi.org/10.1016/j.compositesa.2021.106725

Elfaleh, I., Abbassi, F., Habibi, M., Ahmad, F., Guedri, M., Nasri, M., & Garnier, C. (2023). A comprehensive review of natural fibers and their composites: An eco-friendly alternative to conventional materials. *Results in Engineering, 19,* 101271. https://doi.org/10.1016/j.rineng.2023.101271

Espinach, F., Boufi, S., Delgado-Aguilar, M., Julián, F., Mutjé, P., & Méndez, J. (2018). Composites from poly (lactic acid) and bleached chemical fibres: Thermal properties. *Composites Part B: Engineering, 134,* 169–176. https://doi.org/10.1016/j.compositesb.2017.09.055

Ezair, B., Massarwi, F., & Elber, G. (2015). Orientation analysis of 3D objects toward minimal support volume in 3D-printing. *Computers & Graphics, 51,* 117–124. https://doi.org/10.1016/j.cag.2015.05.009

Faidallah, R. F., Hanon, M. M., Szakál, Z., & Oldal, I. (2022). Biodegradable materials used in FDM 3D printing technology: a critical review. *Journal of Modern Mechanical Engineering and Technology, 9,* 90–105. https://doi.org/10.31875/2409-9848.2022.09.11

Farah, S., Anderson, D. G., & Langer, R. (2016). Physical and mechanical properties of PLA, and their functions in widespread applications—A comprehensive review. *Advanced Drug Delivery Reviews, 107,* 367–392. https://doi.org/10.1016/j.addr.2016.06.012

Fianko, S. K., Dzogbewu, T. C., Agbamava, E., & de Beer, D. J. (2025). Mass Customisation Strategies in Additive Manufacturing: A Systematic Review and Implementation Framework. *Processes, 13*(6), 1855. https://doi.org/10.3390/pr13061855

Fico, D., Rizzo, D., De Carolis, V., Montagna, F., & Esposito Corcione, C. (2022). Sustainable polymer composites manufacturing through 3D printing technologies by using recycled polymer and filler. *Polymers, 14*(18), 3756. https://doi.org/10.3390/polym14183756

Filgueira, D., Holmen, S., Melbø, J. K., Moldes, D., Echtermeyer, A. T., & Chinga-Carrasco, G. (2017). Enzymatic-assisted modification of thermomechanical pulp fibers to improve the interfacial adhesion with poly (lactic acid) for 3D printing. *ACS Sustainable Chemistry & Engineering, 5*(10), 9338–9346. https://doi.org/10.1021/acssuschemeng.7b02351

Folino, A., Pangallo, D., & Calabrò, P. S. (2023). Assessing bioplastics biodegradability by standard and research methods: Current trends and open issues. *Journal of Environmental Chemical Engineering, 11*(2), 109424. https://doi.org/10.1016/j.jece.2023.109424

Franco-Urquiza, E. A., Escamilla, Y. R., & Alcántara Llanas, P. I. (2021). Characterization of 3D printing on jute fabrics. *Polymers, 13*(19), 3202. https://doi.org/10.3390/polym13193202

Gan, Y. X. (2009). Effect of interface structure on mechanical properties of advanced composite materials. *International Journal of Molecular Sciences, 10*(12), 5115–5134. https://doi.org/10.3390/ijms10125115

Gardner, J. M., Sauti, G., Kim, J.-W., Cano, R. J., Wincheski, R. A., Stelter, C. J., . . . Siochi, E. J. (2016). 3-D printing of multifunctional carbon nanotube yarn reinforced components. *Additive Manufacturing, 12,* 38–44. https://doi.org/10.1016/j.addma.2016.06.008

Gauvin, R., & Chibani, M. (2022). The modelling of mold filling in resin transfer molding. *International Polymer Processing, 1*(1), 42–46. https://doi.org/10.1515/217.860042

Ghebretinsae, F., Mikkelsen, O., & Akessa, A. (2019). Strength analysis of 3D printed carbon fibre reinforced thermoplastic using experimental and numerical methods. *IOP Conference Series: Materials Science and Engineering, 700*(1), 012024. https://doi.org/10.1088/1757-899X/700/1/012024

Ghorbani, J., Koirala, P., Shen, Y.-L., & Tehrani, M. (2022). Eliminating voids and reducing mechanical anisotropy in fused filament fabrication parts by adjusting the filament extrusion rate. *Journal of Manufacturing Processes, 80,* 651–658. https://doi.org/10.1016/j.jmapro.2022.06.026

Girdis, J., Gaudion, L., Proust, G., Löschke, S., & Dong, A. (2017). Rethinking timber: investigation into the use of waste macadamia nut shells for additive manufacturing. *Jom, 69*(3), 575–579. https://doi.org/10.1007/s11837-016-2213-6

Gkartzou, E., Koumoulos, E. P., & Charitidis, C. A. (2017). Production and 3D printing processing of bio-based thermoplastic filament. *Manufacturing Review, 4*(1). https://doi.org/10.1051/mfreview/2016020

Goh, G. D., Dikshit, V., Nagalingam, A. P., Goh, G. L., Agarwala, S., Sing, S. L., . . . Yeong, W. Y. (2018). Characterization of mechanical properties and fracture mode of additively manufactured carbon fiber and glass fiber reinforced thermoplastics. *Materials & Design, 137,* 79–89. https://doi.org/10.1016/j.matdes.2017.10.021

Goh, G. D., Yap, Y. L., Agarwala, S., & Yeong, W. Y. (2019). Recent progress in additive manufacturing of fiber reinforced polymer composite. *Advanced Materials Technologies, 4*(1), 1800271. https://doi.org/10.1002/admt.201800271

Gowtham, P., Jayasheela, M., Sivamani, C., & Balaji, D. (2024). Interfacing the IoT in composite manufacturing: An overview. *Reviews on Advanced Materials Science, 63*(1), 20240026. https://doi.org/10.1515/rams-2024-0026

Gray IV, R. W., Baird, D. G., & Helge Bøhn, J. (1998). Effects of processing conditions on short TLCP fiber reinforced FDM parts. *Rapid Prototyping Journal, 4*(1), 14–25. https://doi.org/10.1108/13552549810197514

Gribniak, V. (2023). Material-oriented engineering for eco-optimized structures—A new design approach. *Advanced materials letters, 14*(1), 1–8. https://doi.org/10.5185/amlett.2023.011713

Gribniak, V., Rimkus, A., Misiūnaitė, I., & Zakaras, T. (2022). Improving local stability of aluminium profile with low-modulus stiffeners: Experimental and numerical web buckling analysis. *Thin-Walled Structures, 172,* 108858. https://doi.org/10.1016/j.tws.2021.108858

Gribniak, V., Rimkus, A., Plioplys, L., Misiūnaitė, I., Boris, R., & Pravilonis, T. (2021a). Evaluating mechanical efficiency of glass fibres in a polymer profile. *Polymer Testing, 102,* 107338. https://doi.org/10.1016/j.polymertesting.2021.107338

Gribniak, V., Rimkus, A., Plioplys, L., Misiūnaitė, I., Garnevičius, M., Boris, R., & Šapalas, A. (2021b). An efficient approach to describe the fiber effect on mechanical performance of pultruded GFRP profiles. *Frontiers in Materials, 8*, 746376. https://doi.org/10.3389/fmats.2021.746376

Gribniak, V., Rimkus, A., Torres, L., & Jakstaite, R. (2017). Deformation analysis of reinforced concrete ties: Representative geometry. *Structural Concrete, 18*(4), 634–647. https://doi.org/10.1002/suco.201600105

Gupta, A., & Ogale, A. (2002). Dual curing of carbon fiber reinforced photoresins for rapid prototyping. *Polymer Composites, 23*(6), 1162–1170. https://doi.org/10.1002/pc.10509

Hachimi, T., Majid, F., Zekriti, N., Rhanim, R., & Rhanim, H. (2024). Improvement of 3D printing polymer simulations considering converting G-code to ABAQUS. *The International Journal of Advanced Manufacturing Technology, 131*(9), 5193–5208. https://doi.org/10.1007/s00170-024-13300-9

Hamel, J., Salsbury, C., & Bouck, A. (2018). Characterizing the effects of additive manufacturing process settings on part performance using approximation-assisted multi-objective optimization. *Progress in Additive Manufacturing, 3*(3), 123–143. https://doi.org/10.1007/s40964-018-0043-5

Han, P., Torabnia, S., Riyad, M. F., Bawareth, M., & Hsu, K. (2024). Effect of laser heating on mechanical strength of carbon fiber–reinforced nylon in fused filament fabrication. *The International Journal of Advanced Manufacturing Technology, 133*(11), 6139–6146. https://doi.org/10.1007/s00170-024-14103-8

Han, P., Torabnia, S., Riyad, M. F., Thippanna, V., Song, K., & Hsu, K. (2025). In-process laser heating for mechanical strength improvement of FFF-printed PEEK. *Progress in Additive Manufacturing, 10*(5), 3729–3738. https://doi.org/10.1007/s40964-024-00833-4

Hanon, M. M., Marczis, R., & Zsidai, L. (2021). Influence of the 3D printing process settings on tensile strength of PLA and HT-PLA. *Periodica Polytechnica Mechanical Engineering, 65*(1), 38–46. https://doi.org/10.3311/PPme.13683

Hao, W., Liu, Y., Zhou, H., Chen, H., & Fang, D. (2018). Preparation and characterization of 3D printed continuous carbon fiber reinforced thermosetting composites. *Polymer Testing, 65*, 29–34. https://doi.org/10.1016/j.polymertesting.2017.11.004

Hasyim, S., Salam, N., Pallu, M. S., & Maricar, F. (2023). Study on the Manufacturing of Composite Materials Made from Glass Fiber Reinforced Polymer (GFRP) in Indonesia for Use as Lining in Open Channels. *Key Engineering Materials, 959*, 207–219. https://doi.org/10.4028/p-95WrEa

Hedayati, S. K., Behravesh, A. H., Hasannia, S., Saed, A. B., & Akhoundi, B. (2020). 3D printed PCL scaffold reinforced with continuous biodegradable fiber yarn: A study on mechanical and cell viability properties. *Polymer Testing, 83,* 106347. https://doi.org/10.1016/j.polymertesting.2020.106347

Hetrick, D. R., Sanei, S. H. R., Ashour, O., & Bakis, C. E. (2021). Charpy impact energy absorption of 3D printed continuous Kevlar reinforced composites. *Journal of Composite Materials, 55*(12), 1705–1713. https://doi.org/10.1177/0021998320985596

Hisham, M., Dileep, C., Jacob, L., & Butt, H. (2024). Additive manufacturing of carbon nanocomposites for structural applications. *Journal of Materials Research and Technology, 28,* 4674–4693. https://doi.org/10.1016/j.jmrt.2024.01.049

Hoang, T. D., Van Anh, N., Yusuf, M., Ali S. A, M., Subramanian, Y., Hoang Nam, N., . . . Abi Bianasari, A. (2024). Valorization of Agriculture Residues into Value-Added Products: A Comprehensive Review of Recent Studies. *The Chemical Record, 24*(8), e202300333. https://doi.org/10.1002/tcr.202300333

Hofstätter, T., Gutmann, I. W., Koch, T., Pedersen, D. B., Tosello, G., Heinz, G., & Hansen, H. N. (2016). Distribution and orientation of carbon fibers in polylactic acid parts produced by fused deposition modeling. In *Proceedings of the ASPE Summer Topical Meeting 2016*.

Hong, S. Y., Kim, Y. C., Wang, M., Kim, H.-I., Byun, D.-Y., Nam, J.-D., . . . Suhr, J. (2018). Experimental investigation of mechanical properties of UV-Curable 3D printing materials. *Polymer, 145,* 88–94. https://doi.org/10.1016/j.polymer.2018.04.067

Hu, Q., Duan, Y., Zhang, H., Liu, D., Yan, B., & Peng, F. (2018). Manufacturing and 3D printing of continuous carbon fiber prepreg filament. *Journal of Materials Science, 53*(3), 1887–1898. https://doi.org/10.1007/s10853-017-1624-2

Hu, Z., & Mahadevan, S. (2017). Uncertainty quantification and management in additive manufacturing: current status, needs, and opportunities. *The International Journal of Advanced Manufacturing Technology, 93*(5), 2855–2874. https://doi.org/10.1007/s00170-017-0703-5

Huang, B., Meng, S., He, H., Jia, Y., Xu, Y., & Huang, H. (2019). Study of processing parameters in fused deposition modeling based on mechanical properties of acrylonitrile-butadiene-styrene filament. *Polymer Engineering & Science, 59*(1), 120–128. https://doi.org/10.1002/pen.24875

Hussain, M., Khan, S. M., Shafiq, M., & Abbas, N. (2024). A review on PLA-based biodegradable materials for biomedical applications. *Giant, 18,* 100261. https://doi.org/10.1016/j.giant.2024.100261

Hussein, A., Hao, L., Yan, C., & Everson, R. (2013). Finite element simulation of the temperature and stress fields in single layers built without-support in selective laser melting. *Materials & Design (1980-2015), 52,* 638–647. https://doi.org/10.1016/j.matdes.2013.05.070

Iftekar, S. F., Aabid, A., Amir, A., & Baig, M. (2023). Advancements and limitations in 3D printing materials and technologies: a critical review. *Polymers, 15*(11), 2519. https://doi.org/10.3390/polym15112519

Islam, M., Xayachak, T., Haque, N., Lau, D., Bhuiyan, M., & Pramanik, B. K. (2024). Impact of bioplastics on environment from its production to end-of-life. *Process Safety and Environmental Protection, 188,* 151–166. https://doi.org/10.1016/j.psep.2024.05.113

Islam, S., & Bagheri, Z. S. (2025). Investigating the impact of 3D printing process parameters on the mechanical and morphological properties of fiber-reinforced thermoplastic polyurethane composites. *Polymer Engineering & Science*, 65(7), 3432–3451. https://doi.org/10.1002/pen.27224

ISO (International Organization for Standardization) (1966). *Plastics – Determination of tensile properties*, ISO R527:1966.

ISO (International Organization for Standardization) (1975). *Plastics — Determination of flexural properties*, ISO R178:1975.

ISO (International Organization for Standardization) (1982). *Plastics — Determination of Charpy impact properties*, ISO 179:1982.

ISO (International Organization for Standardization) (2012a). *Plastics — Determination of tensile properties — Part 1: General principles*, ISO 527-1:2012.

ISO (International Organization for Standardization) (2012b). *Plastics — Determination of tensile properties — Part 2: Test conditions for moulding and extrusion plastics*, ISO 527-2:2012.

ISO (International Organization for Standardization) (2019). *Plastics — Determination of tensile properties. Part 1: General principles* ISO 527-1:2019.

ISO (International Organization for Standardization) (2021). *Additive manufacturing — General principles — Fundamentals and vocabulary*, ISO/ASTM 52900:2021.

Jiang, D., Hoglund, R., & Smith, D. E. (2019). Continuous fiber angle topology optimization for polymer composite deposition additive manufacturing applications. *Fibers, 7*(2), 14. https://doi.org/10.3390/fib7020014

Jing, W., Hui, C., Qiong, W., Hongbo, L., & Zhanjun, L. (2017). Surface modification of carbon fibers and the selective laser sintering of modified carbon fiber/nylon 12 composite powder. *Materials & Design, 116,* 253-260. https://doi.org/10.1016/j.matdes.2016.12.037

Kabir, S. F., Mathur, K., & Seyam, A.-F. M. (2020). A critical review on 3D printed continuous fiber-reinforced composites: History, mechanism, materials and properties. *Composite Structures, 232,* 111476. https://doi.org/10.1016/j.compstruct.2019.111476

Kalsoom, U., Nesterenko, P. N., & Paull, B. (2016). Recent developments in 3D printable composite materials. *Rsc Advances, 6*(65), 60355-60371. https://doi.org/10.1039/C6RA11334F

Kamarudin, S. H., Mohd Basri, M. S., Rayung, M., Abu, F., Ahmad, S. b., Norizan, M. N., . . . Abdullah, U. H. (2022). A review on natural fiber reinforced polymer composites (NFRPC) for sustainable industrial applications. *Polymers, 14*(17), 3698. https://doi.org/10.3390/polym14173698

Kantaros, A., Drosos, C., Papoutsidakis, M., Pallis, E., & Ganetsos, T. (2025). Composite Filament Materials for 3D-Printed Drone Parts: Advancements in Mechanical Strength, Weight Optimization and Embedded Electronics. *Materials, 18*(11), 2465. https://doi.org/10.3390/ma18112465

Karimi, A., Rahmatabadi, D., & Baghani, M. (2024). Various FDM mechanisms used in the fabrication of continuous-fiber reinforced composites: a review. *Polymers, 16*(6), 831. https://doi.org/10.3390/polym16060831

Kariz, M., Sernek, M., & Kuzman, M. K. (2016). Use of wood powder and adhesive as a mixture for 3D printing. *European journal of wood and wood products, 74*(1), 123–126. https://doi.org/10.1007/s00107-015-0987-9

Karkun, M. S., & Dharmalingam, S. (2022). 3D printing technology in aerospace industry–a review. *International Journal of Aviation, Aeronautics, and Aerospace, 9*(2), 4. https://doi.org/10.15394/ijaaa.2022.1708

Kavosi, J., Creasy, T. S., Palazzolo, A., & Naraghi, M. (2020). Crosslinked network microstructure of carbon nanomaterials promotes flaw-tolerant mechanical response. *Nanotechnology, 31*(31), 315606. https://doi.org/10.1088/1361-6528/ab8b92

Kennedy, S. M., Wilson, L. A., & Rb, J. R. (2025). Natural fiber filaments transforming the future of sustainable 3D printing. *MethodsX*, 103385. https://doi.org/10.1016/j.mex.2025.103385

Kęsy, A., & Kotliński, J. (2010). Mechanical properties of parts produced by using polymer jetting technology. *Archives of civil and mechanical engineering, 10*(3), 37–50. https://doi.org/10.1016/S1644-9665(12)60135-6

Khalid, M. Y., Al Rashid, A., Arif, Z. U., Ahmed, W., Arshad, H., & Zaidi, A. A. (2021). Natural fiber reinforced composites: Sustainable materials for emerging applications. *Results in Engineering, 11*, 100263. https://doi.org/10.1016/j.rineng.2021.100263

Khanafer, K., Al-Masri, A., Deiab, I., & Vafai, K. (2022). Thermal analysis of fused deposition modeling process based finite element method: Simulation and parametric study. *Numerical Heat Transfer, Part A: Applications, 81*(3–6), 94–118. https://doi.org/10.1080/10407782.2022.2038972

Khare, K. S., Khabaz, F., & Khare, R. (2014). Effect of carbon nanotube functionalization on mechanical and thermal properties of cross-linked epoxy–carbon nanotube nanocomposites: role of strengthening the interfacial interactions. *ACS applied materials & interfaces, 6*(9), 6098–6110. https://doi.org/10.1021/am405317x

Khoshkhoo, A., Carrano, A. L., & Blersch, D. M. (2018). Effect of surface slope and build orientation on surface finish and dimensional accuracy in material jetting processes. *Procedia Manufacturing, 26*, 720–730. https://doi.org/10.1016/j.promfg.2018.07.082

Kim, C.-H., Kim, H.-Y., Kim, J.-H., & Kim, J. (2023). 3D printing-based soft auxetic structures using PDMS-Ecoflex Hybrid. *Functional Composites and Structures, 5*(1), 015006. https://doi.org/10.1088/2631-6331/acc0cf

Kim, K., Zhu, W., Qu, X., Aaronson, C., McCall, W. R., Chen, S., & Sirbuly, D. J. (2014). 3D optical printing of piezoelectric nanoparticle–polymer composite materials. *ACS nano, 8*(10), 9799–9806. https://doi.org/10.1021/nn503268f

Kirubakaran, G., Senthamaraikannan, C., & Vignesh, M. (2025). Effect of raster orientation on pure nylon, carbon fibre nylon, and glass fibre nylon using three-dimensional printing. *Proceedings of the Institution of Mechanical Engineers, Part E: Journal of Process Mechanical Engineering, 239*(5), 2954–2962. https://doi.org/10.1177/09544089241239821

Kleijnen, R. G., Sesseg, J., Schmid, M., & Wegener, K. (2017). Insights into the development of a short-fiber reinforced polypropylene for laser sintering. *Paper presented at the AIP Conference Proceedings, 1914*(1), 190003. https://doi.org/10.1063/1.5016791

Kumar, M. B., & Sathiya, P. (2021). Methods and materials for additive manufacturing: A critical review on advancements and challenges. *Thin-Walled Structures, 159*, 107228. https://doi.org/10.1016/j.tws.2020.107228

Kunwar, P., Xiong, Z., & Soman, P. (2021). *Hybrid laser platform (HLP) for printing 3D multiscale multi-material hydrogel structures.* Paper presented at the Laser 3D Manufacturing VIII. https://doi.org/10.1117/12.2577781

La Fuente, C. I. A., Maniglia, B. C., & Tadini, C. C. (2023). Biodegradable polymers: A review about biodegradation and its implications and applications. *Packaging Technology and Science, 36*(2), 81–95. https://doi.org/10.1002/pts.2699

Lagman-Bautista, J. (2020). Ecological footprint accounting of non-biodegradable wastes of Angeles City, Philippines: the anthropogenic shift to biodegradables. *Journal of Environmental Science and Management*, (1). https://doi.org/10.47125/jesam/2020_sp1/05

Lanzotti, A., Martorelli, M., Maietta, S., Gerbino, S., Penta, F., & Gloria, A. (2019). A comparison between mechanical properties of specimens 3D printed with virgin and recycled PLA. *Procedia CIRP, 79*, 143–146. https://doi.org/10.1016/j.procir.2019.02.030

Larson, S., Newman, J., O Connor, G., Griggs, C., Martin, A., Nijak, G., . . . Leeson, A. (2013). *Biopolymer as an alternative to petroleum-based polymers to control soil erosion: Iowa Army ammunition plant*. https://doi.org/10.21236/ADA621917

Le Duigou, A., Castro, M., Bevan, R., & Martin, N. (2016). 3D printing of wood fibre biocomposites: From mechanical to actuation functionality. *Materials & Design, 96*, 106–114. https://doi.org/10.1016/j.matdes.2016.02.018

Lee, D., & Wu, G.-Y. (2020). Parameters affecting the mechanical properties of three-dimensional (3D) printed carbon fiber-reinforced polylactide composites. *Polymers, 12*(11), 2456. https://doi.org/10.3390/polym12112456

Lendvai, L., Fekete, I., Jakab, S. K., Szarka, G., Verebélyi, K., & Iván, B. (2024). Influence of environmental humidity during filament storage on the structural and mechanical properties of material extrusion 3D-printed poly (lactic acid) parts. *Results in Engineering, 24*, 103013. https://doi.org/10.1016/j.rineng.2024.103013

Li, H., Liu, B., Ge, L., Chen, Y., Zheng, H., & Fang, D. (2021). Mechanical performances of continuous carbon fiber reinforced PLA composites printed in vacuum. *Composites Part B: Engineering, 225*, 109277. https://doi.org/10.1016/j.compositesb.2021.109277

Li, N., Huang, S., Zhang, G., Qin, R., Liu, W., Xiong, H., . . . Blackburn, J. (2019). Progress in additive manufacturing on new materials: A review. *Journal of Materials Science & Technology, 35*(2), 242–269. https://doi.org/10.1016/j.jmst.2018.09.002

Li, N., Li, Y., & Liu, S. (2016). Rapid prototyping of continuous carbon fiber reinforced polylactic acid composites by 3D printing. *Journal of Materials Processing Technology, 238*, 218–225. https://doi.org/10.1016/j.jmatprotec.2016.07.025

Li, S., Yuan, S., Zhu, J., Wang, C., Li, J., & Zhang, W. (2020). Additive manufacturing-driven design optimization: Building direction and structural topology. *Additive Manufacturing, 36*, 101406. https://doi.org/10.1016/j.addma.2020.101406

Li, T., Huang, Z., Tsui, G. C.-P., Tang, C.-Y., & Deng, Y. (2024). Recent advances in 4D printing of hydrogels. *Reviews on Advanced Materials Science, 63*(1), 20240028. https://doi.org/10.1515/rams-2024-0028

Li, X., Ni, Z., Bai, S., & Lou, B. (2018). *Preparation and mechanical properties of fiber reinforced PLA for 3D printing materials.* Paper presented at the IOP Conference Series: Materials Science and Engineering. https://doi.org/10.1088/1757-899X/322/2/022012

Li, Y., Huang, L., Wang, X., Wang, Y., Lu, X., Wei, Z., . . . Huang, C. (2023). Blending and functionalisation modification of 3D printed polylactic acid for fused deposition modeling. *Reviews on Advanced Materials Science, 62*(1), 20230140. https://doi.org/10.1515/rams-2023-0140

Liao, G., Li, Z., Cheng, Y., Xu, D., Zhu, D., Jiang, S., . . . Zhu, Y. (2018). Properties of oriented carbon fiber/polyamide 12 composite parts fabricated by fused deposition modeling. *Materials & Design, 139*, 283–292. https://doi.org/10.1016/j.matdes.2017.11.027

Liu, F., Wang, S., Zhang, J., Zhang, W., Snels, L., Seveno, D., . . . Ivens, J. (2025). Thermal history and multi-scale analyses of 3D-printed continuous carbon fibre composites. *Composites Part A: Applied Science and Manufacturing*, 109058. https://doi.org/10.1016/j.compositesa.2025.109058

Liu, G., Xiong, Y., & Zhou, L. (2021). Additive manufacturing of continuous fiber reinforced polymer composites: Design opportunities and novel applications. *Composites Communications, 27*, 100907. https://doi.org/10.1016/j.coco.2021.100907

Liu, L., Jia, C., He, J., Zhao, F., Fan, D., Xing, L., . . . Huang, Y. (2015). Interfacial characterization, control and modification of carbon fiber reinforced polymer composites. *Composites Science and Technology, 121*, 56–72. https://doi.org/10.1016/j.compscitech.2015.08.002

Liu, T., Liu, X., & Feng, P. (2020). A comprehensive review on mechanical properties of pultruded FRP composites subjected to long-term environmental effects. *Composites Part B: Engineering, 191*, 107958. https://doi.org/10.1016/j.compositesb.2020.107958

Lordi, V., & Yao, N. (2000). Molecular mechanics of binding in carbon-nanotube–polymer composites. *Journal of Materials Research, 15*(12), 2770–2779. https://doi.org/10.1557/JMR.2000.0396

Love, L. J., Kunc, V., Rios, O., Duty, C. E., Elliott, A. M., Post, B. K., . . . Blue, C. A. (2014). The importance of carbon fiber to polymer additive manufacturing. *Journal of Materials Research, 29*(17), 1893–1898. https://doi.org/10.1557/jmr.2014.212

Lubliner, J. (2008). *Plasticity theory*. Dover Publications.

Lumpe, T. S., Mueller, J., & Shea, K. (2019). Tensile properties of multi-material interfaces in 3D printed parts. *Materials & Design, 162*, 1–9. https://doi.org/10.1016/j.matdes.2018.11.024

Maqsood, N., & Rimašauskas, M. (2021). Delamination observation occurred during the flexural bending in additively manufactured PLA-short carbon fiber filament reinforced with continuous carbon fiber composite. *Results in Engineering, 11*, 100246. https://doi.org/10.1016/j.rineng.2021.100246

Martínez-García, A., Monzón, M., & Paz, R. (2021). Standards for additive manufacturing technologies: Structure and impact. *Additive Manufacturing* (pp. 395–408). Elsevier. https://doi.org/10.1016/B978-0-12-818411-0.00013-6

Matsuzaki, R., Ueda, M., Namiki, M., Jeong, T.-K., Asahara, H., Horiguchi, K., . . . Hirano, Y. (2016). Three-dimensional printing of continuous-fiber composites by in-nozzle impregnation. *Scientific Reports, 6*(1), 23058. https://doi.org/10.1038/srep23058

Matúš, M., Križan, P., Kijovský, J., Strigáč, S., Beniak, J., & Šooš, Ľ. (2023). Implementation of Finite Element Method Simulation in Control of Additive Manufacturing to Increase Component Strength and Productivity. *Symmetry, 15*(11), 2036. https://doi.org/10.3390/sym15112036

Mazzanti, V., Pariante, R., Bonanno, A., de Ballesteros, O. R., Mollica, F., & Filippone, G. (2019). Reinforcing mechanisms of natural fibers in green composites: Role of fibers morphology in a PLA/hemp model system. *Composites Science and Technology, 180*, 51–59. https://doi.org/10.1016/j.compscitech.2019.05.015

Melenka, G. W., Cheung, B. K., Schofield, J. S., Dawson, M. R., & Carey, J. P. (2016). Evaluation and prediction of the tensile properties of continuous fiber-reinforced 3D printed structures. *Composite Structures, 153*, 866–875. https://doi.org/10.1016/j.compstruct.2016.07.018

Memarzadeh, A., Safaei, B., Tabak, A., Sahmani, S., & Kizilors, C. (2023). Advancements in additive manufacturing of polymer matrix composites: a systematic review of techniques and properties. *Materials Today Communications, 36*, 106449. https://doi.org/10.1016/j.mtcomm.2023.106449

Milosevic, M., Stoof, D., & Pickering, K. L. (2017). Characterizing the mechanical properties of fused deposition modelling natural fiber recycled polypropylene composites. *Journal of Composites Science, 1*(1), 7. https://doi.org/10.3390/jcs1010007

Misiūnaitė, I., Rimkus, A., & Gribniak, V. (2025). Developing lightweight steel profile and lattice polymeric core composite for structural use. *Thin-Walled Structures, 206*, 112697. https://doi.org/10.1016/j.tws.2024.112697

Mohammadian, Y., & Nasirzadeh, N. (2021). Toxicity risks of occupational exposure in 3D printing and bioprinting industries: a systematic review. *Toxicology and Industrial Health, 37*(9), 573–584. https://doi.org/10.1177/07482337211031691

Mohammed, M., Rahman, R., Mohammed, A. M., Adam, T., Betar, B. O., Osman, A. F., & Dahham, O. S. (2022). Surface treatment to improve water repellence and compatibility of natural fiber with polymer matrix: Recent advancement. *Polymer Testing, 115*, 107707. https://doi.org/10.1016/j.polymertesting.2022.107707

Mokhena, T., Mochane, M., Mtibe, A., Sigonya, S., Ntsendwana, B., Masibi, E., . . . Motsoeneng, T. (2024). Recent advances on nanocellulose-graphene oxide composites: a review. *Cellulose, 31*(12), 7207–7249. https://doi.org/10.1007/s10570-024-06055-9

Mora, A., Verma, P., & Kumar, S. (2020). Electrical conductivity of CNT/polymer composites: 3D printing, measurements and modeling. *Composites Part B: Engineering, 183*, 107600. https://doi.org/10.1016/j.compositesb.2019.107600

Mosleh, N., Esfandeh, M., & Dariushi, S. (2024). Simulation of temperature profile in fused filament fabrication 3D printing method. *Rapid Prototyping Journal, 30*(1), 134–144. https://doi.org/10.1108/RPJ-02-2023-0067

Motaparti, K. P., Taylor, G., Leu, M. C., Chandrashekhara, K., Castle, J., & Matlack, M. (2017). Experimental investigation of effects of build parameters on flexural properties in fused deposition modelling parts. *Virtual and Physical Prototyping, 12*(3), 207–220. https://doi.org/10.1080/17452759.2017.1314117

Nakagawa, Y., Mori, K.-i., & Maeno, T. (2017). 3D printing of carbon fibre-reinforced plastic parts. *The International Journal of Advanced Manufacturing Technology, 91*(5), 2811–2817. https://doi.org/10.1007/s00170-016-9891-7

Nikzad, M., Masood, S. H., & Sbarski, I. (2011). Thermo-mechanical properties of a highly filled polymeric composites for fused deposition modeling. *Materials & Design, 32*(6), 3448–3456. https://doi.org/10.1016/j.matdes.2011.01.056

Ning, F., Cong, W., Hu, Y., & Wang, H. (2017). Additive manufacturing of carbon fiber-reinforced plastic composites using fused deposition modeling: Effects of process parameters on tensile properties. *Journal of Composite Materials, 51*(4), 451–462. https://doi.org/10.1177/0021998316646169

Ogaili, A. A. F., Basem, A., Kadhim, M. S., Al-Sharify, Z. T., Jaber, A. A., Njim, E. K., . . . Al-Ameen, E. S. (2024). The effect of chopped carbon fibers on the mechanical properties and fracture toughness of 3D-printed PLA parts: an experimental and simulation study. *Journal of Composites Science, 8*(7), 273. https://doi.org/10.3390/jcs8070273

Paciorek-Sadowska, J., Borowicz, M., & Isbrandt, M. (2019). New Poly(lactide-urethane-isocyanurate) Foams Based on Bio-Polylactide Waste. *Polymers, 11*(3). https://doi.org/10.3390/polym11030481

Palanikumar, K., Mudhukrishnan, M., & Soorya Prabha, P. (2020). Technologies in additive manufacturing for fiber reinforced composite materials: a review. *Current Opinion in Chemical Engineering, 28,* 51–59. https://doi.org/10.1016/j.coche.2020.01.001

Panerai, A., Canegrati, A., Martulli, L., Kostovic, M., Rollo, G., Sorrentino, A., . . . Bernasconi, A. (2023). Fatigue behaviour of additively manufactured short fibre reinforced polyamide. *International Journal of Fatigue, 174,* 107711. https://doi.org/10.1016/j.ijfatigue.2023.107711

Parker, M., Inthavong, A., Law, E., Waddell, S., Ezeokeke, N., Matsuzaki, R., & Arola, D. (2022). 3D printing of continuous carbon fiber reinforced polyphenylene sulfide: Exploring printability and importance of fiber volume fraction. *Additive Manufacturing, 54*, 102763. https://doi.org/10.1016/j.addma.2022.102763

Peinado, V., Castell, P., García, L., & Fernández, Á. (2015). Effect of Extrusion on the Mechanical and Rheological Properties of a Reinforced Poly(Lactic Acid): Reprocessing and Recycling of Biobased Materials. *Materials, 8*(10). https://doi.org/10.3390/ma8105360

Phiri, R., Rangappa, S. M., Siengchin, S., Oladijo, O. P., & Dhakal, H. N. (2023). Development of sustainable biopolymer-based composites for lightweight applications from agricultural waste biomass: A review. *Advanced Industrial and Engineering Polymer Research, 6*(4), 436–450. https://doi.org/10.1016/j.aiepr.2023.04.004

Pirchio, D., Althouse, J. A., Madlem, T. A., Denavit, M. D., Weldon, B. D., & Walsh, K. Q. (2023). Tensile strength and modulus of FRP pultruded composites at varying load angles relative to the pultrusion direction. *Construction and Building Materials, 385*, 131477. https://doi.org/10.1016/j.conbuildmat.2023.131477

Pitt, K., Lopez-Botello, O., Lafferty, A. D., Todd, I., & Mumtaz, K. (2017). Investigation into the material properties of wooden composite structures with in-situ fibre reinforcement using additive manufacturing. *Composites Science and Technology, 138,* 32–39. https://doi.org/10.1016/j.compscitech.2016.11.008

Plamadiala, I., Croitoru, C., Pop, M. A., & Roata, I. C. (2025). Enhancing polylactic acid (PLA) performance: A review of additives in fused deposition modelling (FDM) filaments. *Polymers, 17*(2), 191. https://doi.org/10.3390/polym17020191

Plymill, A., Minneci, R., Greeley, D. A., & Gritton, J. (2016). *Graphene and Carbon Nanotube PLA Composite Feedstock Development for Fused Deposition Modeling.* (Chancellor’s Honors Program Projects). University of Tennessee.

Pokorný, P., Delgado Sobrino, D. R., Václav, Š., Petru, J., & Gołębski, R. (2023). Research into specific mechanical properties of composites produced by 3D-printing additive continuous-fiber fabrication technology. *Materials, 16*(4), 1459. https://doi.org/10.3390/ma16041459

Post, W., Kuijpers, L. J., Zijlstra, M., Van Der Zee, M., & Molenveld, K. (2021). Effect of mineral fillers on the mechanical properties of commercially available biodegradable polymers. *Polymers, 13*(3), 394. https://doi.org/10.3390/polym13030394

Pu, J., McIlroy, C., Jones, A., & Ashcroft, I. (2021). Understanding mechanical properties in fused filament fabrication of polyether ether ketone. *Additive Manufacturing, 37*, 101673. https://doi.org/10.1016/j.addma.2020.101673

Punera, D., & Mukherjee, P. (2022). Recent developments in manufacturing, mechanics, and design optimization of variable stiffness composites. *Journal of Reinforced Plastics and Composites, 41*(23–24), 917–945. https://doi.org/10.1177/07316844221082999

Qiao, P., Yang, M., & Bobaru, F. (2008). Impact mechanics and high-energy absorbing materials. *Journal of Aerospace Engineering, 21*(4), 235–248. https://doi.org/10.1061/(ASCE)0893-1321(2008)21:4(235)

Qin, D., Sang, L., Zhang, Z., Lai, S., & Zhao, Y. (2022). Compression performance and deformation behavior of 3D-printed PLA-based lattice structures. *Polymers, 14*(5), 1062. https://doi.org/10.3390/polym14051062

Quan, Z., Wu, A., Keefe, M., Qin, X., Yu, J., Suhr, J., . . . Chou, T.-W. (2015). Additive manufacturing of multi-directional preforms for composites: opportunities and challenges. *Materials Today, 18*(9), 503–512. https://doi.org/10.1016/j.mattod.2015.05.001

Radzi, A., Zaki, S. A., Hassan, M. Z., Ilyas, R., Jamaludin, K. R., Daud, M. Y. M., & Aziz, S. A. (2022). Bamboo-fiber-reinforced thermoset and thermoplastic polymer composites: A review of properties, fabrication, and potential applications. *Polymers, 14*(7), 1387. https://doi.org/10.3390/polym14071387

Rahmati, M., & Zolfaghari, A. (2024). Effect of printing parameters on the mechanical properties of 3D printed short glass fiber/acrylonitrile butadiene styrene composites. *Polymers for Advanced Technologies, 35*(9), e6576. https://doi.org/10.1002/pat.6576

Ramesh, M., Rajeshkumar, L., & Balaji, D. (2021). Influence of process parameters on the properties of additively manufactured fiber-reinforced polymer composite materials: a review. *Journal of Materials Engineering and Performance, 30*(7), 4792–4807. https://doi.org/10.1007/s11665-021-05832-y

Ray, S. S., Yamada, K., Okamoto, M., & Ueda, K. (2003). New polylactide-layered silicate nanocomposites. 2. Concurrent improvements of material properties, biodegradability and melt rheology. *Polymer, 44*(3), 857–866. https://doi.org/10.1016/S0032-3861(02)00818-2

Rayegani, F., & Onwubolu, G. C. (2014). Fused deposition modelling (FDM) process parameter prediction and optimization using group method for data handling (GMDH) and differential evolution (DE). *The International Journal of Advanced Manufacturing Technology, 73*(1), 509–519. https://doi.org/10.1007/s00170-014-5835-2

Reddy, M. V., Hemasunder, B., Chavan, P. M., Dish, N., & Savio, A. P. (2023). Study on the significance of process parameters in improvising the tensile strength of FDM printed carbon fibre reinforced PLA. *Materials Today: Proceedings*. https://doi.org/10.1016/j.matpr.2023.06.330

Reichl, K., & Inman, D. (2018). Dynamic mechanical and thermal analyses of Objet Connex 3D printed materials. *Experimental Techniques, 42*(1), 19–25. https://doi.org/10.1007/s40799-017-0223-0

Rezaie, R., Badrossamay, M., Ghaie, A., & Moosavi, H. (2013). Topology optimization for fused deposition modeling process. *Procedia CIRP, 6*, 521–526. https://doi.org/10.1016/j.procir.2013.03.098

Rimašauskas, M., Kuncius, T., & Rimašauskienė, R. (2019). Processing of carbon fiber for 3D printed continuous composite structures. *Materials and Manufacturing Processes, 34*(13), 1528–1536. https://doi.org/10.1080/10426914.2019.1655152

Riseh, R. S., Vazvani, M. G., Hassanisaadi, M., & Thakur, V. K. (2024). Agricultural wastes: A practical and potential source for the isolation and preparation of cellulose and application in agriculture and different industries. *Industrial Crops and Products, 208*, 117904. https://doi.org/10.1016/j.indcrop.2023.117904

Roper, D. A., Good, B. L., McCauley, R., Yarlagadda, S., Smith, J., Good, A., . . . Mirotznik, M. S. (2014). Additive manufacturing of graded dielectrics. *Smart Materials and Structures, 23*(4), 045029. https://doi.org/10.1088/0964-1726/23/4/045029

Rosenboom, J.-G., Langer, R., & Traverso, G. (2022). Bioplastics for a circular economy. *Nature Reviews Materials, 7*(2), 117–137. https://doi.org/10.1038/s41578-021-00407-8

Rossini, M., Saqan, E., & Nanni, A. (2019). Prediction of the creep rupture strength of GFRP bars. *Construction and Building Materials, 227*, 116620. https://doi.org/10.1016/j.conbuildmat.2019.08.001

Ryu, J. E., Salcedo, E., Lee, H. J., Jang, S. J., Jang, E. Y., Yassi, H. A., . . . Lee, E. (2019). Material models and finite analysis of additively printed polymer composites. *Journal of Composite Materials, 53*(3), 361–371. https://doi.org/10.1177/0021998318785672

Saari, M., Cox, B., Richer, E., Krueger, P. S., & Cohen, A. L. (2015). Fiber encapsulation additive manufacturing: An enabling technology for 3D printing of electromechanical devices and robotic components. *3D Printing and Additive Manufacturing, 2*(1), 32–39. https://doi.org/10.1089/3dp.2015.0003

SAC (Standardization Administration of China) (2006). *Plastics — Determination of tensile properties — Part 2: Test conditions for moulding and extrusion plastics (GB/T 1040.2-2006).*

SAC (Standardization Administration of China) (2008). *Plastics — Determination of flexural properties (GB/T 9341-2008).*

Safari, F., Kami, A., & Abedini, V. (2022). 3D printing of continuous fiber reinforced composites: A review of the processing, pre-and post-processing effects on mechanical properties. *Polymers and Polymer Composites, 30*, 09673911221098734. https://doi.org/10.1177/09673911221098734

Samir, A., Ashour, F. H., Hakim, A. A., & Bassyouni, M. (2022). Recent advances in biodegradable polymers for sustainable applications. *Npj Materials Degradation, 6*(1), 68. https://doi.org/10.1038/s41529-022-00277-7

Sanchez, F. A. C., Boudaoud, H., Hoppe, S., & Camargo, M. (2017). Polymer recycling in an open-source additive manufacturing context: Mechanical issues. *Additive Manufacturing, 17*, 87–105. https://doi.org/10.1016/j.addma.2017.05.013

Scaffaro, R., Citarrella, M. C., Catania, A., & Settanni, L. (2022). Green composites based on biodegradable polymers and anchovy (Engraulis Encrasicolus) waste suitable for 3D printing applications. *Composites Science and Technology, 230*, 109768. https://doi.org/10.1016/j.compscitech.2022.109768

Schoinochoritis, B., Chantzis, D., & Salonitis, K. (2017). Simulation of metallic powder bed additive manufacturing processes with the finite element method: A critical review. *Proceedings of the Institution of Mechanical Engineers, Part B: Journal of Engineering Manufacture, 231*(1), 96–117. https://doi.org/10.1177/0954405414567522

Šenkeřík, V., Bednařík, M., Janoštík, V., Karhankova, M., & Mizera, A. (2024). Analysis of extrusion process parameters in PLA filament production for FFF technology. *Manufacturing Technology*. https://doi.org/10.21062/mft.2024.037

Shanmugam, V., Das, O., Babu, K., Marimuthu, U., Veerasimman, A., Johnson, D. J., . . . Berto, F. (2021). Fatigue behaviour of FDM-3D printed polymers, polymeric composites and architected cellular materials. *International Journal of Fatigue, 143*, 106007. https://doi.org/10.1016/j.ijfatigue.2020.106007

Shanmugam, V., Rajendran, D. J. J., Babu, K., Rajendran, S., Veerasimman, A., Marimuthu, U., . . . Hedenqvist, M. S. (2021). The mechanical testing and performance analysis of polymer-fibre composites prepared through the additive manufacturing. *Polymer Testing, 93*, 106925. https://doi.org/10.1016/j.polymertesting.2020.106925

Sharifi, J., Rizvi, G., & Fayazfar, H. (2024). Sustainable 3D printing of enhanced carbon nanotube-based polymeric nanocomposites: green solvent-based casting for eco-friendly electrochemical sensing applications. *The International Journal of Advanced Manufacturing Technology, 131*(9), 4825–4837. https://doi.org/10.1007/s00170-024-13337-w

Sheikh, T., & Behdinan, K. (2023). Novel experimental and multiscale study of additively manufactured ABS-carbon nanotubes nanocomposites. *Applied Materials Today, 35*, 101963. https://doi.org/10.1016/j.apmt.2023.101963

Sheikh, T., & Behdinan, K. (2024). Parametric analysis of additively manufactured polymer nanocomposites: A experimental and multiscale study. *Journal of Manufacturing Processes, 117*, 193–204. https://doi.org/10.1016/j.jmapro.2024.03.007

Shofner, M., Rodríguez-Macías, F. J., Vaidyanathan, R., & Barrera, E. V. (2003). Single wall nanotube and vapor grown carbon fiber reinforced polymers processed by extrusion freeform fabrication. *Composites Part A: Applied Science and Manufacturing, 34*(12), 1207–1217. https://doi.org/10.1016/j.compositesa.2003.07.002

Singh, S., Singh, G., Prakash, C., Ramakrishna, S., Lamberti, L., & Pruncu, C. I. (2020). 3D printed biodegradable composites: An insight into mechanical properties of PLA/chitosan scaffold. *Polymer Testing, 89*, 106722. https://doi.org/10.1016/j.polymertesting.2020.106722

Siripongpreda, T., Hoven, V. P., Narupai, B., & Rodthongkum, N. (2023). Emerging 3D printing based on polymers and nanomaterial additives: enhancement of properties and potential applications. *European Polymer Journal, 184*, 111806. https://doi.org/10.1016/j.eurpolymj.2022.111806

Slavković, V., Hanželič, B., Plesec, V., Milenković, S., & Harih, G. (2024). Thermo-mechanical behavior and strain rate sensitivity of 3D-printed polylactic acid (PLA) below glass transition temperature (Tg). *Polymers, 16*(11), 1526. https://doi.org/10.3390/polym16111526

Song, Y., Li, Y., Song, W., Yee, K., Lee, K.-Y., & Tagarielli, V. L. (2017). Measurements of the mechanical response of unidirectional 3D-printed PLA. *Materials & Design, 123*, 154–164. https://doi.org/10.1016/j.matdes.2017.03.051

Sood, A. K., Ohdar, R. K., & Mahapatra, S. S. (2010). Parametric appraisal of mechanical property of fused deposition modelling processed parts. *Materials & Design, 31*(1), 287–295. https://doi.org/10.1016/j.matdes.2009.06.016

Šostakaitė, L., Šapranauskas, E., Rudinskas, D., Rimkus, A., & Gribniak, V. (2024). Investigating additive manufacturing possibilities for an unmanned aerial vehicle with polymeric materials. *Polymers, 16*(18), 2600. https://doi.org/10.3390/polym16182600

Spoerk, M., Holzer, C., & Gonzalez-Gutierrez, J. (2020). Material extrusion-based additive manufacturing of polypropylene: A review on how to improve dimensional inaccuracy and warpage. *Journal of Applied Polymer Science, 137*(12), 48545. https://doi.org/10.1002/app.48545

Stepashkin, A., Chukov, D., Senatov, F., Salimon, A., Korsunsky, A., & Kaloshkin, S. (2018). 3D-printed PEEK-carbon fiber (CF) composites: Structure and thermal properties. *Composites Science and Technology, 164,* 319–326. https://doi.org/10.1016/j.compscitech.2018.05.032

Stoof, D., Pickering, K., & Zhang, Y. (2017). Fused deposition modelling of natural fibre/polylactic acid composites. *Journal of Composites Science, 1*(1), 8. https://doi.org/10.3390/jcs1010008

Struzziero, G., Barbezat, M., & Skordos, A. A. (2021). Consolidation of continuous fibre reinforced composites in additive processes: A review. *Additive Manufacturing, 48,* 102458. https://doi.org/10.1016/j.addma.2021.102458

Syrlybayev, D., Zharylkassyn, B., Seisekulova, A., Perveen, A., & Talamona, D. (2021). Optimization of the warpage of fused deposition modeling parts using finite element method. *Polymers, 13*(21), 3849. https://doi.org/10.3390/polym13213849

Tammaro, L., Martone, A., Palmieri, B., Borriello, C., Portofino, S., Iovane, P., . . . Galvagno, S. (2024). Reinforcing efficiency of recycled carbon fiber PLA filament suitable for additive manufacturing. *Polymers, 16*(15), 2100. https://doi.org/10.3390/polym16152100

Tan, Z., Yi, Y., Wang, H., Zhou, W., Yang, Y., & Wang, C. (2016). Physical and degradable properties of mulching films prepared from natural fibers and biodegradable polymers. *Applied Sciences, 6*(5), 147. https://doi.org/10.3390/app6050147

Thakur, V., Singh, R., Kumar, R., Sharma, S., Singh, S., Li, C., . . . Alqarni, S. A. (2024). Mechanically sustainable and primary recycled thermo-responsive ABS–PLA polymer composites for 4D printing applications: fabrication and studies. *Reviews on Advanced Materials Science, 63*(1), 20230149. https://doi.org/10.1515/rams-2023-0149

Tian, X., Liu, T., Wang, Q., Dilmurat, A., Li, D., & Ziegmann, G. (2017). Recycling and remanufacturing of 3D printed continuous carbon fiber reinforced PLA composites. *Journal of Cleaner Production, 142,* 1609–1618. https://doi.org/10.1016/j.jclepro.2016.11.139

Tian, X., Liu, T., Yang, C., Wang, Q., & Li, D. (2016). Interface and performance of 3D printed continuous carbon fiber reinforced PLA composites. *Composites Part A: Applied Science and Manufacturing, 88,* 198–205. https://doi.org/10.1016/j.compositesa.2016.05.032

Tran, T. N., Bayer, I. S., Heredia-Guerrero, J. A., Frugone, M., Lagomarsino, M., Maggio, F., & Athanassiou, A. (2017). Cocoa shell waste biofilaments for 3D printing applications. *Macromolecular Materials and Engineering, 302*(11), 1700219. https://doi.org/10.1002/mame.201700219

Turner, B. N., & Gold, S. A. (2015). A review of melt extrusion additive manufacturing processes: II. Materials, dimensional accuracy, and surface roughness. *Rapid Prototyping Journal, 21*(3), 250–261. https://doi.org/10.1108/RPJ-02-2013-0017

Ulkir, O., Ertugrul, I., Ersoy, S., & Yağımlı, B. (2024). The effects of printing temperature on the mechanical properties of 3D-printed acrylonitrile butadiene styrene. *Applied Sciences, 14*(8), 3376. https://doi.org/10.3390/app14083376

Umerah, C. O., Kodali, D., Head, S., Jeelani, S., & Rangari, V. K. (2020). Synthesis of carbon from waste coconut shells and their application as filler in bioplast polymer filaments for 3D printing. *Composites Part B: Engineering, 202*, 108428. https://doi.org/10.1016/j.compositesb.2020.108428

Vălean, C., Marșavina, L., Mărghitaș, M., Linul, E., Razavi, N., & Berto, F. (2020). Effect of manufacturing parameters on tensile properties of FDM printed specimens. *Procedia Structural Integrity, 26*, 313–320. https://doi.org/10.1016/j.prostr.2020.06.040

Van Der Klift, F., Koga, Y., Todoroki, A., Ueda, M., Hirano, Y., & Matsuzaki, R. (2015). 3D printing of continuous carbon fibre reinforced thermo-plastic (CFRTP) tensile test specimens. *Open Journal of Composite Materials, 6*(1), 18–27. https://doi.org/10.4236/ojcm.2016.61003

van Huyssteen, D., Rivarola, F. L., Etse, G., & Steinmann, P. (2025). On mesh refinement procedures for polygonal virtual elements. *Applications in Engineering Science*, 100222. https://doi.org/10.1016/j.apples.2025.100222

Vaneker, T. (2017). Material extrusion of continuous fiber reinforced plastics using commingled yarn. *Procedia CIRP, 66*, 317–322. https://doi.org/10.1016/j.procir.2017.03.367

Varma, M. M. M., Baghel, P. K., & Raju, R. (2022). Additive manufacturing of thermosetting resins in-situ carbon fibers: a review. *Recent Advances in Materials and Modern Manufacturing: Select Proceedings of ICAMMM 2021*, 97–105. https://doi.org/10.1007/978-981-19-0244-4_11

Wiberg, A., Persson, J., & Ölvander, J. (2021). An optimisation framework for designs for additive manufacturing combining design, manufacturing and post-processing. *Rapid Prototyping Journal, 27*(11), 90–105. https://doi.org/10.1108/RPJ-02-2021-0041

Wissamitanan, T., Dechwayukul, C., Kalkornsurapranee, E., & Thongruang, W. (2020). Proper blends of biodegradable polycaprolactone and natural rubber for 3D printing. *Polymers, 12*(10), 2416. https://doi.org/10.3390/polym12102416

Wu, C.-S., Liao, H.-T., & Cai, Y.-X. (2017). Characterisation, biodegradability and application of palm fibre-reinforced polyhydroxyalkanoate composites. *Polymer Degradation and Stability, 140*, 55–63. https://doi.org/10.1016/j.polymdegradstab.2017.04.016

Wu, Y., An, C., & Guo, Y. (2023). 3D printed graphene and graphene/polymer composites for multifunctional applications. *Materials, 16*(16), 5681. https://doi.org/10.3390/ma16165681

Xie, J., Zhang, N., Guers, M., & Varadan, V. K. (2002). Ultraviolet-curable polymers with chemically bonded carbon nanotubes formicroelectromechanical system applications. *Smart Materials and Structures, 11*(4), 575. https://doi.org/10.1088/0964-1726/11/4/313

Xu, X., Thwe, M. M., Shearwood, C., & Liao, K. (2002). Mechanical properties and interfacial characteristics of carbon-nanotube-reinforced epoxy thin films. *Applied physics letters, 81*(15), 2833–2835. https://doi.org/10.1063/1.1511532

Xu, Y., Feng, Z., Gao, Y., Wu, C., Fang, J., Sun, G., . . . Li, Q. (2024). Topology optimization for additive manufacturing of CFRP structures. *International Journal of Mechanical Sciences, 269*, 108967. https://doi.org/10.1016/j.ijmecsci.2024.108967

Yadav, N., & Schledjewski, R. (2023). Review of in-process defect monitoring for automated tape laying. *Composites Part A: Applied Science and Manufacturing, 173*, 107654. https://doi.org/10.1016/j.compositesa.2023.107654

Yan, C., Hao, L., Xu, L., & Shi, Y. (2011). Preparation, characterisation and processing of carbon fibre/polyamide-12 composites for selective laser sintering. *Composites Science and Technology, 71*(16), 1834–1841. https://doi.org/10.1016/j.compscitech.2011.08.013

Yang, Y., Yang, B., Chang, Z., Duan, J., & Chen, W. (2023). Research status of and prospects for 3D printing for continuous fiber-reinforced thermoplastic composites. *Polymers, 15*(17), 3653. https://doi.org/10.3390/polym15173653

Yang, Z., Fu, K., Zhang, Z., Zhang, J., & Li, Y. (2022). Topology optimization of 3D-printed continuous fiber-reinforced composites considering manufacturability. *Composites Science and Technology, 230*, 109727. https://doi.org/10.1016/j.compscitech.2022.109727

Yang, Z., Wang, F., Dun, Y., & Li, D. (2025). Path-Based Discrete Modeling and Process Simulation for Thermoplastic Fused Deposition Modeling Technology. *Polymers, 17*(8), 1026. https://doi.org/10.3390/polym17081026

Yap, Y. L., Wang, C., Sing, S. L., Dikshit, V., Yeong, W. Y., & Wei, J. (2017). Material jetting additive manufacturing: An experimental study using designed metrological benchmarks. *Precision engineering, 50,* 275–285. https://doi.org/10.1016/j.precisioneng.2017.05.015

Young, D., Wetmore, N., & Czabaj, M. (2018). Interlayer fracture toughness of additively manufactured unreinforced and carbon-fiber-reinforced acrylonitrile butadiene styrene. *Additive Manufacturing, 22,* 508–515. https://doi.org/10.1016/j.addma.2018.02.023

Yu, B., Chen, G., Sun, J., Hua, W., Wu, W., Jin, Y., . . . Zheng, W. (2025). Finite Element Analysis of Warping and Mechanical properties of 3D parts printed by fused deposition modeling. *Journal of Materials Engineering and Performance, 34*(3), 2410–2423. https://doi.org/10.1007/s11665-024-09243-7

Yu, T., Zhang, Z., Song, S., Bai, Y., & Wu, D. (2019). Tensile and flexural behaviors of additively manufactured continuous carbon fiber-reinforced polymer composites. *Composite Structures, 225,* 111147. https://doi.org/10.1016/j.compstruct.2019.111147

Zaldivar, R. J., McLouth, T. D., Patel, D. N., Severino, J. V., & Kim, H. I. (2017). Strengthening of plasma treated 3D printed ABS through epoxy infiltration. *Progress in Additive Manufacturing, 2*(4), 193–200. https://doi.org/10.1007/s40964-017-0032-0

Zhang, N., Huang, D., Chen, X., Ye, C., Li, B., Zhu, S., . . . Liu, J. (2023). Improving the interlaminar bonding and thermal conductivity of polymer composites by using split-radial mesophase pitch-based carbon fiber as reinforcement. *Composites Part B: Engineering, 252,* 110509. https://doi.org/10.1016/j.compositesb.2023.110509

Zhang, Q., Cai, H., Zhang, A., Lin, X., Yi, W., & Zhang, J. (2018). Effects of lubricant and toughening agent on the fluidity and toughness of poplar powder-reinforced polylactic acid 3D printing materials. *Polymers, 10*(9), 932. https://doi.org/10.3390/polym10090932

Zhang, W., Cotton, C., Sun, J., Heider, D., Gu, B., Sun, B., & Chou, T.-W. (2018). Interfacial bonding strength of short carbon fiber/acrylonitrile-butadiene-styrene composites fabricated by fused deposition modeling. *Composites Part B: Engineering, 137,* 51–59. https://doi.org/10.1016/j.compositesb.2017.11.018

Zhang, Y., & Chou, K. (2008). A parametric study of part distortions in fused deposition modelling using three-dimensional finite element analysis. *Proceedings of the Institution of Mechanical Engineers, Part B: Journal of Engineering Manufacture, 222*(8), 959–968. https://doi.org/10.1243/09544054JEM990

Zhang, Y., & Chou, Y. (2006). Three-dimensional finite element analysis simulations of the fused deposition modelling process. *Proceedings of the Institution of Mechanical*

Engineers, Part B: Journal of Engineering Manufacture, 220(10), 1663–1671. https://doi.org/10.1243/09544054JEM572

Zhang, Y., Qiao, J., Zhang, G., Li, Y., & Li, L. (2021). Prediction of deformation and failure behavior of continuous fiber reinforced composite fabricated by additive manufacturing. *Composite Structures, 265*, 113738. https://doi.org/10.1016/j.compstruct.2021.113738

Zhao, D. X., Cai, X., Shou, G. Z., Gu, Y. Q., & Wang, P. X. (2016). Study on the preparation of bamboo plastic composite intend for additive manufacturing. *Key Engineering Materials, 667*, 250–258. https://doi.org/10.4028/www.scientific.net/KEM.667.250

Zhao, P., Rao, C., Gu, F., Sharmin, N., & Fu, J. (2018). Close-looped recycling of polylactic acid used in 3D printing: An experimental investigation and life cycle assessment. *Journal of Cleaner Production, 197*, 1046–1055. https://doi.org/10.1016/j.jclepro.2018.06.275

Zhao, X. G., Hwang, K.-J., Lee, D., Kim, T., & Kim, N. (2018). Enhanced mechanical properties of self-polymerized polydopamine-coated recycled PLA filament used in 3D printing. *Applied Surface Science, 441*, 381–387. https://doi.org/10.1016/j.apsusc.2018.01.257

List of scientific publications by the author on the topic of the dissertation

Papers in the Reviewed Scientific Journals

Rimkus, A., Farh, M. M., & Gribniak, V. (2022). Continuously reinforced polymeric composite for additive manufacturing—Development and efficiency analysis. *Polymers, 14*(17), 3471. https://doi.org/10.3390/polym14173471

Farh, M. M., & Gribniak, V. (2025). Thermo-mechanical approach to material extrusion process during fused filament fabrication of polymeric samples. *Materials, 18*(19), 4537. https://doi.org/10.3390/ma18194537

Farh, M. M., Rimkus, A., Meškėnas, A., & Gribniak, V. (2026). Recent advancements in the additive manufacturing of fiber-reinforced polymeric composites. *Reviews on Advanced Materials Science, 65*(1), 20250228. https://doi.org/10.1515/rams-2025-0228

Papers in Other Editions

Farh, M., Abdelkader, M., & Gribniak, V. (2024). Numerical simulation of fused filament fabrication process and tensile tests. In *Proceedings of the 35th DAAAM International Symposium* (pp. 24–25). https://doi.org/10.2507/35th.daaam.proceedings.004

Summary in Lithuanian

Įvadas

Problemos formulavimas

Spartėjanti 3D spausdinimo (angl. *fused filament fabrication*, FFF) plėtra didina susidomėjimą šios technologijos taikymu. Vis dėlto jos taikymą konstrukcinėms funkcijoms riboja ryški spausdintų medžiagų anizotropija ir gamybos metu susidarantys mikrostruktūros defektai bei liekamieji įtempiai, lemiantys geometrinių matmenų netikslumus ir formos iškraipymus. Šie apribojimai dar labiau išryškėja, kai į gamybos ciklą siekiama įtraukti tvarumo principus, įskaitant dalinai perdirbtų polimerų naudojimą, todėl būtina įvertinti, kaip medžiagos sudėtis ir spausdinimo režimai lemia struktūrą bei gaminių mechaninį atsparumą. Vystant armavimo metodus, taikytinus 3D spausdinimui, t. y. trumpų plaušų užpildą ir ištisines armuojančias gijas, atsiveria galimybės gerinti mechanines savybes, tačiau kartu ryškėja plaušų pasiskirstymo netolygumo, sąveikos su polimero matrica ir struktūrinių defektų susidarymo rizikos. Todėl būtina sukurti vieningą metodinį pagrindą, kuris susietų medžiagos parinkimą (įskaitant perdirbtų plastikų taikymą), pasirinktą armavimo būdą, mikrostruktūros formavimosi ypatumus, viskoelastines, termomechanines ir mechanines savybes bei gamybos metu atsirandančių liekamųjų deformacijų ir įtempių modeliavimą. Toks kompleksinis požiūris sudaro prielaidas patikimai vertinti 3D spausdintų kompozitų konstrukcinį panaudojimą ir geometrinį tikslumą.

Darbo aktualumas

Disertacija yra aktuali tiek mokslinei, tiek pramonininkų bendruomenei, nes joje nagrinėjama trijų šiuolaikinių tendencijų sankirta: 3D spausdinimo būdu gaminamų pluoštu armuotų polimerinių kompozitų plėtra, tvarių polimerų perdirbimo ir panaudojimo sprendimų poreikis ir didėjanti procesų analizės svarba siekiant mažinti bandymų ir klaidų apimtį. Didėjantis trumpų plaušų armuotų polimero siūlų prieinamumas ir pažanga integruojant ištisinį armuojantį pluoštą sudaro sąlygas gaminti mechaniškai atsparesnius 3D spausdintus elementus. Taip pat išryškina didesnį poreikį vertinti plaušo ir matricos sąveiką, spausdinimo sluoksnių sukibimo kokybę ir jautrumą struktūriniams defektams. Eksperimentinis nearmuoto perdirbto polilaktido (PLA) vertinimas prisideda prie tvarumo siekių įgyvendinimo gamyboje, nes leidžia pagrįsti tokios medžiagos taikymą, kai būtina patikrinti jos mechaninį patikimumą. Ištisinių pluoštų armavimas leidžia išplėsti PLA pagrindu gaminamų komponentų mechaninių savybių spektrą, ženkliai pranokstantį įprastinių polimerų galimybes. Galiausiai, termomechaninių procesų analizė dar labiau sustiprina tyrimų potencialą, nes padeda atskleisti, kaip liekamosios deformacijos ir įtempiai, atsirandantys gamybos metu, veikia 3D spausdintų detalių matmenų tikslumą ir struktūrinį patikimumą.

Tyrimo objektas

3D spausdintų PLA pagrindu sudarytų trumpų plaušų ir ištisinio pluošto armuotų kompozitų mechaninės ir temperatūrai jautrias viskoelastinės savybės, taip pat gamybos metu susidarantys liekamosios deformacijos ir įtempiai.

Darbo tikslas

Sukurti eksperimentinę ir skaitinio modeliavimo metodiką, leidžiančią įvertinti PLA pagrindo armuotų kompozitų mechaninį atsparumą ir nustatyti 3D spausdinimo metu atsirandančias deformacijas bei liekamųjų įtempių pokyčius.

Darbo uždaviniai

Siekiant įgyvendinti tyrimo tikslą, disertacijoje sujungta literatūros analizė, eksperimentiniai tyrimai, medžiagų charakterizavimas ir baigtinių elementų modeliavimas. Remiantis šiomis tyrimų kryptimis, suformuluoti šie uždaviniai:

1. Nustatyti armavimo tipo (ištisinio ir trumpų plaušų) bei medžiagos sudėties, įskaitant perdirbto PLA dalį, įtaką 3D spausdintų PLA elementų mechaninėms savybėms, įvertinant jų stiprį, standumą ir irimo elgseną.
2. Ištirti gamybos proceso, medžiagos struktūros ir PLA bei jo kompozitų savybių sąsajas, analizuojant kristalizavimo lygį, viskoelastines savybes, termomechanines reakcijas ir mikrostruktūros ypatumus (plaušų pasiskirstymą, sąsajos kokybę, defektų susidarymą) bei identifikuoti pagrindinius kompozitų irimo ir pleišėjimo mechanizmus.
3. Sukurti ir eksperimentiškai patikrinti kombinuotą termomechaninį skaitinį (baigtinių elementų) modelį, nustatantį 3D spausdinimo, aušinimo ir atskyrimo nuo

pagrindo metu susidarančias liekamąsias deformacijas, įtempius ir bandinių išlinkį, taip pat DIGIMAT aplinkoje įvertinti trumpais plaušais armuotų kompozitų išlinkio tendencijas bei modeliavimo ir eksperimentinių bandymų atitikimą.

Tyrimo metodai

Tyrimo objektui nagrinėti taikyta teorinė analizė ir sintezė, kurių metu nustatytas tyrimo kontekstas ir suformuotas vieningas tyrimų pagrindas, siejantis armavimo būdą, 3D spausdinimo šiluminio režimo įtaką, spausdintos medžiagos mikrostruktūrą, mechanines savybes, geometrinės formos pokyčius ir 3D spausdinimo proceso skaitinį modeliavimą. Eksperimentinio tyrimo planavimas ir gamybos parametrų parinkimas buvo grindžiami laboratorine 3D spausdinimo praktika ir polimerinių kompozitų mechaninių bandymų standartais. Kvazistatiniai tempimo bandymai atlikti siekiant nustatyti mechaninį atspausdintų bandinių atsaką, o ištisinės gijos armavimo atveju deformacijoms registruoti taikytas skaitmeninės vaizdų koreliacijos (DIC) metodas. Trumpų plaušų armuotiems kompozitams įvertinti taikyti kvazistatiniai tempimo ir trijų taškų lenkimo bandymai, nustatant jų stiprį, plastiškumą ir tąsumą. Diferencialinė skenuojančioji kalorimetrija (DSC) ir dinaminė mechaninė analizė (DMA) naudotos terminio virsmo charakteristikoms ir temperatūrai jautraus kompozitų standumo pokyčiams nustatyti. Skenuojančioji elektroninė mikroskopija (SEM) taikyta gijų skerspjūviui ir irimo paviršiams tirti, identifikuojant plaušų pasiskirstymą, sąsajos kokybę ir susidariusius defektus. Kombinuotas termomechaninis baigtinių elementų modelis buvo taikytas grynajam PLA: modeliuoti spausdinimo, aušinimo ir atskyrimo nuo pagrindo etapai, prognozuoti liekamieji įtempiai, bandinių išlinkis ir liekamųjų deformacijų bei įtempių eksportavimas į mechaninio tempimo bandymo modelį. DIGIMAT aplinkoje sudarytas skaitinis modelis taikytas trumpų plaušų armuotiems kompozitams, siekiant įvertinti išlinkio tendencijas ir palyginti modeliavimo bei eksperimentinių bandymų rezultatus.

Darbo mokslinis naujumas

Eksperimentiniai ir skaitinio modeliavimo 3D spausdintų elementų tyrimai leidžia išskirti šiuos disertacijos mokslo naujumo aspektus:

1. Kombinuotas SEM, DSC ir DMA taikymas leidžia pateikti vientisą trumpų plaušų armuotų PLA kompozitų struktūros ir savybių sąsajų interpretaciją. Šis kombinuotas tyrimas atskleidė skirtingą plaušo tipo įtaką kristalizavimuisi, viskoelastinėms savybėms ir mikrostruktūrinei sandarai: 30 % medienos plaušų užpildas padidina kristalizavimo lygį, tąsumą ir matmenų pastovumą, o 10 % anglies plaušų įtaka pasireiškia per standumo pokyčius ir plaušų ir PLA matricos sukibimo defektų sukeltus irimo mechanizmus.
2. Sukurtas kombinuotas termomechaninis modeliavimo pagrindas, leidžiantis eksportuoti 3D spausdinimo metu atsirandančių liekamųjų įtempių ir formos pokyčių laukus į mechaninį baigtinių elementų modelį. DSC ir DMA tyrimų metu nustatytos terminio virsmo temperatūros ir standumo pokyčiai sudarė temperatūrai priklausomus medžiagų modelius. Tai leido apibrėžti liekamųjų įtempių

prieaugį ir nustatyti bandinių atskyrimo nuo pagrindo metu gamybos metu susidarančių deformacijų pokyčius.

3. DIGIMAT aplinkoje sukurtas trumpų plaušų armuotų PLA kompozitų homogenizavimo modelis yra pirmasis tokio tipo skaitinis modelis, skirtas 3D spausdinimo metu atsirandančioms deformacijoms nustatyti. Šis modelis leidžia įvertinti deformacijų dydį ir jų priklausomybę nuo kompozito sudėties bei plaušo tipo, esant 3D spausdinimo proceso sukeltoms termomechaninėms apkrovoms.

Darbo rezultatų praktinė reikšmė

Šio darbo rezultatai turi praktinę vertę tiek 3D spausdinimo technologijų tobulinimui, tiek taikomajam kompozitų projektavimui:

1. Pademonstruotas ištisinės aramido gijos armavimo pritaikomumas gali būti laikomas praktine nuoroda, skirta išplėsti PLA pagrindu gaminamų elementų mechaninį atsparumą naudojant įprastas vieno ekstruderio 3D spausdinimo sistemas. Taip pat nustatyti technologiniai apribojimai – gijos įtempimo stoka, trajektorijų tęstinumo poreikis ir sukibimo defektai, atsiradusieji spausdinimo metu, pademonstravo veiksnius, ribojančius ištisinio armavimo efektyvumą ir pakartojamumą.
2. Gauti eksperimentiniai duomenys apie spausdintų PLA elementų tempiamo savybes, pagamintas kontroliuojant 3D spausdinimo režimus, įskaitant palyginimą tarp gryno ir perdirbto polilaktido. Šie rezultatai sudaro pagrindą spausdinimo žaliavų praktiniam taikymui ir mechaninių savybių vertinimui tvarumo kontekste.
3. Derinant mechaninių bandymų ir SEM mikrostruktūros tyrimų rezultatus paprastam PLA ir trumpais plaušais armuotiems kompozitams nustatytas ryšys tarp trumpų plaušų poveikio standumui, stipriui ir tąsumui, taip pat parodyta, kaip plaušų sukibimo defektai ir jų pasiskirstymas riboja šių kompozitų mechaninį atsparumą.
4. DSC ir DMA tyrimai pateikia duomenų apie temperatūrai jautrias medžiagų savybes, svarbias skaitiniam modeliavimui 3D spausdinimo procesų metu, identifikuojant kristalizacijos bei standumo pokyčius ir jų įtaką komponentams, veikiamiems temperatūrų, artimų medžiagos stiklėjimo sričiai. Gauti eksperimentiniai duomenys būtini termomechaniniams modeliams kalibruoti, siekiant patikimai prognozuoti gamybos (medžiagos lydimo, ekstruzijos ir aušinimo procesų) liekamąsias deformacijas ir įtempius.
5. Sukurtas kombinuotas 3D spausdinimo termomechaninis modelis, įgyvendintas ABAQUS aplinkoje, leidžia įvertinti deformacijas ir liekamuosius įtempius atsižvelgiant į gamybos etapų seką – medžiagos ekstruziją, aušinimą ir atskyrimą nuo formavimo pagrindo. Nustatyta, kad būtent atskyrimo etapas lemia sukauptų įtempių išlaisvinimą ir gali nutraukti gamybą. Šis modelis leidžia identifikuoti išlinkiui jautrias formas ir nustatyti saugius proceso parametrus, taip sumažinant eksperimentinių bandymų poreikį.

6. PYTHON aplinkoje sukurtas automatizuotas įrankis, skirtas 3D spausdinimo kodui (G-kodas) transformuoti į laike išdėstytą įvykių seką, skirtą baigtiniams elementams aktyvuoti skaitiniame modelyje. Šis algoritmas sumažina modeliavimo paruošimo laiką ir eliminuoja žmogiškąsias klaidas.
7. DIGIMAT aplinkoje sudarytas termomechaninis trumpais plaušais armuotų PLA kompozitų modelis leidžia įvertinti medžiagų savybėmis nulemtas ir 3D spausdinimo aktyvuotos geometrinės formos praradimo tendencijas ir palyginti deformacijų skirtumus priklausomai nuo užpildo tipo. Nustatyta, kad medienos plaušais armuotas PLA kompozitas pasižymi mažiausiu formos praradimu, o jo taikymas gali sumažinti formos nuokrypius, taip užtikrinant gamybos preciziškumą. Be to, medienos plaušų ir PLA derinys gali būti laikomas potencialiai bioskaidomu ir aplinkai palankiu kompozitu.

Ginamieji teiginiai

Šie disertacijos rezultatais pagrįsti teiginiai sudaro ginamąją darbo hipotezę:

1. Sukurta ištisai armuota PLA gija, kurioje įterpta ištisinė aramido gija, yra suderinama su įprastomis vieno ekstruderio 3D spausdinimo sistemomis. Tačiau armavimas negali pasiekti teorinio efektyvumo, nes spausdinimo procesas neužtikrina armavimo gijos įtempimo ir geometrinio gaminio tikslumo.
2. Trumpų plaušų armavimas mažina liekamąjį išlinkį ir geometrijos netikslumus 3D spausdintuose PLA kompozituose. Medienos plaušai skatina polimero kristalizavimo procesą ir didina tąsumą, o anglies plaušai didina standumą. Abu plaušų tipai leidžia užtikrinti spausdintų objektų matmenų pastovumą, tačiau tik medienos plaušas pasižymi tvarumu.
3. Sukurtas kombinuotas termomechaninis 3D spausdinimo modeliavimo sprendinys leidžia nustatyti liekamąsias deformacijas ir įtempius grynajame ir trumpais plaušais armuotame PLA. Automatinis 3D spausdinimo proceso algoritmo transformavimas į ABAQUS baigtinių elementų tinklą sudaro galimybę įvertinti spausdinimo metu susidarančius įtempių būvius elementuose.

Darbo rezultatų aprobavimas

Tyrimo tematika parengtos keturios mokslinės publikacijos, iš kurių trys paskelbtos *Web of Science* duomenų bazėje referuojamuose mokslo žurnaluose, turinčiuose citavimo rodiklius.

Disertacijoje pristatytų tyrimų rezultatai paskelbti septyniose mokslinėse konferencijose:

- NUMIFORM 2023: *14th International Conference on Numerical Methods in Industrial Forming Processes* pranešimas *Numerical Simulation of Polymer Extrusion-Based Additive Manufacturing Process,* 2023 m., Krokuvoje, Lenkijoje.
- *35th DAAAM International Symposium on Intelligent Manufacturing and Automation* pranešimas *Numerical Simulation of FFF Process and Tensile Tests,* 2024 m., Vienoje, Austrijoje.

- OES 2025: *2nd Olympiad in Engineering Science International Conference* pranešimas *Thermo-Mechanical Simulation of Material Extrusion-Based Additive Manufacturing Process,* 2025 m., Stavangeryje, Norvegijoje.
- Pranešimas *Development and Mechanical Performance Analysis of Biodegradable Polymers Sustainable for Additive Manufacturing* Stambulo universiteto seminare, 2025 m., Stambule, Turkijoje.

Disertacijos struktūra

Pagrindinę disertacijos dalį sudaro trys skyriai ir bendrosios išvados. Literatūros sąrašą sudaro 280 šaltiniai. Disertacijos apimtis (be santraukos lietuvių kalba) yra 135 puslapiai, joje pateikiamos 35 iliustracijos, 14 lentelių ir 17 sunumeruotų lygčių. Autoriaus publikacijų sąrašą sudaro trys straipsniai *Web of Science* domenų bazėje referuojamuose žurnaluose ir viena publikacija tarptautinės konferencijos leidinyje.

Padėkos

Autorius nuoširdžiai dėkoja darbo vadovui prof. dr. Viktorui Gribniak už neįkainojamą pagalbą, pastangas ir intelektinę paramą viso studijų laikotarpio metu. Taip pat reiškiama padėka doc. dr. Arvydui Rimkui už konstruktyvias įžvalgas ir pagalbą organizuojant eksperimentinius tyrimus.

Autorius dėkingas doc. dr. Jelenai Škamat, prof. dr. Dariui Bačinskui, prof. dr. Alfonsui Daniūnui, prof. dr. Artūrui Juknai, doc. dr. Nikolajui Višniakov ir prof. dr. Dimitrios Pavlou už jų indėlį gerinant šios disertacijos kokybę.

Autorius taip pat nuoširdžiai dėkoja savo šeimos nariams ir draugams. Jų nuolatinė emocinė parama suteikė motyvacijos ir stiprybės viso studijų proceso metu.

1. Pluoštu armuotų polimerinių kompozitų adityvioji gamyba

Šiame skyriuje pateikiama pluoštu armuotų polimerinių kompozitų adityviosios gamybos literatūros apžvalga, skiriant dėmesį 3D spausdinimui (angl. *fused filament fabrication,* FFF). Analizuojamos pagrindinės tyrimų kryptys, susijusios su polilaktido (PLA) pagrindu gaminamomis medžiagomis, įskaitant gryną ir perdirbtą PLA, taip pat trumpais plaušais ir ištisinėmis gijomis armuotus kompozitus. Apžvelgiami būdai, kaip galima įvesti ištisinę aramido armuojančią giją į spausdinamą medžiagą ir užtikrinti plaušų arba gijų suderinamumą su polimero matrica. Be to, aptariama polimero kristalizavimo procesai, poringumo susidarymo ir sukibimo defektų, atsirandančių spausdinimo metu, poveikis spausdintų kompozitų mechaninėms savybėms ir jų anizotropijai.

Taip pat aptariamas 3D spausdinimo šiluminio režimo poveikis liekamosioms deformacijoms ir įtempiams, kurie sukelia geometrinės formos pokyčius. Pabrėžiama, kad dauguma esamų skaitinių modelių vertina medžiagos formavimo ir aušinimo etapus, tačiau jų galimybės aprašyti galutinį gaminio atskyrimą nuo gamybos pagrindo, kuris yra lemiamas liekamųjų deformacijų veiksnys, yra ribotos. Šis neatitikimas riboja galimybę tiksliai nustatyti spausdinimo metu sukeltus geometrijos netikslumus.

Skyrius pabrėžia poreikį sistemingai tirti sąsajas tarp medžiagos sudėties, trumpų plaušų arba ištisinės gijos armavimo, spausdinimo parametrų, spausdintų dalių mikrostruktūros ir mechaninių savybių. Nustatyti pagrindiniai neišspręsti klausimai, kurie tapo šios disertacijos tikslo ir uždavinių pagrindu.

2. Medžiagos, metodai ir tyrimo metodika

Šiame skyriuje pateikiama kombinuota eksperimentinių ir skaitinio modeliavimo metodika, skirta PLA pagrindu gaminamų medžiagų savybėms įvertinti, įskaitant gryną, perdirbtą (40 % PLA pakeitimas perdirbtu plastiku) ir pluoštu armuotus kompozitus. Šis skyrius sieja medžiagos formavimo procesą ir mechaninį atsparumą, sujungdamas fizikinių medžiagų savybių nustatymą su skaitiniu termomechaniniu 3D spausdinimo proceso modeliavimu. Nagrinėjama priklausomybė tarp kompozito mechaninių savybių ir 3D spausdinimo kokybės. Tyrimas suskirstytas į dvi dalis. Pirmojoje dalyje nagrinėjamas ištisinės gijos armavimas, siekiant padidinti spausdintos medžiagos atsparumą tempimui. Kiekybiškai įvertinamas skirtumas tarp teorinio aramido gijos armavimo potencialo (laikomosios galios) ir eksperimentiškai pasiektų savybių bei nustatomas armavimo efektyvumas. Antrojoje skyriaus dalyje vertinami trumpais anglies (PLA-CF) ir medienos (PLA-WF) plaušais armuoti kompozitai, analizuojant jų gebėjimą gerinti tąsumą ir sumažinti geometrinės formos pokyčius.

Pirmojoje skyriaus dalyje aprašoma eksperimentinė medžiagų tyrimų programa. S2.1 lentelėje pateiktas bandinių ir jų gamybos parametrų apibendrintas planas visoms tirtoms medžiagoms.

S2.1 lentelė. Tirtų medžiagų gamybos parametrai

Medžiaga	Geometrijos standartas	Spausdinimo greitis	Temperatūra		Užpildymo tankis	Spausdinimo kryptys	Ekstruderio skersmuo	Bandinių skaičius
			Ekstruzijos	Platformos				
		(mm/s)	(°C)	(°C)	(%)	(°)	(mm)	(-)
cAFR-PLA 22 tūr. % (In.LT)	ASTM D3039	10	210	60	100	±45	0,8	5
40% perdibtas-PLA (In.LT)	ASTM D638-14	28	210	60	100	±45	0,4	6
PLA (In.LT)	ASTM D638-14, D3039	28	210	60	100	±45	0,4	11
PLA (Pr.CZ)	ASTM D638-14	28	210	60	100	±45	0,4	6
PLA (Po.TR)	ASTM D638-14, D790	30	215	60	20, 60, 100	±45	0,4	6, 6, 6
PLA-CF 10 masės % (Po.TR)	ASTM D638-14, D790	30	215	60	20, 60, 100	±45	0,4	6, 6, 6
PLA-WF 30 masės % (Po.TR)	ASTM D638-14, D790	30	215	60	20, 60, 100	±45	0,4	6, 6, 6

Pastaba: cAFR-PLA – ištisine aramido gija armuotas PLA; (In.LT), (Pr.CZ) ir (Po.TR) nurodo gamintojus „Inorega Ltd.“ (Lietuva), „Prusa“ (Čekija) ir „Porima3D“ (Turkija).

Ištisinės gijos armuotų PLA bandinių atsparumas vertinamas atliekant tempimo bandymus pagal ASTM standartus (ASTM International, 2017); trumpų anglies ir medienos plaušų armuotiems kompozitams atliekami tempimo ir trijų taškų lenkimo bandymai, leidžiantys nustatyti atsparumą tempimui, lenkimo stiprį, plastiškumą ir tąsumą. Šie mechaniniai bandymai atliekami kartu su mikrostruktūros (SEM) ir terminiais tyrimais: DSC naudotas kristalizavimo lygiui nustatyti, o DMA – temperatūrai jautrioms viskoelastinėms savybėms įvertinti.

Antrojoje skyriaus dalyje aprašomas kombinuotas termomechaninis skaitinis modelis, sudarytas ABAQUS aplinkoje grynam PLA. Šis modelis skirtas liekamosioms deformacijoms ir geometrijos pokyčiams nustatyti. Siekiant atkurti medžiagos formavimo (3D spausdinimo) seką, sukurtas automatizuotas spausdinimo kodo (G-kodo) transformavimo algoritmas, kuris konvertuoja spausdinimo trajektorijas į laike išdėstytų įvykių seką, skirtą baigtiniams elementams aktyvuoti skaitiniame modelyje. Modeliavimas apima tris esminius 3D spausdinimo etapus: medžiagos klojimą, aušinimą ir gaminio atskyrimą nuo pagrindo.

Termomechaninis modeliavimas buvo išplėstas įtraukiant trumpų plaušų armuotus PLA kompozitus. DIGIMAT-AM darbo aplinkoje ASTM D638 I tipo bandinio geometrija buvo sugeneruota kaip STL failas ir parengta ULTIMAKER CURA programoje G-kodui (3D spausdinimo trajektorijų) sukurti. Spausdinimo modelis sudarytas naudojant 100 % užpildą ir ±45° rastrinę užpildo struktūrą, keičiant jos kryptį tarp sluoksnių; nustatytas 30 mm/s spausdinimo greitis ir 215 °C ekstruzijos temperatūra. Pirmasis sluoksnis formuotas 0,2 mm, o tolesni – 0,3 mm storiu, išgaunant maždaug 3,2 mm storio bandinį. Atskirų plaušų geometrija nebuvo modeliuojama – tam taikytas homogeninis DIGIMAT-MF trumpų plaušų armuoto polimero modelis. Spausdinimo duomenys (geometrija ir trajektorijos) importuoti į DIGIMAT-AM aplinką, siekiant adekvačiai perteikti gijos išdėstymą, aušinimą ir deformaciją, kartu mažinant skaičiavimo sąnaudas.

DIGIMAT-AM aplinkos baigtinių elementų tinklas skiriasi nuo ABAQUS tuo, kad yra pagrįstas vokseliniu (angl. *voxel-based*) diskretizavimu, kuriame modeliuojamas objektas vaizduojamas struktūrizuotu tinklu. Kaip ir ABAQUS, tinklui sudaryti naudojami kubo formos baigtiniai elementai. Toks diskretizavimo būdas supaprastina automatinį spausdinimo trajektorijos susiejimą su modeliu ir padidina sudėtingų formavimo trajektorijų modeliavimo patikimumą. Vis dėlto lokalių gradientų nustatymą riboja daugiausia vokselio dydis, o ne tinklelio sutankinimas. Tuo tarpu ABAQUS naudojami tetraedriniai arba heksaedriniai baigtinių elementų tinklai reikalauja lokalaus sutankinimo didelių gradientų zonose, kas padidina modeliavimo tikslumą, tačiau lemia gerokai didesnes skaičiavimo sąnaudas.

3. Mechaninių savybių ir gamybos proceso sukeltų deformacijų charakterizavimas bei modeliavimas

Šiame skyriuje pateikiami eksperimentinių ir skaitinio modeliavimo rezultatai, skirti nustatyti medžiagos pasirinkimo, armavimo būdo ir 3D spausdinimo režimų poveikį spausdintų PLA elementų mechaniniam atsparumui ir geometrinės formos pokyčiams. Rezultatai apjungia tempimo ir lenkimo bandymus, termines ir viskoelastines savybių nustatymo rezultatus, mikrostruktūros tyrimus bei termomechaninį modeliavimą, pristatytą antrajame disertacijos skyriuje.

Ištisinės gijos armavimas. Naudojant vieno ekstruderio 3D spausdintuvą ir iš anksto impregnuotą aramido giją, pavyko beveik dvigubai, palyginant su nearmuotais bandiniais, padidinti armuoto PLA elementų atsparumą tempimui. Tačiau armavimo efektyvumą riboja keli gamybos veiksniai: aramido gijos sukibimo su PLA matrica defektai atspausdintame bandinyje, gijos išdėstymo trajektorijos netolygumas, spausdintų elementų geometriniai netikslumai ir sukibimo tarp spausdinimo sluoksnių defektai. Taip pat nepavyko užtikrinti bandinio numatytos geometrinės formos. Šių apribojimų pasekmės atsispindėjo baigtinių elementų modelio tempimo modeliavimo rezultatuose: teorinė laikomoji galia buvo gerokai didesnė nei eksperimentiškai užfiksuotos reikšmės (S3.1 pav.).

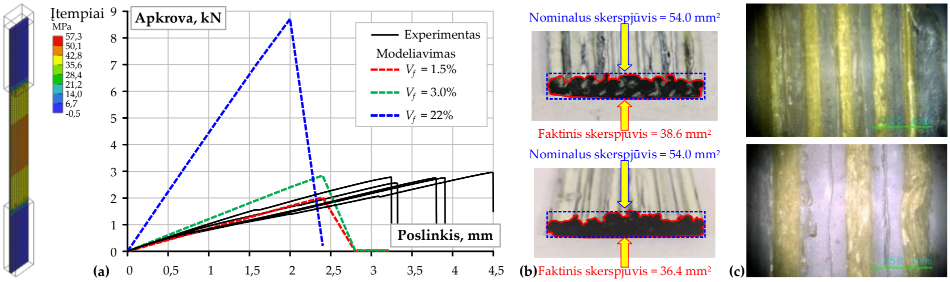

S3.1 pav. Tempimo bandymo ir geometrines formos stebėjimo rezultatai: (a) apskaičiuotas įtempių pasiskirstymas ir armavimo efektyvumo vertinimas; (b) spausdinimo metu susidarę skerspjūvio defektai; (c) ištisinės gijos armuoto bandinio vaizdai esant skirtingiems didinimo masteliams

Šio neatitikimo priežastys siejamos su ribotomis ištisinės gijos armavimo formavimo galimybėmis: poreikiu išlaikyti nenutrūkstamas spausdinimo trajektorijas, sudėtingu gijos išdėstymu sudėtingos formos objektuose, gijos įtempimo stoka spausdinant elementus bei gijos sukibimo defektais. Dėl to realus mechaninis atsakas stipriai priklauso nuo gamybos nustatymų ir spausdinimo mastelio yra ribotas.

Trumpų plaušų armuoti kompozitai. Detalėse su 100 % spausdinimo užpildymu trumpais plaušais armuotų PLA kompozitų mechaninės savybės nepasiekia gryno PLA stiprio ir standumo, iš vienos pusės, ir pranoksta PLA plastiškumą bei tąsumą – iš kitos. Grynas PLA pasižymėjo didžiausiu tempiamuoju stipriu (39,9 MPa) ir tamprumo moduliu (2,08 GPa), o PLA-WF pasiekė didžiausias pailgėjimo deformacijas (5,60 ± 0,70 %) ir didžiausią irimo energiją (1268 kJ/m³). S3.1 lentelėje pateikiama tempiamųjų bandymų rezultatų suvestinė.

S3.1 lentelė. Tempimo bandymo rezultatų suvestinė

Medžiaga	Tamprumo modulis	Tempiamasis stipris	Ribinė deformacija	Tąsumas
	(GPa)	(MPa)	(%)	(kJ/m³)
PLA	2,08 ± 0,15	39,9 ± 2,10	3,87 ± 0,45	813
PLA-CF	1,92 ± 0,02	27,2 ± 0,20	4,45 ± 0,05	985
PLA	1,38 ± 0,03	24,1 ± 0,60	5,60 ± 0,70	1268

DSC rezultatai parodė, kad anglies ir medienos plaušų taikymas labiau keičia PLA kristališkumo laipsnį (X_c) nei stiklėjimo temperatūrą (T_g). Trumpi plaušai veikia kaip kristalizavimo židiniai ir riboja polimero grandinės difuziją, slopindami kristalų augimą. S3.2 lentelėje pateiktos DSC savybės.

S3.2 lentelė. DSC terminės savybės

Medžiaga	Pirmas kaitinimas						Aušinimas	Antras kaitinimas					
	T_g	T_{cc}	ΔH_{cc}	T_m	ΔH_m	X_c	T_g	T_g	T_{cc}	ΔH_{cc}	T_m	ΔH_m	X_c
	°C		J/g	°C	J/g	%	°C	°C		J/g	°C	J/g	%
PLA	60,8	116,8	18,1	151,9	19,4	20,7	51,2	59,1	119,5	15,8	150,4	19,1	20,4
PLA-CF	61,9	114,9	16,6	151,8	19,1	24,0	50,6	59,9	121,0	13,3	150,9	17,4	21,8
PLA-WF	61,0	111,7	19,5	153,4	20,4	31,1	49,0	60,0	119,8	18,9	152,5	20,5	31,2

DMA analizė parodė standumo mažėjimą visose medžiagose, tačiau PLA-WF išlaikė didesnį termomechaninį stabilumą ties 80 °C (2,71 MPa), palyginti su grynu PLA (1,6 MPa). Tokie standumo rezultatai siejami su didesniu kristalizavimo laipsniu ir standžiomis užpildo sritimis, ribojančiomis molekulinį judrumą, kai temperatūra pasiekė medžiagos stiklėjimo ribą.

SEM tyrimai parodė, kad grynas PLA turi tankią ir tolygią vidinę struktūrą su lygiu irimo paviršiumi, būdingu matricos dominuojamam, trapiai-plastiškam irimui ir maža energijos absorbcijai. Priešingai, PLA-CF ir PLA-WF kompozituose plaušai pasiskirstę netolygiai, formuojant sankaupų židinius, sukibimo defektus ir mikroporas. Šie defektai sukuria standumo netolygumus ir įtempių koncentracijos vietas, kurie mažina kompozito atsparumą mechaninėms apkrovoms.

Termomechaninis modeliavimas. Sukurtas kombinuotas baigtinių elementų modelis, kuriame termomechaninio uždavinio sprendimas pažingsnių atkuria 3D spausdinimo, aušinimo ir spausdinto objekto atskyrimo nuo gamybos platformos etapus. Vėliau, gauti liekamųjų įtempių ir deformacijų pasiskirstymo laukai eksportuojami į mechaninį modelį. Eksperimentiškai išmatuotas didžiausias spausdinto elemento kraštų vertikalus poslinkis siekė 6,82 mm (S3.2 pav.), o tai gerai sutapo su skaitinio modeliavimo rezultatais. ABAQUS modeliavimo aplinkoje grynojo PLA elemento išlinkis apskaičiuotas su 8,2–10,6 % vidutine paklaida.

DIGIMAT-AM aplinkoje atliktas bandinio išlinkio modeliavimo patikrinimas, lyginant skaitinius rezultatus su eksperimentiškai išmatuotais trijų skirtingų spausdintų medžiagų kraštinių briaunų poslinkiais. Bandymų duomenys parodė, kad trumpų plaušų armavimas sumažino briaunų poslinkį nuo 0,49 mm gryno PLA atveju iki 0,42 mm PLA-CF ir 0,28 mm PLA-WF kompozituose, patvirtindamas teigiamą plaušų poveikį geometrinių matmenų pastovumui. DIGIMAT-AM modeliavimo rezultatai adekvačiai nusako tiek poslinkio mažėjimo tendenciją, tiek jo reikšmę: kiekybiškai vertinant, skaitinis modelis sistemingai nuvertino išmatuotą išlinkį, o santykiniai nuokrypiai PLA, PLA-CF ir PLA-WF atvejais siekė atitinkamai 8,2 %, 14,3 % ir 17,9 % (S3.3 pav.). Šį neatitikimą lemia supaprastintos modeliavimo prielaidos, ypač susijusios su medžiagos modeliavimo būdu.

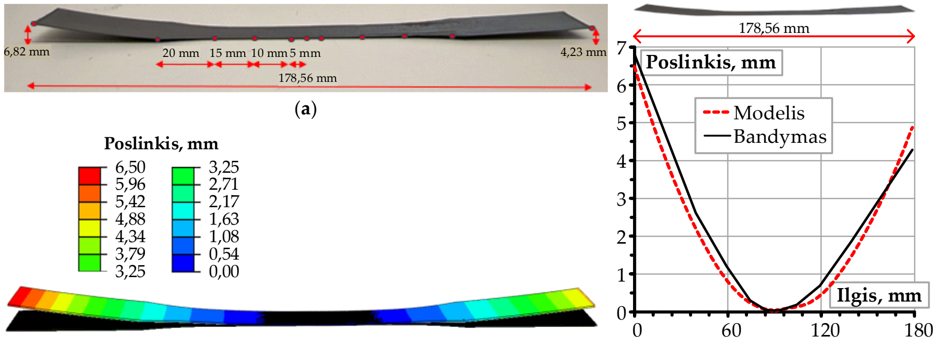

(b) (c)

S3.2 pav. Geometrijos pokyčių analizė: (a) eksperimentiniai matavimo taškai (raudoni apskritimai); (b) baigtinių elementų modeliavimo rezultatai; (c) formos pokyčių profilių palyginimas

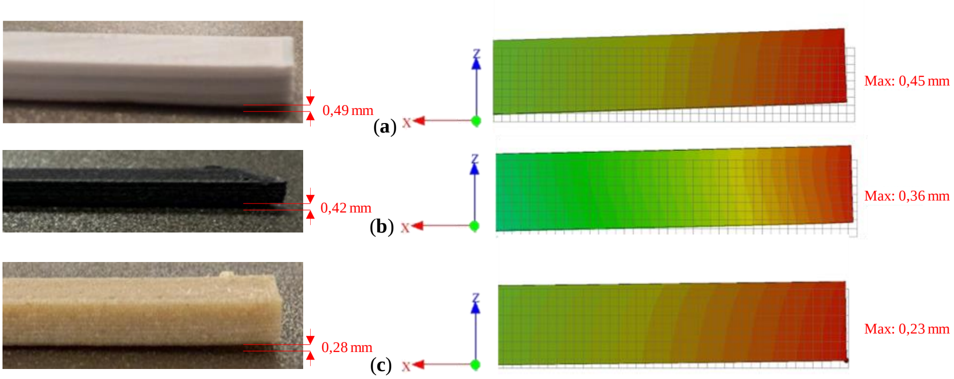

S3.3 pav. Trumpų plaušų armuoto PLA išlinkio eksperimentinių matavimų ir modeliavimo rezultatai DIGIMAT-AM aplinkoje: (a) grynas PLA; (b) PLA CF; (c) PLA WF

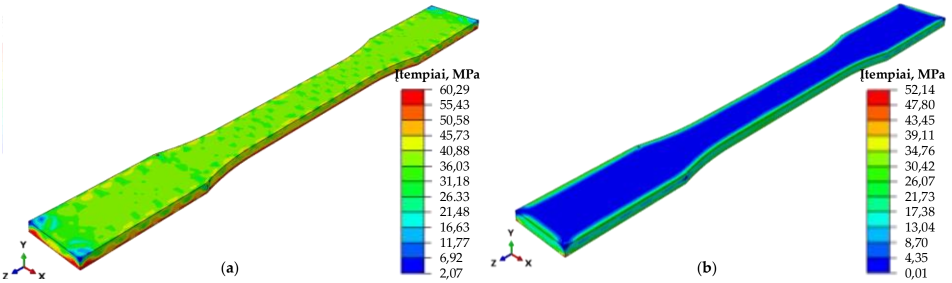

S3.4 pav. Spausdinto bandinio liekamųjų įtempių pasiskirstymo modeliavimo rezultatai: (a) įtempiai ekstruzijos pabaigoje; (b) įtempiai aušinimo pabaigoje

Sukurtas termomechaninis modelis taip pat panaudotas spausdinto bandinio liekamiesiems įtempimams nustatyti. Šiam tikslui temperatūros pokyčių duomenys perkelti į mechaninį modelį kaip pradinė sąlyga, siekiant įvertinti liekamuosius įtempius ir deformacijas, atsirandančias dėl temperatūros kitimo, aušinimo ir formavimo proceso poveikių. Pastebėta, kad, palyginti su kitomis vietomis, didžiausios liekamosios įtempių vertės telkiasi išilgai bandinio briaunų (S3.4 pav.).

Atlikus termomechaninę analizę buvo sudarytas tempimo bandymo modelis. Pirmoji tempimo simuliacija atlikta neįvertinus 3D spausdinimo proceso metu susidarančių liekamųjų įtempių; ši situacija pavaizduota S3.5 pav. kaip 1 BE modelis. 2 BE modelis papildomai įvertino liekamuosius įtempius ir su gamyba susijusius geometrinius netikslumus. Pastarasis modelis parodė, kad liekamieji įtempiai mažina 3D spausdintų komponentų mechanines savybes, o modeliavimo rezultatai patvirtinti fiziniais bandymais (Rimkus et al., 2022). Eksperimentiniu būdu nustatyta 1,7 kN tempimo apkrova esant 2,8 mm poslinkiui; 1 BE modelis prognozavo didesnę laikomąją galią, o 2 BE modelis tiksliau prognozavo laikomosios galios sumažėjimą dėl liekamųjų įtempių ir bandinio geometrijos pokyčių.

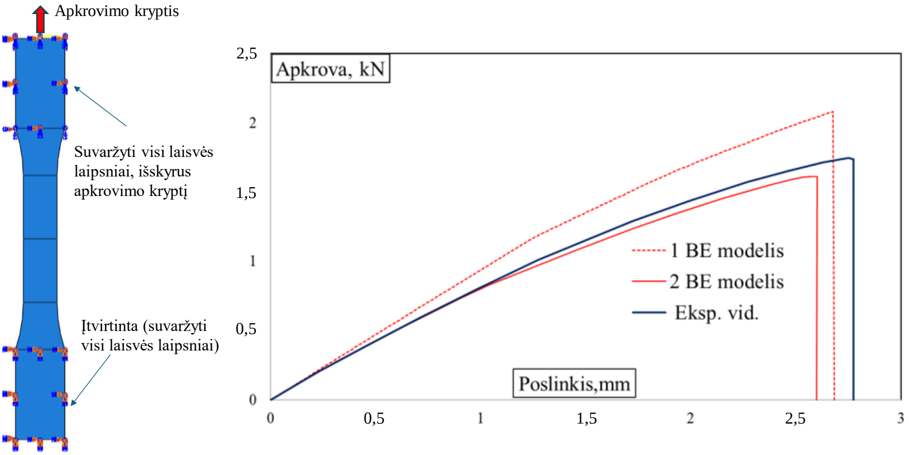

(**a**) (**b**)

S3.5 pav. Tempimo bandymo modeliavimo rezultatai: (a) baigtinių elementų modelis; (b) apkrovos ir poslinkio diagramos

Bendrosios išvados

Disertacijoje nagrinėjama sąsaja tarp pluoštu armuotų PLA kompozitų 3D spausdinimo proceso parametru, kompozitų sudėties ir mechaninių savybių. Rezultatai rodo, kad armavimo efektyvumas priklauso nuo armavimo sąlygų: ištisinė aramido gija padidina kompozito atsparumą tempimui, tačiau jos efektyvumą riboja armavimo gijos išdėstymo ir tempimo apribojimai spausdinimo metu, o trumpi plaušai pagerina medžiagos tąsumą ir standumą bei mažina geometrines formos nuokrypius. Mechaninis stipris priklauso nuo armavimo sukibimo defektų ir vidinių defektų atsiradimo spausdinimo metu. Sukurtas kombinuotas modeliavimo metodas leidžia vertinti geometrinius pokyčius ir liekamąsias deformacijas bei įtempius, todėl padeda parinkti medžiagas ir spausdinimo parametrus, užtikrinančius gaminio geometrinį tikslumą. Gauti rezultatai yra aktualūs lengvųjų konstrukcinių elementų projektavimui, pvz., dronų komponentams, robotų ir mažų transporto priemonių dalims, kur mažas svoris ir mechaninis atsparumas yra esminiai projektavimo kriterijai. Pagrindinės darbo išvados:

1. Ištisinės gijos armavimas turi ribotumų dėl suderinamumo, sutankinimo, gijos išdėstymo ir įtempimo stokos spausdinimo metu. Armuojančios aramido gijos įvedimas į 3D spausdinimui PLA tinkamą vyksta dviem etapais: ištisinės aramido gijos įterpimu į PLA giją ir bandinio formavimu spausdinant, todėl abiejų etapų defektai sumuojasi. Praktiškai naudingas rezultatas pasiektas parodant, kad ištisai armuota gija gali būti spausdinama įprasto vieno ekstruderio 3D spausdinimo įranga, bei armavimo efektyvumas nėra aukštas. Vertinant pagal teorinio modelio rezultatus, pasiekta tik 6,8 % standumo ir 13,6 % laikomosios galios reikšmės.
2. Mechaniniai bandymai ir SEM, DSC bei DMA analizės rezultatai parodė trumpo plaušo tipo poveikio skirtumus: medienos plaušai (30 % tūrio kiekis) padidina kristalizavimo lygį, tąsumą ir 43 % sumažina liekamąsias deformacijas, o anglies plaušai (10 % tūrio kiekis) padidina spausdinto gaminio standumą ir 14 % sumažina liekamąsias deformacijas. Praktiškai šie rezultatai leidžia rekomenduoti medienos plaušus tais atvejais, kai svarbus gaminių matmenų tikslumas, o anglies plaušus – kai prioritetas yra didesnis medžiagos standumas.
3. Sukurtas kombinuotas termomechaninis 3D spausdinimo modelis leidžia automatiškai transformuoti spausdinimo kodą (G-kodą) į baigtinių elementų aktyvavimo instrukciją ir eksportuoti liekamųjų deformacijų bei įtempių laukus į mechaninio modeliavimo etapą. Apskaičiuotos liekamosios deformacijos atitinka eksperimentinius rezultatus, esant 10,6 % vidutinei paklaidai. DIGIMAT aplinkoje išplėstas modeliavimo metodas trumpais plaušais armuotiems kompozitams leido nustatyti jų liekamąsias deformacijas. Toks modelis sukurtas pirmą kartą. Praktikoje šis metodas sumažins bandymų ir klaidų kiekį, leis parinkti medžiagas ir spausdinimo nustatymus, atsižvelgiant į priimtinus geometrinių matmenų nuokrypius.

Mahmoud Samy Mahmoud Mohammed FARH

ANALYSIS AND MODELING OF DEFORMATIONS
INDUCED BY THE EXTRUSION OF FIBER-REINFORCED POLYMERS
Doctoral Dissertation

Technological Sciences,
Materials Engineering (T 008)

PLUOŠTAIS ARMUOTŲ POLIMERŲ EKSTRUZIJOS
SUKELTŲ DEFORMACIJŲ ANALIZĖ IR MODELIAVIMAS

Daktaro disertacija

Technologijos mokslai,
Medžiagų inžinerija (T 008)

Lietuvių kalbos redaktorė Deimantė Grigaitė
Anglų kalbos redaktorė Jūratė Griškėnaitė

2026 05 08. 13,8 sp. l. Tiražas 20 egz.
Leidinio el. versija *https://doi.org/10.20334/2026-023-M*
Vilniaus Gedimino technikos universitetas
Saulėtekio al. 11, 10223 Vilnius
Spausdino UAB „Ciklonas“,
Žirmūnų g. 68, 09124 Vilnius